

BYG•DTU

DANMARKS  
TEKNISKE  
UNIVERSITET



Martin Uhre Pedersen

# Dowel Type Timber Connections

Strength modelling

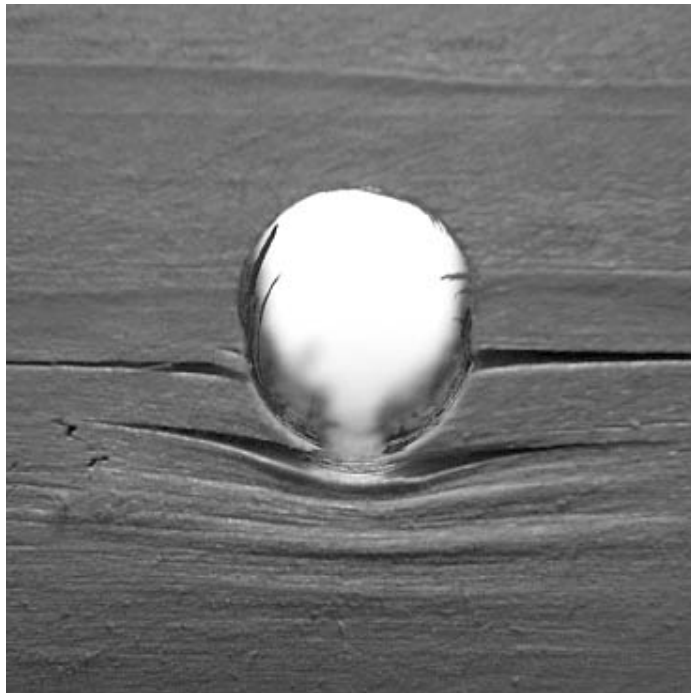
Rapport  
BYG•DTU R-039  
2002  
ISBN 87-7877-097-1



# Dowel Type Timber Connections

Strength modelling

Martin Uhre Pedersen



**Department of Civil Engineering**  
**DTU-building 118**  
**2800 Kgs. Lyngby**  
<http://www.byg.dtu.dk>

2002



# Preface

This thesis is submitted as a partial fulfilment of the requirements for the Danish Ph.d. degree.

The work has been carried out at the Department of Structural Engineering and Materials (BKM), Technical University of Denmark (DTU), during the years 1996 to 2000. Associate Professor, Ph.D. Lars Damkilde and Associate Professor, Ph.D. Preben Hoffmeyer have supervised the study.

I wish to express my gratitude to my supervisors for their inspiration to and active participation in the project while giving me full freedom in my work and at the same time helping me prepare and in various fora present the results obtained. I am also grateful to them for enabling me to interrupt the project on several occasions to solve design assignments for the Danish glulam industry. Though this work for Limtræ Danmark A/S has prolonged the project it has also made my time at the Department very dynamic.

In the same vein I would like to thank the staff at the Department, especially my colleague Christian Clorius, for their help. Further, the following are acknowledged for their support to the work: Limtræ Danmark, Fiberline Composites, and BMF bygningsbeslag.



# Abstract

Large primary connections in wood structures such as apex or foot point connections in e.g. 3-charnier arches or the connections in large glulam truss girders are often designed by use of dowel type connections. The design loads are in these cases primarily in the axial direction of the wood member. With respect to the axial loads the connections may be both strong and ductile, inevitable however the connections will also be subjected to loads acting transverse to the fibre direction of the wood. This may be a direct function of the external loading, e.g. transference of shear forces, or it may be the indirect consequence of a connection modelled as an ideal hinge which in reality transfers moment according to its relatively uncontrolled bending rigidity.

Dowel type timber connections have been studied with the main focus on loading where the dowels act on the embedment with an angle to the grain. Splitting failures are known to occur even for dowel type connections loaded in the grain direction. However, in this work splitting is studied in direct transverse loading. The objective is to study the range of validity of yield modelling of dowels and dowel groups when transversely loading of the dowels is present. This is done by means of a yield surface determined for the single connectors, implemented in a modelling of joints containing a group of dowels exposed to loads in both the axial and transverse direction of the wood member.

A study of the embedment strength as function of angle to grain shows that by the current design rules the embedment strength perpendicular to grain is overestimated by approximately 50 %.

Further, a study of the use of fibre reinforced plastic, FRP, as replacement for steel in dowels as well as insertion plates is presented. The study shows that connections made by use of FRP dowels exhibit plastic behaviour at a load which is independent of the wood member thickness. A strength criterion for FRP dowels combining the effect of shear and moment is implemented in the yield model for connectors. By use of this combined criterion the ultimate strength can be modelled and with small modifications the onset of plastic behaviour can be predicted.



# Resumé

Store primære samlinger i trækonstruktioner såsom kip- og fodsamlinger i 3-charniers buer eller samlingerne i store limtrægitterspær designes ofte ved brug af dorntypeforbindelser. Designlasterne er i disse tilfælde primært i træelementets aksielle retning. For aksielle laster er forbindelserne både stærke og duktile, men samlingerne bliver uundgåeligt også påvirket af kræfter, der virker på tværs af træets fiberretning. Dette kan være en direkte funktion af ydre last, f.eks. overførsel af forskydningskræfter, eller det kan være en indirekte funktion af, at samlingen optager et moment i overensstemmelse med dens relativt ukontrollerede bøjningsstivhed, selvom den er modelleret som et ideelt charnier.

Dorntypeforbindelser er blevet studeret med fokus på lasttilfælde, hvor dornen virker mod træet under en vinkel med fiberretningen. Flækningsbrud kendes selv fra dorntypeforbindelser belastet udelukkende i fiberretningen. I dette arbejde studeres flækningsbrud imidlertid ved direkte belastning på tværs af fiberretningen. Målet er at studere gyldigheden af en plastisk modellering af dorne og dorngrupper, når dornene påvirker træet direkte på tværs af fiberretningen. Dette er blevet gjort ved hjælp af en flydeflade bestemt for det enkelte forbindelsesmiddel og herefter implementeret i modelleringen af en samling, der indeholder en gruppe dorne, der udsættes for laster såvel i træets aksielle retning som på tværs heraf.

En undersøgelse af hulrandsstyrken som funktion af vinklen med fiberretningen viser, at i følge de gældende designregler overestimeres hulrandsstyrken vinkelret på fiberretningen med omkring 50 %.

Yderligere præsenteres en undersøgelse af brugen af fiberforstærket plast, FRP, som erstatning for stål i dorne såvel som i indslidsede plader. Undersøgelsen viser, at forbindelser med FRP-dorne udviser plastisk opførsel ved en last, som er uafhængig af sidetræstykkelsen. Et brudkriterium for FRP-dorne, der kombinerer effekten af forskydning og moment er implementeret i flydemodellen for forbindelsesmidlerne. Ved hjælp af dette kombinerede kriterium kan den ultimative styrke modelleres og med små modifikationer kan initieringen af plastisk opførsel forudsiges.



# Table of Contents

<b>Table of Contents</b>	<b>i</b>
<b>1 Introduction</b>	<b>1</b>
<b>2 Background on dowel type connections</b>	<b>3</b>
2.1 Plastic failure criterion . . . . .	4
2.1.1 Slotted-in steel plates . . . . .	4
Double shear connections . . . . .	4
Experimental realisation of double shear failure . . . . .	6
Model refinements . . . . .	7
Multiple shear connections . . . . .	8
2.2 Global design criteria . . . . .	10
Stress Condition in Dowel Proximity . . . . .	10
2.2.1 Distance and spacing criteria . . . . .	12
2.2.2 Reduction for multiple dowels . . . . .	13
2.2.3 Increasing slenderness ratio . . . . .	15
2.2.4 Wood reinforcement . . . . .	16
2.2.5 Production precision . . . . .	17
<b>3 Embedment and dowel capacity</b>	<b>19</b>
3.1 Embedment . . . . .	19
3.1.1 Embedment strength . . . . .	19
Old Danish code . . . . .	20
New Danish code . . . . .	20
Eurocode . . . . .	20
3.2 Embedment tests . . . . .	21
3.2.1 Material and method . . . . .	21

	Randomized complete block test . . . . .	21
	Additional tests . . . . .	22
3.2.2	Results . . . . .	22
	Randomized complete block test . . . . .	22
3.3	Embedment modelling . . . . .	29
3.3.1	Strength and code rules . . . . .	29
	Fibre direction . . . . .	29
	Perpendicular to fibre direction . . . . .	29
3.3.2	Yield surface . . . . .	30
3.4	Dowels . . . . .	31
3.4.1	Dowel bending tests . . . . .	31
3.4.2	Determination of bending capacity . . . . .	32
<b>4</b>	<b>Tension splitting due to transverse load</b>	<b>35</b>
4.1	Material and methods . . . . .	35
4.1.1	Bending tests . . . . .	36
4.1.2	Embedment and compression tests . . . . .	37
4.1.3	Transverse tension tests . . . . .	37
4.2	Results . . . . .	38
4.2.1	Bending tests . . . . .	38
	Spacing variation . . . . .	40
4.2.2	Embedment and compression tests . . . . .	41
	Oriented compressive tests . . . . .	43
4.2.3	Transverse tension tests . . . . .	43
4.3	Predicting failure . . . . .	44
4.4	Wood structure in RT-plane . . . . .	45
<b>5</b>	<b>Full scale connections</b>	<b>49</b>
5.1	Material and Method . . . . .	49
5.1.1	Specimens . . . . .	49
5.1.2	Test conditions . . . . .	51
5.2	Results . . . . .	52
<b>6</b>	<b>Discussion on full scale connections</b>	<b>59</b>
6.1	Modelling full scale connections . . . . .	59
6.1.1	Single connector description . . . . .	59

	Model parameters for $t=40$ mm . . . . .	62
	Model parameters for $t=65$ mm . . . . .	62
6.1.2	Yield modelling of full connection . . . . .	62
6.2	Brittle modelling of full scale connections . . . . .	64
6.2.1	Shear based failure modelling . . . . .	64
6.2.2	Slenderness ratio . . . . .	66
<b>7</b>	<b>Fibre reinforced plastic in dowel type connections</b>	<b>69</b>
7.1	Background . . . . .	69
7.2	Material and tests . . . . .	70
7.3	Dowel properties . . . . .	71
7.4	FRP-embedment . . . . .	72
7.5	Connector tests . . . . .	72
7.6	Buckling properties . . . . .	77
7.6.1	Plate bending tests . . . . .	77
7.6.2	Buckling tests . . . . .	79
<b>8</b>	<b>Modelling FRP in dowel type connections</b>	<b>81</b>
8.1	FRP connector modelling . . . . .	81
8.1.1	Traditional model including shear in dowel . . . . .	81
8.1.2	English model . . . . .	82
8.1.3	Inherited model from wood dowels . . . . .	82
8.1.4	Elasto-plastic model . . . . .	83
8.2	Model implementation . . . . .	83
8.2.1	Traditional model including shear in dowel . . . . .	83
	Dowel strength . . . . .	83
	Connector strength . . . . .	85
8.2.2	English model . . . . .	86
8.2.3	Inherited models . . . . .	87
8.2.4	Elasto-plastic model . . . . .	87
	Dowel stiffness . . . . .	87
	Elasto-plastic model input . . . . .	89
	Elasto-plastic model results . . . . .	89
8.3	Model comparison . . . . .	89
8.3.1	Failure definition . . . . .	89

8.3.2	Comparison between models . . . . .	91
8.3.3	Comparison with steel . . . . .	93
8.4	FRP plates . . . . .	94
8.4.1	Embedment strength of FRP plates . . . . .	94
8.4.2	Buckling of FRP plates . . . . .	95
<b>9</b>	<b>Conclusion</b>	<b>97</b>
	<b>Bibliography</b>	<b>103</b>
	<b>List of Symbols</b>	<b>107</b>
	<b>List of Abbreviations</b>	<b>109</b>

Paper I: Strength of Glued-In Bolts after Full-Scale Loading. Pedersen, M. U., Clorius, C. O., Damkilde, L. & Hoffmeyer, P., *Journal of Performance of Constructed Facilities*, 13 (3)(1999), 107–113.

Paper II: A simple size effect model for tension perpendicular to the grain. Pedersen, M. U., Clorius, C. O., Damkilde, L. & Hoffmeyer, P., accepted for publication in: *Wood Science and Technology*

Paper III: Compressive fatigue in wood. Clorius, C. O., Pedersen, M. U., Hoffmeyer, P. & Damkilde, L., *Wood Science and Technology*, 34 (2000), 21–37.

## Chapter 1

# Introduction

Udviklingen har vist, at Trækonstruktionerne, som allerede for Aarhundereder siden kunde fremvise imponerende Resultater, igen i vor Tid har faaet et løfterigt ”come back”.

København Januar 1947

Anker Englund

This quote from the wood construction textbook written by the former principal of the Technical University of Denmark appraises that: *The development has shown that wood constructions, which already centuries ago demonstrated impressive results, again in our time have achieved a promising come back.*

The fifty year old quote exemplifies the almost overwhelming joy and enthusiasm with which each generation seems able to celebrate the promising future for wood and timber constructions. The sentimentality apart, wood is a cheap and in many situations very apt construction material. However, it has its shortcomings among which proper design of connections most prominently challenges the structural engineer.

In the undergraduate course on timber construction, theoretical fulfilling load bearing formulas for single dowel type connectors are taught one day just to be blurred the next day by highly empirical and mostly unexplained requirements to spacing and distances.

So, on one hand, at the local level of the single connector, a highly rationalized failure theory exists embedded in the theory of plasticity. On the other hand, at the more global level of the whole cross sections inflicted by a connection, the engineer is left with empirical spacing criteria and a restriction on the shear capacity. These spacing criteria are to assure sufficient non plastic capacity of the cross section to ensure that plastic failure is not supervened by a brittle global failure.

In the literature much attention is given to the problem of failure in tension perpendicular to the grain for loading of dowel type connections in the grain direction. In this thesis the emphasis is laid on splitting failure when the loading is transverse to grain. That is, a realistic yield surface for the single connector is established as function of the load direction to grain and experiments and modelling are conducted on groups of connectors subject to combinations of axial and transverse load in order to verify if the group of connectors can be plastically modelled or if tension perpendicular to the grain failures precedes plastic failure.

It is the position of the author that with the plasticity theory a consistent and intelligible design criterion is given. Though some failures in dowel type connections are only modelled by brittle failure mechanisms, from simple shear strength criteria to more refined fracture mechanics, the complexity hereby added to the design process may be overruled just by adding more material, enhancing the brittle strength of the cross section.

The thesis falls in four main parts: An investigation of embedment and dowel properties, demonstration and discussion of non-ductile failures due to transverse loads, testing and modelling of full scale connection capacity as function of load direction, and a mapping of the behaviour of connections where the steel parts are replaced with glass fibre reinforced plastic.

## Chapter 2

# Background on dowel type connections

Dowel type connections is a generic term covering nails, screws, dowels and bolts transferring load perpendicular to their longitudinal axis. In principle the load bearing mechanisms are the same for long slender nails as it is for stout bolts though the different mechanical fasteners pronounce different types of design aspects.

The design of dowel type connections consists of two relatively independent types of design criteria, a local set and a global set:

- The local design criteria consists of plasticity theory applied to the single connector, i.e. the capacity of the connector and of the wood in which it is embedded is evaluated.
- The global design criteria consists of criteria for spacing and distance between the single connectors which are to insure global capacity of the cross section enough to withstand the forces transferred by the connectors.

The local design criteria corresponds to the so called European Yield Model formulated by K. W. Johansen. He first applied theory of plasticity to dowel type connectors in wood in (Johansen 1941) and (Johansen 1949). This design criteria for the single connector now form the basis for the design rules given in the Eurocode (EC5-1 1995). There has not been much dispute about the design criteria at the local level. At the global level, however, the dispute is never ending as it is possible to obtain global splitting of the cross section before the local yield strength is obtained.

## 2.1 Plastic failure criterion

Calculation of the load bearing capacity of the single connector is compact and simple. Ideal plasticity of both steel and wood is assumed and further the dowel is assumed rigid-plastic. The ultimate load bearing capacity of a single connector is predicted to be when either the stresses in the wood reaches the plastic failure stress level or when a combination of plastic failure in wood and dowel is attained.

In order to determine the load bearing capacity for a specific connector geometry, the kinematic possible failure modes are determined. The load corresponding to failure at each failure mode is determined directly from stress equilibrium conditions. For a given geometry the actual failure mode will be that among the kinematic possible which gives the lowest failure load.

### 2.1.1 Slotted-in steel plates

Steel fishplates connecting wood members have the benefit of increasing the load bearing capacity of the connection as the bending moment in the connectors generally decreases for the same external load because the steel plate gives a smaller eccentricity compared to a wood member with the same capacity. This is fully recognized in the Eurocode whereas the danish code do not allow full benefit of the steel member in all cases. In the following the load bearing formulas are derived and discussed.

### Double shear connections

The kinematically possible failure modes are shown in Figure 2.1 for a double shear connection with a central steel plate. The three possible failure modes are shown and below the forces acting on the dowel as well as the occurring plastic hinges in the dowel are schematized.

**Mode I:** In mode I the dowel is dragged through the wood that yields plastically. The capacity per shear plane,  $F_y$ , is given by a simple projection:

$$F_y = t d f_h, \quad (2.1)$$

where  $f_h$  is the embedment strength,  $t$  the wood thickness per side and  $d$  is the dowel diameter.

**Mode II:** Mode II failure is realized when the embedment stresses act on the dowel over a sufficient length to form a plastic hinge in the dowel. The hinge is formed at the location of the steel plate and the dowel rotates as a stiff member in the wood. All

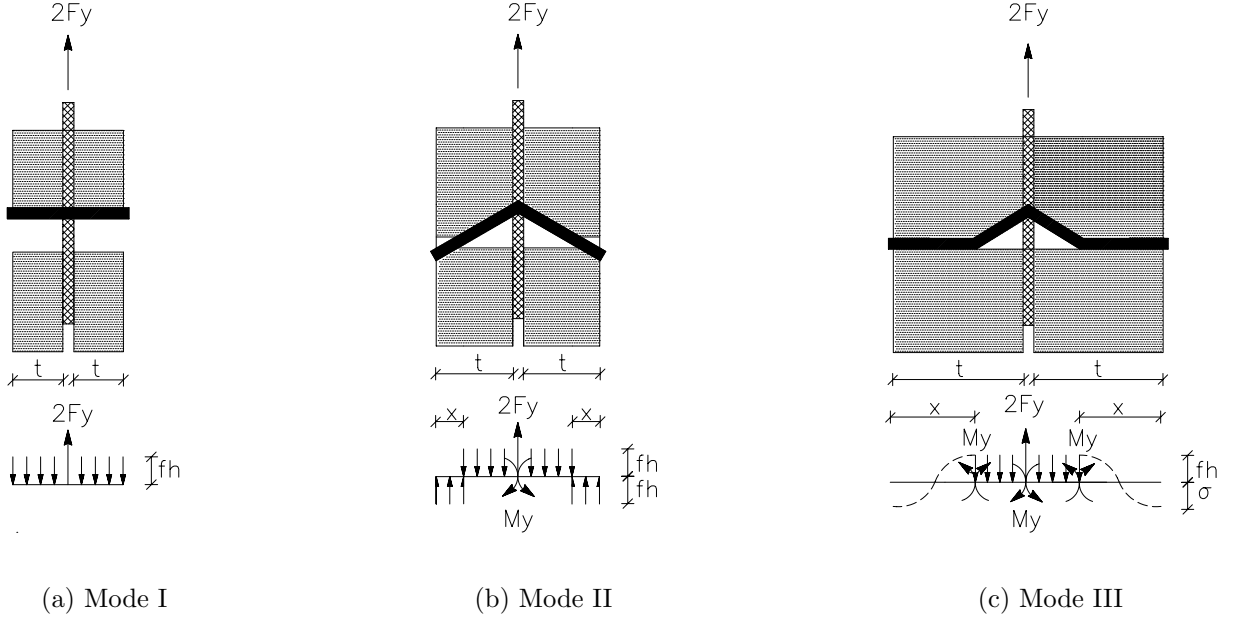


**Figure 2.1:** *The three possible plastic failure modes for a double shear dowel connector used with a central steel plate.*

embedment stresses are directed opposite the force in the steel plate if  $t$  is just wide enough to form a plastic hinge in the dowel. For larger values of  $t$  the embedment stresses are directed both ways. The capacity is determined by use of a projection and a moment equation. Eliminating the unknown  $x$ , the capacity per shear plane is:

$$F_y = \left( \sqrt{2 + 4 \frac{M_y}{t^2 d f_h}} - 1 \right) t d f_h, \quad (2.2)$$

where  $M_y$  is the plastic yield moment of the dowel, for a circular dowel it is determined as:  $M_y = W_y f_{y, \text{steel}} = \frac{1}{6} d^3 f_{y, \text{steel}}$ .

**Mode III:** Mode III failure is realized when the stress on the dowel acts over sufficient length  $x$  to form an additional plastic hinge in the dowel. The capacity is determined by use of projection and moment equation, using that the shear is zero in the plastic hinges. The capacity per shear plane is:

$$F_y = \sqrt{4 M_y d f_h}. \quad (2.3)$$

In summary, the capacity of a dowel is a function of embedding strength,  $f_h$ , dowel diameter,  $d$ , and the plastic moment capacity,  $M_y$ , of the dowel. The failure mode will

progress from I to III as the thickness,  $t$ , of the wood member increases, and the capacity per shear plane is determined by:

$$F_y = \begin{cases} t d f_h & \text{for } t < \sqrt{\frac{2M_y}{d f_h}} & \text{Mode I} \\ \left( \sqrt{2 + 4 \frac{M_y}{t^2 d f_h}} - 1 \right) t d f_h & \text{for } \sqrt{\frac{2M_y}{d f_h}} \leq t < \sqrt{\frac{16M_y}{d f_h}} & \text{Mode II} \\ \sqrt{4M_y d f_h} & \text{for } t \geq \sqrt{\frac{16M_y}{d f_h}} & \text{Mode III} \end{cases} \quad (2.4)$$

The formulas in equation (2.4) are similar to those given in Eurocode 5 (EC5-1 1995, eq. 6.2.2e–f), with the only exception that for mode II and III EC5 allows for additional 10% load bearing capacity. The origin of these extra 10% is unclear but may be referred to friction capacity.

### Experimental realisation of double shear failure

The failure modes in (2.4) are easily realized experimentally. Figure 2.2 shows the three modes realized for a thin, 6 mm dowel going through a 6 mm hole in a 6 mm steel plate. Mode I in Figure 2.2(a) is realized for  $t = 12$  mm, mode II for  $t = 22$  mm and  $t = 47$  mm seen in Figure 2.2(b) and (c); the latter is on transition into mode III shown in (d) for  $t = 57$  mm. The adequacy of the strength modelling is verified in Table 2.1 which gives the yield strength,  $F_y$ , determined according to (2.4) and the corresponding failure mode. The theoretical strength lies within 5% of the mean value for each geometry. The embedding strength,  $f_{h,0}$ , used as input in (2.4), is determined directly of the results for  $t = 12$  mm, and is found to be 37.3 MPa. The plastic capacity of the dowel,  $M_y$ , is determined in 3 point bending. The steel exhibits large strain hardening and a capacity of 30 Nm ( $f_y = 830$  MPa) is obtained. This yield capacity corresponds to relatively large deformations, the ultimate strength of the connections is however also determined at relatively large deformations, see Figure 2.2.

	$t=12$ mm	$t=22$ mm	$t=34.5$ mm	$t=47$ mm	$t=57$ mm
Experimental strength	2.68	3.94	4.48	5.06	5.13
Failure mode	I	II	II	II/III	III
Theoretical strength	2.68	3.76	4.37	5.18	5.18
Failure mode	I	II	II	III	III

**Table 2.1:** Strength,  $F_y$ , per shear plane [kN].

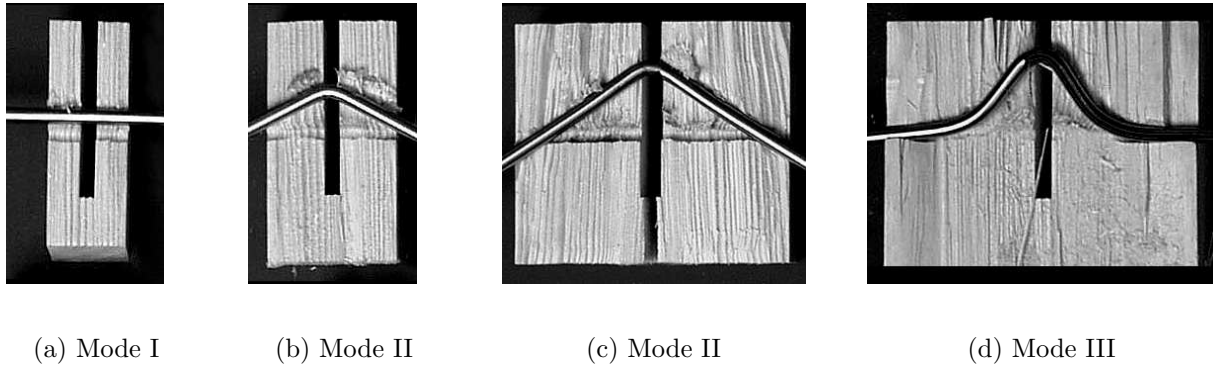


**Figure 2.2:** *Experimental realizations of failure modes for loading in the grain direction, (Eskildsen:1999).*

### Model refinements

The Eurocode uses the theoretical formulas for slotted in steel plates, i.e. the formulas are equal to (2.4). These formulas are derived under the assumption that the steel plate has no extension. In a controlled laboratory test, e.g. as shown in Figure 2.2, the no-extension condition can be obtained by tight fitting connection between steel plate and dowel. At both sides of the steel plate a plastic hinge is formed in the dowel and hence the load is transferred as if the steel plate had no extension.

In real constructions the no-extension condition of the steel plate is often not realised. The slot for the steel plate is often oversized (approximately 2 mm) and the holes in the steel plate for the dowels are not tight fitting either. Under these conditions the Eurocode load bearing formulas may be optimistic. In the following paragraphs the theoretical load bearing formulas for a double shear connection with a central steel plate are derived under the condition that the load on the dowel from the wood side members acts on the dowel with an additional eccentricity,  $e$ , relative to the central hinge.

Further load bearing formulas are derived under the condition that the holes in the wood side members are not tight fitting. Oversized holes are generally not allowed for dowels in real structures, but they occur, and the load bearing formula under this condition corresponds to the conditions of some of the tests reported in Chapter 5.

***Slotted in steel plate with slot eccentricity***

In (2.5) the load bearing capacity is given under the assumption that the slot has a width of  $2e$ . Hence, the dowels suffer from additional bending due to the eccentricity  $e$ :

$$F_y = \min \begin{cases} t d f_h & \text{Mode I} \\ \left( \sqrt{2 + 4\frac{e^2}{t^2} + 4\frac{e}{t} + 4\frac{M_y}{t^2 d f_h}} - (1 + 2\frac{e}{t}) \right) t d f_h & \text{Mode II} \\ \left( \sqrt{e^2 + 4\frac{M_y}{d f_h}} - e \right) d f_h & \text{Mode III} \end{cases} \quad (2.5)$$

***Eccentricity and oversized holes***

The consequence of oversized holes is that the restriction on the rotation of the outer part of the dowel is diminished. For sufficiently oversized holes mode III is never realized and mode II cannot take higher values than corresponding to the transition between mode I and II. In (2.6) the load bearing capacity is given for a double shear connection with a central steel plate including slot eccentricity and the effect of oversized holes:

$$F_y = \min \begin{cases} t d f_h & \text{Mode I} \\ \left( \sqrt{e^2 + 2\frac{M_y}{d f_h}} - e \right) d f_h & \text{Mode II} \end{cases} \quad (2.6)$$

**Multiple shear connections**

Multiple shear connections using slotted in steel plates have according to Gehri in (Madsen 2000) been known since the 1940'ties and are widely used in modern timber constructions. In the Eurocode the load bearing formulas are not explicitly given for more than two shear planes. For higher number of shear planes it is recommended to calculate the capacity as the lowest load carrying capacities for each shear plane, taking each shear plane as part of a series of double shear connections. This procedure is of course conservative for all failure modes that benefits from the rotational restriction of the dowel in the section between the fictitious double shear connections. Load bearing formulas can be derived from the kinematically possible failure modes as shown in Figure 2.3 for a connection with slotted in steel plates and four shear planes. The corresponding formulas for load bearing

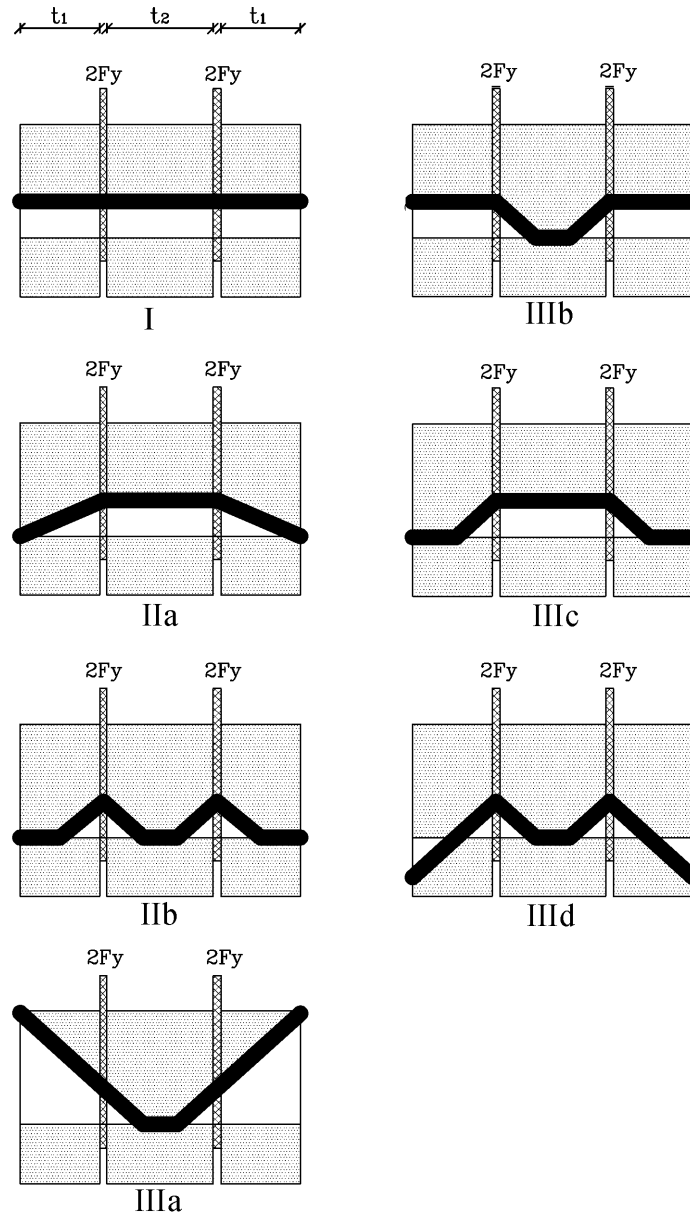


**Figure 2.3:** *Kinematically possible failure mode in a connection with slotted in steel plates and four shear planes.*

capacity are:

$$F_y = \min \left\{ \begin{array}{ll} \frac{1}{4}(2t_1 + t_2)d f_h & \text{Mode I} \\ \left( -\frac{1}{2}t_1 + \frac{t_2}{4} + \sqrt{\frac{1}{2}t_1^2 + \frac{M_y}{d f_h}} \right) d f_h & \text{Mode IIa} \\ \sqrt{4M_y d f_h} & \text{Mode IIb} \\ \left( \frac{1}{2}t_1 + \frac{1}{2}\sqrt{t_1^2 + \frac{2M_y}{d f_h}} \right) d f_h & \text{Mode IIIa} \\ \left( \sqrt{\frac{M_y}{d f_h}} + \frac{1}{2}t_1 \right) d f_h & \text{Mode IIIb} \\ \left( \sqrt{\frac{M_y}{d f_h}} + \frac{1}{4}t_2 \right) d f_h & \text{Mode IIIc} \\ \left( -\frac{1}{2}t_1 + \sqrt{\frac{1}{2}t_1^2 + \frac{M_y}{d f_h}} + \sqrt{\frac{M_y}{d f_h}} \right) d f_h & \text{Mode IIId} \end{array} \right. \quad (2.7)$$

The extra load bearing capacity gained when using (2.7) compared to the procedure suggested in the Eurocode can only be evaluated given the material parameters. Then it is possible to optimize the geometry benefitting from the rotational restriction in the central section.

## 2.2 Global design criteria

### Stress Condition in Dowel Proximity

The non-plastic failures all arise due to stresses best visualized in a transverse section of the dowel in wood. Figure 2.4 shows such a transverse section where the stress condition in the wood in dowel proximity is schematized with special attention to tension and embedment stresses. The embedment stresses shown in the figure are of course the consequence of the dowel acting on the wood. The tension stress singularity is the consequence of the tension state in the wood moving towards the dowel wherein it is concentrated and passed on. The eccentricity tension stresses are the consequence of the eccentricity of the distant uniform stress state in the wood member relative to the concentrated force in the dowel. Hence, these stresses take the highest value for a single connector in a wide wood member; the more connectors – the more smeared are the dowel reactions over the cross section and the smaller become the eccentricity tension stresses. The tension singularity stresses have no such variation with the number of connectors.

The occurrence of non-plastic failures is of course the consequence of some wood capacity being fully utilised before the embedment stresses reaches the embedment strength. In order to understand why tension splitting often occurs when the loading is in the trans-

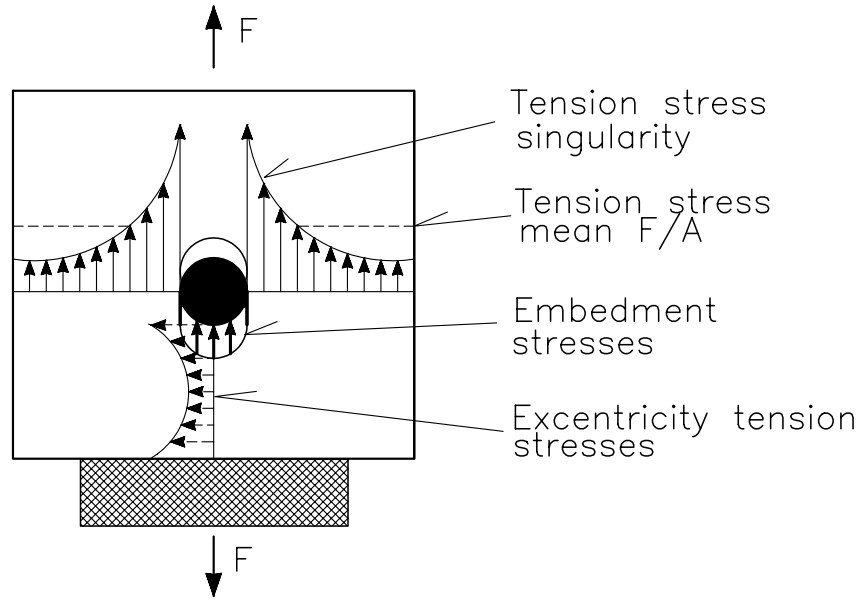


**Figure 2.4:** *Schematic stress condition in a transverse section in dowel proximity, with attention to tension stresses.*

verse direction it might be helpful to look at the ratio,  $\eta$ , between the embedded strength and the strength of the material where the stress singularity occurs. When loading in the grain direction the tension singularity stresses shown in Figure 2.4 are carried by strong continuous fibres laying as tangents to the dowel hole. This of course gives the possibility of a high degree of utilization of the embedded strength,  $f_{h,0}$ , as:

$$\eta_0 = \frac{f_{h,0}}{f_{t,0}} \approx \frac{0.67 f_{c,0}}{f_{t,0}} = \frac{0.67 \cdot 45 \text{ MPa}}{90 \text{ MPa}} = 0.34, \quad (2.8)$$

where typical values for tension and compression strength parallel to the grain,  $f_{t,0}$  and  $f_{c,0}$ , are taken from (Larsen & Riberholt 1988);  $f_{h,0} = 0.67 f_{c,0}$  is an empirically based rule used in the Danish code (Larsen & Riberholt 1991).

When the loading is in the transverse direction the singularity stresses are carried in tension perpendicular to the grain – a brittle strength parameter of low value – which of course limits the possible degree of utilization of the embedded strength,  $f_{h,90}$ , as:

$$\eta_{90} = \frac{f_{h,90}}{f_{t,90}} \approx \frac{17.4 \text{ MPa}}{2.2 \text{ MPa}} = 7.9, \quad (2.9)$$

where the value for  $f_{h,90}$  and  $f_{t,90}$  corresponds to the values given in Chapter 4.

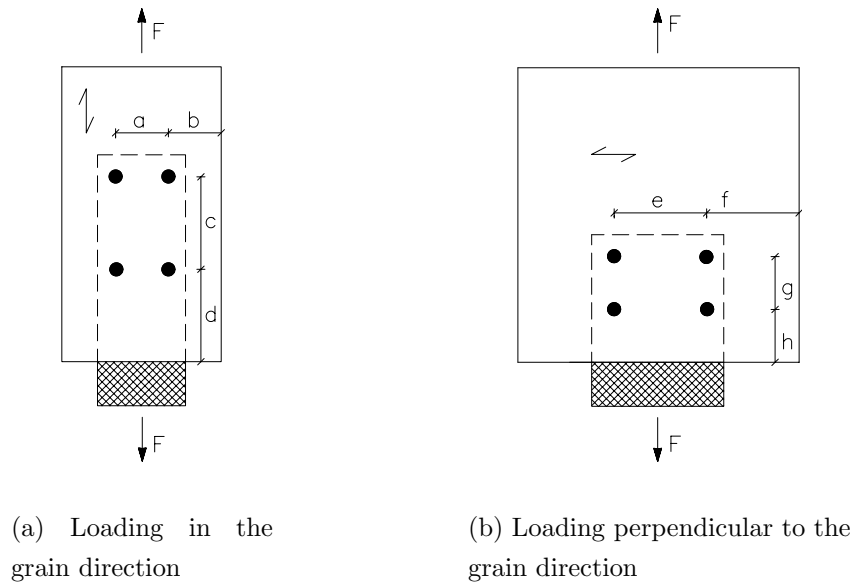


**Figure 2.5:** *Dowel spacing for parallel and transverse loading.*

### 2.2.1 Distance and spacing criteria

The global design criteria to a cross section with dowels and slotted in plates take the form of minimum end and side distance and spacing requirements. The spacing requirements are discussed in e.g. (Nielsen & Johansen 1970) where it is noted that K. W. Johansen's theory was originally tested in experiments containing abundantly wood.

The requirements are meant to ensure both that the capacity of the whole cross section is sufficient and that the connectors do not interact and provoke brittle splitting or tear out failures. When the load is applied in the grain direction, as shown in Figure 2.5 (a), the non-plastic failures to be avoided are primarily shear plug failure and tension splitting. In shear plug failure the material beneath a dowel is dragged out in shear failure. Tension splitting may arise for two reasons; it may be a secondary phenomenon supervening embedment failure, i.e. due to embedment failure the dowel or the crushed wood can be dragged down between the fibres and hereby cause splitting. However, tension splitting may also occur in a more pure form due to the eccentricity tension stresses perpendicular to the grain. For these reasons probably, the empirical side and end distance and spacing requirements are more restrictive in the grain direction than in the transverse direction when the dowel acts as shown in Figure 2.5 (a). Different non-plastic failures are reported

in e.g. (Mohammad, Quenneville & Smith 1997).

When the load is in the transverse direction as shown in Figure 2.5 (b), the non-plastic failure to be avoided is primarily tension splitting caused by the tension stress concentrations near the dowel. Hence, the end and side distance requirements are more severe when loading as sketched in Figure 2.5 (b).

Roughly, the discussion of brittle global failures in dowel type connections can be divided into three groups. The first group includes brittle failures that are not premature, i.e. a brittle failure encountered after yielding stress is reached in the connectors. The second group is concerned with the alleged higher level of security bound up in a high degree of ductility. The third group covers real premature non plastic failures encountered before yielding stress is reached in the connectors.

The first group is clearly uninteresting and to some degree the same goes for the security concern. Though the connections are designed by use of plasticity theory very large plastic deformation capacity is not necessarily present. Generally wood constructions are brittle, hence a brittle behaviour of the connections is not necessarily prohibitive for the performance of the structure. The cases where the plastic capacity is not met before brittle failure clearly poses a problem for the current design practise. In the following, four of the strategies used to meet the problem of brittle failure are discussed:

- Other design criteria, i.e. instead of prescribing abundantly wood round the single connector a new set of brittle design criteria are superimposed to the plastic design criteria.
- Decreased global utilization, i.e. prescribing more slender dowels or larger end distance and spacing requirements.
- Enhancing the brittle strength by means of reinforcement of the wood.
- Enhancing the strength by production precision.

### 2.2.2 Reduction for multiple dowels

Brittle splitting is often seen in connections with multiple dowels in a row. This is generally not taken into consideration by prescription of larger end distance and spacing requirements but by a reduction to the yield strength of the individual dowel as function of the number of dowels in a row. This may seem harmless but in reality by use of the reduction factor method the plastic design criteria is tacitly abandoned in favour of an unknown but empirically based brittle strength model.

In the pre-version of the Eurocode, (CIB 1983), it is recommended to calculate the effective number of dowels when more than four dowels are in a row by:

$$n_{ef} = 4 + \frac{2}{3}(n - 4) \quad (2.10)$$

In the latest version of the Eurocode, (EC5-1 1995), the recommendation is changed to:

$$n_{ef} = 6 + \frac{2}{3}(n - 6) \quad (2.11)$$

In the bridge part of the Eurocode, (EC5-2 1997), the recommendations are tightened:

$$n_{ef} = 2 \left( \frac{n}{2} \right)^{k_j \lambda_r}, \quad (2.12)$$

where  $k_j$  includes the fabrication inaccuracy and takes the value 0.8 and  $\lambda_r$  is the relative slenderness ratio between the actual slenderness ratio  $\lambda = t/d$  and the slenderness ratio corresponding to highest failure mode.

In the Canadian design rule for multiple-dowels-in-a-row, (O86.1-94 1994), a reduction factor in form of an effective number of dowels in a row,  $n_{ef}$ , is given as:

$$n_{ef} = 0.33 k_m \frac{t^{0.5}}{d} \frac{a_1^{0.2}}{d} n^{0.7}, \quad (2.13)$$

where  $k_m$  includes number of rows and  $a_1$  is dowel spacing. While discussing the Canadian design rule Smith (1993) sums up the adjustment factor discussion:

Length-of-row adjustments for bolted connections [...] are recognized as an interim step pending an improved understanding of mechanisms involved when fasteners interact with each other or boundaries of members.

Jorissen (1998) has conducted a large experimental work on double shear timber to timber connections with special emphasis on the effect of multiple dowels in a row. The test series comprises more than 1000 tests on multiple dowel connections where both inter dowel spacing, end spacing, and dowel slenderness ratio are varied. The experimental findings have resulted in a well documented proposal for the effective number of dowels,  $n_{ef}$ , when  $n$  dowels are in a row with dowel spacing  $a_1$ . In the form Jorissen has chosen for  $n_{ef}$  in (Madsen 2000) the proposal reads:

$$n_{ef} = k_m n^{0.9} \left( \frac{a_1}{10d} \right)^{0.25}, \quad (2.14)$$

where  $k_m$  is a factor taking into account the effect of multiple rows, for one row  $k_m = 1$  and for two rows  $k_m = 0.9$ . In order to eliminate the reduction of the strength of a single dowel the proposal (2.14) is by Larsen & Riberholt (1999) given the form:

$$n_{ef} = 1 + 0.5 (n - 1)^{0.9} \left( \frac{a_1}{d} \right)^{0.3} \quad (2.15)$$

Traditionally it is believed that the strength reduction in multiple dowel connections is due to uneven load distribution between dowels because of inaccurate hole positions. However, Jorissen shows that fabrication tolerances are not important to the strength of multiple dowel connections, at least when the dowels are sufficiently slender. Further, Jorissen shows by means of numerical simulations that the tension stress state perpendicular to the grain is affected by the number of dowels in row, and that this probably is the reason for the strength reduction in multiple dowel connections.

It is as mentioned not a new feature to work with strength reduction in multiple dowel connections. However, reduction of the dowel strength as function of inter dowel spacing as done by Jorissen naturally brings about the question whether inter dowel spacing is a variable with which the dowel strength varies or whether it is a limit securing sufficient brittle capacity of the cross section to ensure plastic dowel failure.

Documentation of the failures and load displacement curves are not given in (Jorissen 1998). This makes it difficult to assess if the reduction proposal reduces single dowel yield capacity or single dowel strength determined on basis of premature brittle failures.

As strength reduction due to multiple dowels is a known phenomenon it has to be faced and work with as done by Jorissen. On the other hand one could from an engineering point of view go to far in the direction pointed by Jorissen. What the traditional theory states is that the strength can be predicted on a very firm basis provided the designer stays within a domain where the theory is valid, i.e. within a domain where spacing and end distances are sufficient. Jorissens experiments transcend the borders of the traditional yield theory and comes up with a new theory explaining brittle type failures in dowel type connections.

### 2.2.3 Increasing slenderness ratio

Another approach to brittle type failures is to demarcate and stay within the domain where the plasticity theory is valid. In (Blass, Ehlbeck & Rouger 1999a) it is suggested to simplify the design of dowel type fasteners by encouraging the designer to use slender fasteners by prescribing minimum timber thicknesses ensuring at least one hinge in the

fastener in each timber member. The advantage of this approach is, besides the simplified design rule, that the tendency for premature splitting is reduced as failure modes with at least one plastic hinge in each timber member utilizes the timber less severe than rigid failure modes.

In the literature it is often said that slender dowel connections are more ductile than stout dowel connections. The increased ductility with increased slenderness is not predicted by the plasticity theory. However, when increasing the slenderness beyond mode I failure the load transfer per timber thickness,  $F_y/t$ , decreases for increased slenderness. Due to this the brittle capacity relative to load transferred per shear plane increases with increased slenderness. This increased brittle capacity makes room for larger plastic deformations in connections with slender dowels. Hence, prescribing slender dowels corresponds to a prescription of smaller average stresses in the cross section, an objective which may also be obtained by prescribing increased spacing.

It should be observed that a slenderness ratio just resting on the geometrical relation  $t/d$  neglects the influence of the dowel material on the effective slenderness ratio. Hence, the more comprehensive slenderness ratio  $\lambda_r = \lambda/\lambda_y$  such as used in (2.12) may be more appropriate. This is implicitly included in the Danish code (DS 413 (5.1) 1999), where the spacing in the fibre direction is to be increased with the factor  $\sqrt{f_y/240}$  when steel with yield strength in excess of 240 MPa is used.

#### 2.2.4 Wood reinforcement

A third approach to brittle failure in connections is to enhance the brittle capacity by means of reinforcement. Larsen & Enquist (1996) reports a test series on wood reinforced with glass fibres glued to the side of the wood members with a polyester glue. The finding is for dowels that the ductility is increased and a marginal strength increase is observed and the spacing requirements can be reduced when using reinforced members compared to unreinforced. This observation corresponds to an increase in the brittle strength of the wood members obtained by the reinforcement. For nails the strength is increased more than 50 % probably because the reinforcement prevents the nails from cleaving the wood in the embedment zone.

Similar findings are reported in (Haller, Chen & Natterer 1996) and (Chen, Natterer & Haller 1994). Haller et al. (1996) also uses wood densification to enhance the connector performance. Generally, the increase in strength properties follows the degree of densification.

### 2.2.5 Production precision

Enhanced precision in the fabrication of joints is a fourth means to enhance the strength and reduce the probability of a brittle premature splitting failure. Such enhanced precision is implemented in the "Blumer-System-Binder". The system uses CNC-machinery to drill holes in wood and steel, otherwise the principle is to use slender dowels in geometrical configurations with slotted in steel plates securing mode III failures, such as reported by Gehri in (Madsen 2000).

The principle behind the "Bertsche System" is also partly enhanced precision as a round steel member with multiple holes for dowels in two orthogonal directions is casted with a special mortar securing contact on all surfaces (Bertsche 1993).

The use of Fibre Reinforced Plastics as substitute for steel in slotted in plates allows drilling of holes for dowels directly through wood and plate in one process and promotes hence a higher level of precision opposed to the traditional production method, where plate and wood are produced in two separate processes.



## Chapter 3

# Embedment and dowel capacity

### 3.1 Embedment

The embedment strength or the embedding strength is an artificial material strength parameter gained in a specific geometric configuration, where a stiff element is resting on the inner rim of a hole in a piece of timber. Quoting from the definition clause of EN 383 (1993), the embedding strength is defined as:

Average compressive stress at maximum load in a piece of timber or wood based sheet product under the action of a stiff linear fastener. The fastener's axis is perpendicular to the surface of the timber. The fastener is loaded perpendicular to its axis.

#### 3.1.1 Embedment strength

The embedment strength is closely related to the more straight forward compressive strength parameters of wood, but it is of course influenced by the uneven stress distribution below the fastener. In directions other than the fibre direction the embedment strength is also influenced by the effects of a more complicated load bearing – in danish known as "svellebæreevne". Beside the principal load bearing mechanism there is in this case two factors which increase the strength when the loaded area is smaller than the loaded member, namely:

- Load bearing diffusion beneath the loaded surface.
- Load bearing contribution from unbroken fibres running beneath the loaded surface into unloaded material.

### Old Danish code

In the interpretation of the old Danish Code of Practice (DS 413 1982) given in (Larsen & Riberholt 1991) it was suggested to calculate the embedment strength,  $f_h$ , directly by use of the compressive strength of the wood  $f_{ved}$ :

$$f_h = 0.67 f_{ved} \cdot f(d, \alpha) \quad (3.1)$$

where  $f(d, \alpha)$  is a function of diameter,  $d$ , and angle between load and fibre direction,  $\alpha$ :

$$f(d, \alpha) = \frac{k_{90}}{k_{90} \cos^2 \alpha + \sin^2 \alpha} \quad (3.2)$$

with:

$$k_{90} = 0.45 + 8d^{-1.5} \quad (3.3)$$

The factor 0.67 in (3.1) is an empirical reduction factor due to stress concentrations. The strength,  $f_{ved}$ , is the compressive strength in the fibre direction, hence  $f_{h,0} = 0.67 f_{ved}$ . Equation (3.2) is in principle Hankinsons strength interpolation formula where  $k_{90}$  given in (3.3) is the ratio  $f_{c,90}/f_{c,0}$  bringing into consideration that  $f_{c,90}$  is not linear in the width of the loaded area, due to the effects of "svellebæreevne".

### New Danish code

In the new Danish Code of Practice (DS 413 (5.1) 1999) and it's interpretation in (Larsen & Riberholt 1999) the term  $0.67 f_{ved}$  in (3.1) is substituted with a reference to the test standard for embedment strength (EN 383 1993). Alternatively it is in accordance with the Eurocode and with reference to (Whale, Smith & Larsen 1987) suggested to determine the embedment strength as function of density and dowel diameter.

### Eurocode

The Eurocode (EC5-1 1995) contains two ways of obtaining the embedment strength, either from experiments by use of EN 383 (1993) or indirectly by use of wood density and dowel diameter:

$$f_{h,0} = 0.082(1 - 0.01d)\rho, \quad (3.4)$$

The diameter angle function in the Eurocode uses Hankinsons formula and a linearisation of the dowel diameter dependency:

$$f(d, \alpha) = \frac{1}{k_{90,EC5} \sin^2 \alpha + \cos^2 \alpha} \quad (3.5)$$

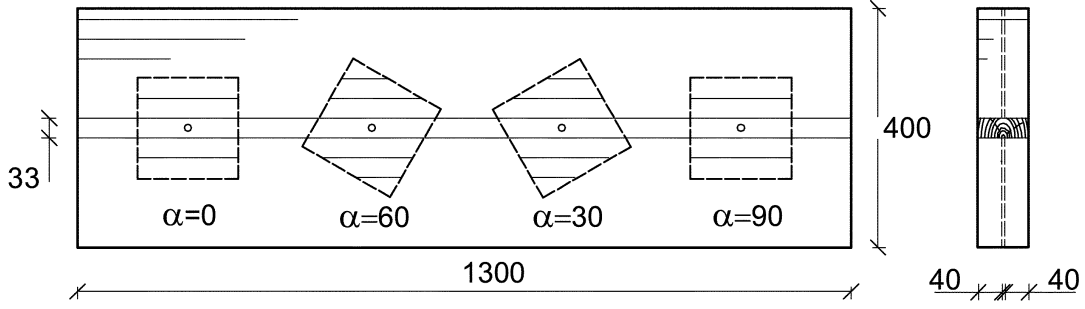


**Figure 3.1:** Plan for cutting embedment specimens from plank, measures in mm.  
All holes for embedment tests are in the same unjointed board.

The factor  $k_{90,EC5}$  is a linearisation of the inverse of  $k_{90}$ :

$$k_{90,EC5} = 1.35 + 0.015d \quad (3.6)$$

## 3.2 Embedment tests

In the proceeding sections test series on the embedment strength are presented. The aim is to generate a yield surface for the embedment strength, and to try to link simple physical wood properties with embedment properties.

### 3.2.1 Material and method

Embedment strength has been determined using specimens cut from the remains of the test material used for the full scale tests of dowel type connections presented in Chapter 5. The wood material was ordinary commercial glulam beams L40-L30 produced with lamellas of spruce (*Picea abies*).

### Randomized complete block test

A randomized complete block test of the embedment strength at different angles was made taking specimens from beams with outer dimension as shown in Figure 3.1. Each plank was halved and four specimens were cut at different angles to grain from each side of the plank. The specimens were cut so the central lamella with the holes for the embedment tests was one unjointed board, i.e. each plank yielded two sets of specimens testing embedment at four angles on the same plank, Figure 3.1. The geometry of the specimen is shown in Figure 3.2. A 12 mm steel dowel was used as embedder and the requirements to maximum width and minimum end and side distances given in the test

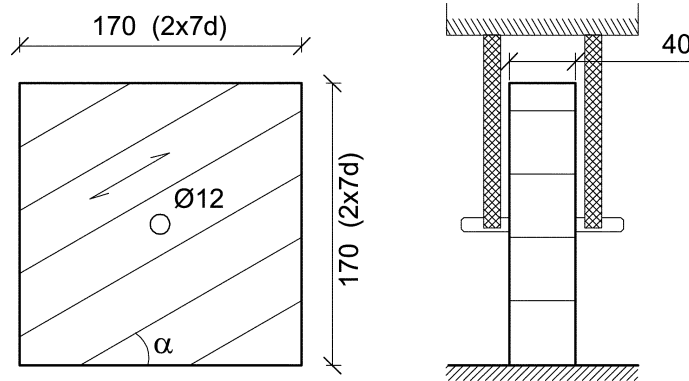


**Figure 3.2:** *Geometry for embedment specimens tested at different angles to grain.*

method standard for embedment strength (EN 383 1993) are all fulfilled. Five different planks were used and the whole series constitute a randomized complete block test with five blocks of four treatments and two repetitions within each combination of block and treatment, i.e. angle.

The specimens were cut and tested at equilibrium with 65% RH. The tests were deformation controlled with a deformation rate of 0.015 mm/s - irrespective of grain angle. The test machine used, a mechanical INSTRON 6025, and the test equipment are infinitely stiff compared to the embedment and the deformations in the transitions were negligible compared to embedment set, hence the traverse position is used as measure for embedment deformation.

### Additional tests

Additional embedment tests have been made, some with geometry as shown in Figure 3.2 and some with slightly different geometry. A total of approximately 30 additional embedment tests have been made primarily in the grain direction and perpendicular to the grain direction. The material for these tests were taken from the same batch of material as material for specimens in the complete block test.

### 3.2.2 Results

#### Randomized complete block test

Representative examples of failures from the complete block test are shown in Figure 3.3. In Figure 3.4 all stress displacement curves are shown grouped by angle. The transition

$\alpha$ [°]	$f_h$		$f_{h,u2}$		$f_{h,y5}$		$K_E$		$K_{post}$	
	mean	stdev	mean	stdev	mean	stdev	mean	stdev	mean	stdev
0	32.2	4.9	32.2	4.9	31.3	5.8	26.6	7.1	-0.13	0.32
30	24.6	3.1	24.7	2.9	25.9	3.8	27.9	6.6	0.23	0.43
60	18.7	4.4	18.3	3.2	21.6	4.8	15.2	2.0	0.63	0.39
90	14.3	2.6	15.4	2.4	21.8	3.7	11.9	1.8	1.61	0.26

**Table 3.1:** *Embedment strength, [MPa], and stiffness, [MPa/mm], at different angles to grain.*

from almost ideal plasticity parallel to grain towards hardening plastic behaviour in the transverse direction is seen.

The stress displacement curves in Figure 3.4 have been analysed using a procedure illustrated in Figure 3.5 and the following quantities have been determined:

$f_h$  Embedment strength determined as the maximum stress in case of  $\alpha = 0^\circ$  or as the stress corresponding to the intersection of the bilinearisation of the curves.

$f_{h,u2}$  Embedment strength determined as the stress at two mm displacement measured from the intersection between the abscissa and the linear regression of the initial elastic part of the curves, see Figure 3.5(b). In the case of  $\alpha = 0^\circ$   $f_{h,u2} = f_h$ , but for other angles  $f_{h,u2} > f_h$ . The quantity  $f_{h,u2}$  has been measured in order to obtain a more consistent measure of the embedment strength, as strong hardening generally punishes the value of  $f_h$ . Further it was observed that the value of  $f_h$  for  $\alpha \neq 0^\circ$  was determined at displacements smaller than the displacement for  $f_{h,0}$  which is unfair to  $f_{h,\alpha \neq 0}$ .

$f_{h,y5}$  Embedment strength determined as the strength corresponding to five mm yielding measured from the displacement at  $f_h$ , see Figure 3.5.

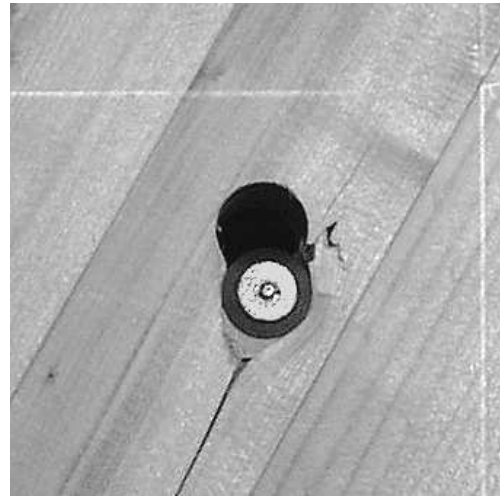
$K_E$  Stiffness at the initial linear part of the curves.

$K_{post}$  Stiffness of the curves between  $f_{h,u2}$  and  $f_{h,y5}$ .

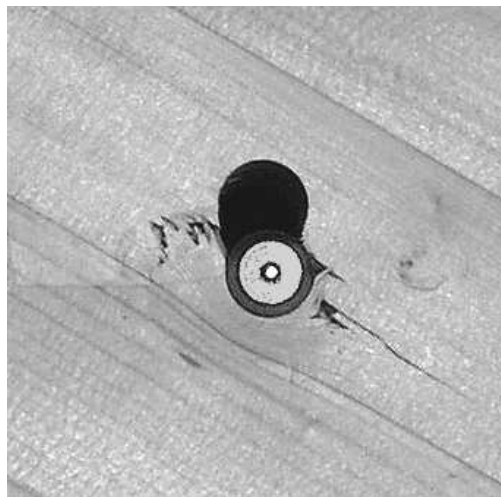
Mean value and standard deviation of the quantities have been determined on the 10 replicates in each block-angle combination, Table 3.1. Beside the significant dependency upon angle, listed in the table and shown in Figure 3.4, a strength dependency upon block, i.e. origination board, is seen. An ANOVA on the complete block test has been



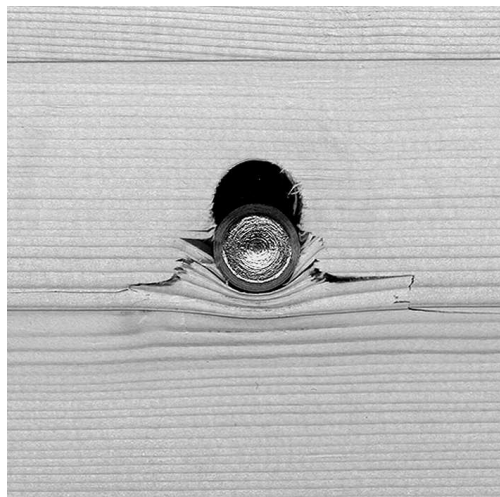
(a)  $\alpha = 0^\circ$



(b)  $\alpha = 30^\circ$

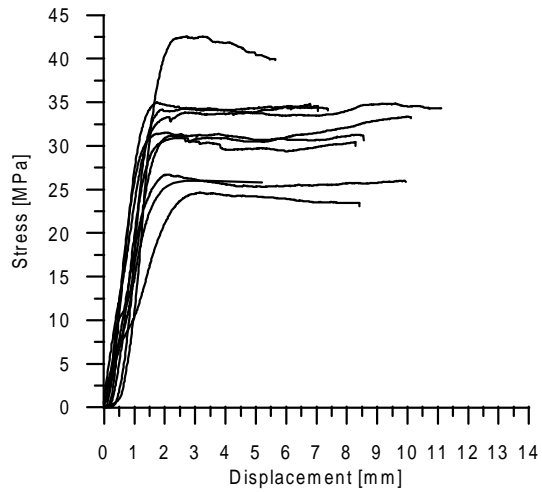
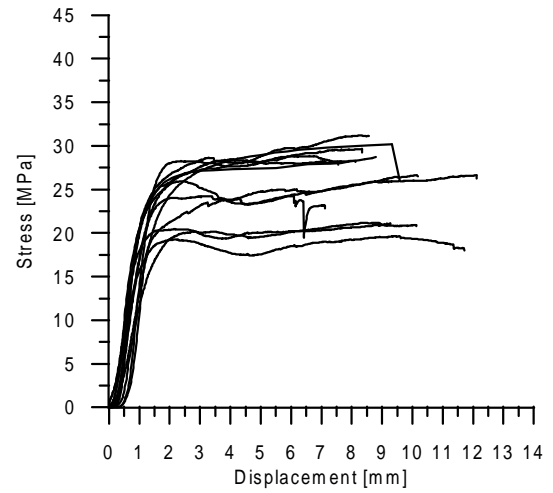
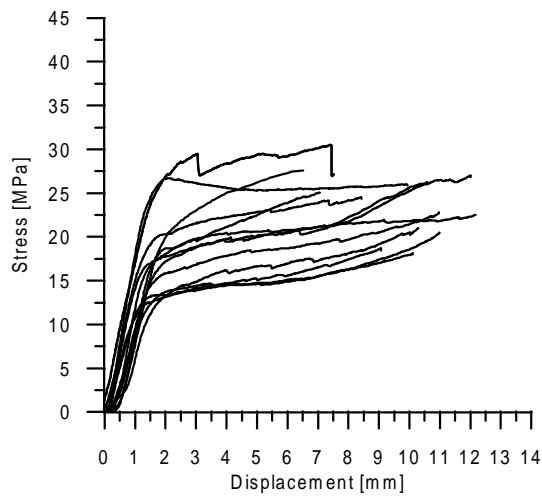
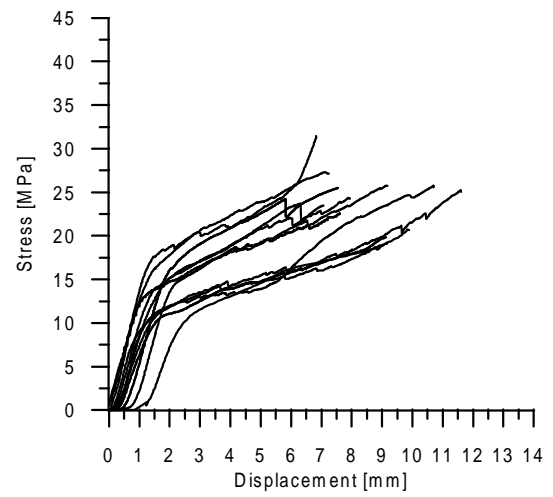


(c)  $\alpha = 60^\circ$



(d)  $\alpha = 90^\circ$

**Figure 3.3:** Failed embedment specimens tested at different angles to grain.

(a)  $\alpha = 0^\circ$ (b)  $\alpha = 30^\circ$ (c)  $\alpha = 60^\circ$ (d)  $\alpha = 90^\circ$ **Figure 3.4:** *Stress displacement for all embedment specimen.*

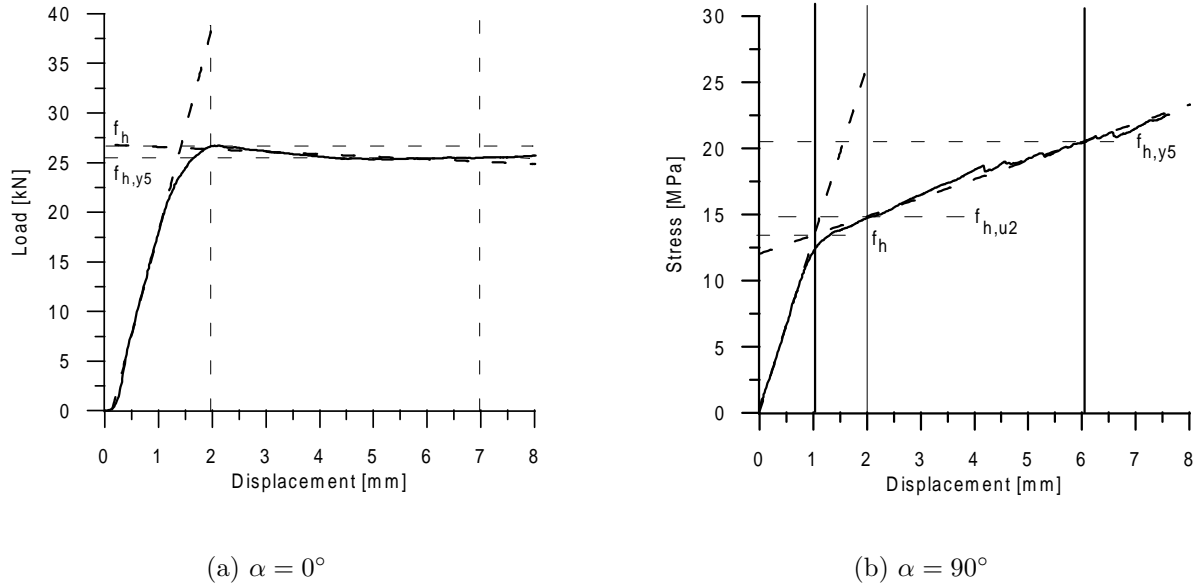


**Figure 3.5:** Procedure for determination of strength and stiffness.

run in SAS with respect to  $f_h$ ,  $f_{h,u2}$ ,  $f_{h,y5}$ ,  $K_E$  and  $K_{post}$ . The analyses show that the effect of block is significant at levels higher than 98% in all instances. The effect of board is not totally consistent between the investigated quantities but board 6 always yields the lowest values and board 12 or 8 the highest. An example of the analysis of variance using the model in (3.7) is given in Table 3.2.

$$Y_{ijk} = \mu + \alpha_i + b_j + E_{ijk} \quad (3.7)$$

$$\text{where: } \begin{cases} \mu & \text{overall mean} \\ \alpha_i & i = 1, 2, 3, 4 \quad \text{effect of angle} \\ b_j & j = 1, 2, 3, 4, 5 \quad \text{effect of board} \\ E_{ijk} & k = 1, 2 \quad \text{random error} \end{cases}$$

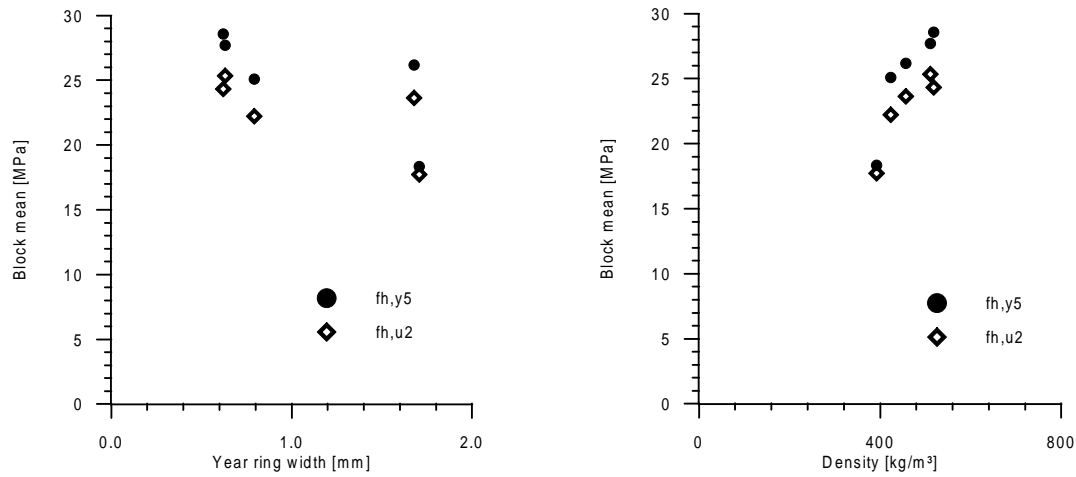
The source of between boards variation in  $f_h$ ,  $f_{h,u2}$ ,  $f_{h,y5}$ ,  $K_E$  and  $K_{post}$  is sought in difference in the bulk density of the specimen, i.e. the mean beam density, or in the density or annual ring width specifically of the loaded board, see Figure 3.1. In Table 3.3 is given the block mean of  $f_{h,u2}$ , which is a somewhat artificial quantity just serving to show the strength variation between blocks. The table also gives bulk specimen density, and density and year ring width of the loaded board. The block mean in Table 3.3 shows no variation with bulk specimen density, but the board properties may serve as explanation

Source of Variation	Sum of Squares	Deg. of Freedom	Mean Square	$F_0$	P-Value
Angle	1834.7	3	611.57	138.1	> 99.99%
Board	334.7	4	83.68	18.9	> 99.99%
Error	141.7	32	4.43		

**Table 3.2:** *Analysis of variance of  $f_{h,u2}$  as function of angle to grain and board.*

Block [no.]	$f_{h,u2}$	Bulk density, $\rho_{12}$		Board density $\rho_{9,5}$		Ring width	
	Mean	Mean	stdev	Mean	stdev	Mean	stdev
12	25.4	473	9	511	23	0.63	0.1
8	24.3	478	8	518	13	0.62	0.05
13	23.6	459	11	456	10	1.68	0.2
10	19.9	470	10	423	17	0.79	0.4
6	17.7	463	7	392	9	1.71	0.1

**Table 3.3:** *Block variation of  $f_{h,u2}$ , [MPa], with bulk specimen density, board density, [kg/m<sup>3</sup>], and annual ring width, [mm], of the loaded board.*



(a) Board mean versus year ring width of board

(b) Board mean versus board density

**Figure 3.6:** *The variation between board mean strength, and board density or year ring width.*

for the block effect. In Figure 3.6 the variations in block mean of  $f_{h,u2}$  and  $f_{h,y5}$  are given as functions of both density and year ring width of the loaded board. Clearly, the loaded board density is the best parameter to account for the block effect observed.

In Table 3.4 the results from the additional embedment tests have been merged with the results from the complete block test. The merged results form a better statistical basis and they deviate little from the results from the block test alone.

$\alpha$ [°]	n	$f_h$		$f_{h,u2}$		$f_{h,y5}$		$K_E$		$K_{post}$	
		mean	stdev	mean	stdev	mean	stdev	mean	stdev	mean	stdev
0	19	31.5	4.1	31.5	4.1	30.1	4.6	31.8	9.1	-0.13	0.32
30	12	24.3	3.4	24.4	3.1	25.5	4.1	27.2	6.4	0.22	0.40
60	12	17.8	4.5	17.5	3.4	20.8	4.8	15.0	2.0	0.63	0.36
90	23	13.3	3.1	15.1	3.0	21.8	4.1	14.4	5.2	1.88	0.67

**Table 3.4:** *Embedment strength, [MPa], and stiffness, [MPa/mm], at different angles to grain, n is number of test at each angle.*

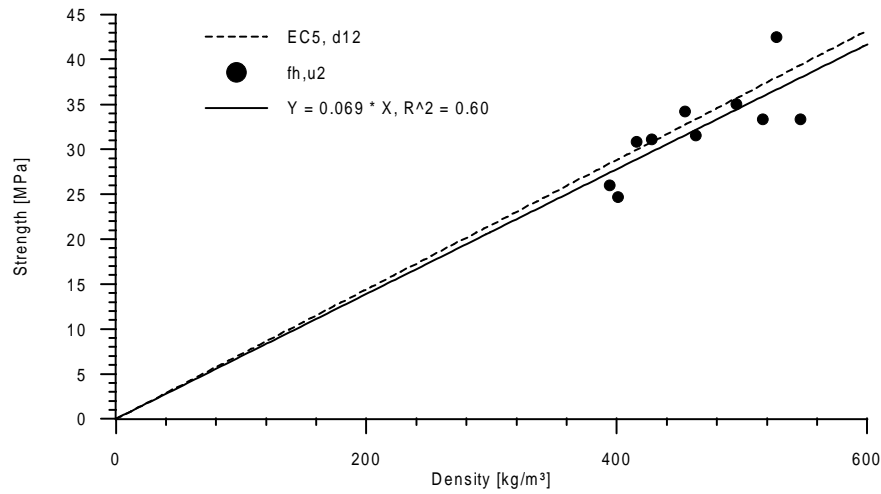


**Figure 3.7:** The variation of  $f_{h,0}$  with board density compared with the prescription in EC5-1.

### 3.3 Embedment modelling

#### 3.3.1 Strength and code rules

##### Fibre direction

The embedment strength in the fibre direction,  $f_{h,0}$ , is found to have a mean value of 31.5 MPa. According to the old Danish Code, (3.1), this corresponds to a compressive strength in the fibre direction of 47 MPa, which is to be expected for the Norway spruce used.

By use of the Eurocode, the embedment strength can be determined from the mean density,  $\rho_{12} = 470 \text{ kg/m}^3$ , giving  $f_{h,0} = 33.8 \text{ MPa}$ , where the density is the mean bulk density of all specimens. The Eurocode expression, (3.4) can for a 12 mm dowel be written:

$$f_{h,0} = 0.072\rho, \quad (3.8)$$

this correlation is confirmed experimentally in Figure 3.7 where the mean of  $f_{h,0}$  from each board is given as function of board density.

##### Perpendicular to fibre direction

For a 12 mm dowel at  $90^\circ$  to grain the diameter-angle function, (3.5), in the Eurocode gives the following reduction factor:

$$f(d12, \alpha90) = 0.654, \quad (3.9)$$

which is the reduction of  $f_{h,0}$  used to obtain the value of  $f_{h,90}$ . By use of the experimental value of  $f_{h,0}$ , the strength perpendicular to grain is predicted to  $f_{h,90} = 20.6$  MPa. According to the results presented in Table 3.4, this value overestimates the experimental value of  $f_{h,90}$  with 55 % and the experimental value of  $f_{h,90,u2}$  with 36 %. It corresponds however to the experimental value of  $f_{h,90,y5}$  within 6 %.

The overestimations pose a modelling problem as utilization of the predicted  $f_{h,90}$  entails permanent damage already at a 50 % stress level. Further, it is questionable whether the value of  $f_{h,90,y5}$ , which in the reported experiments is obtained in compression, can be obtained in a tension test without premature splitting of the wood.

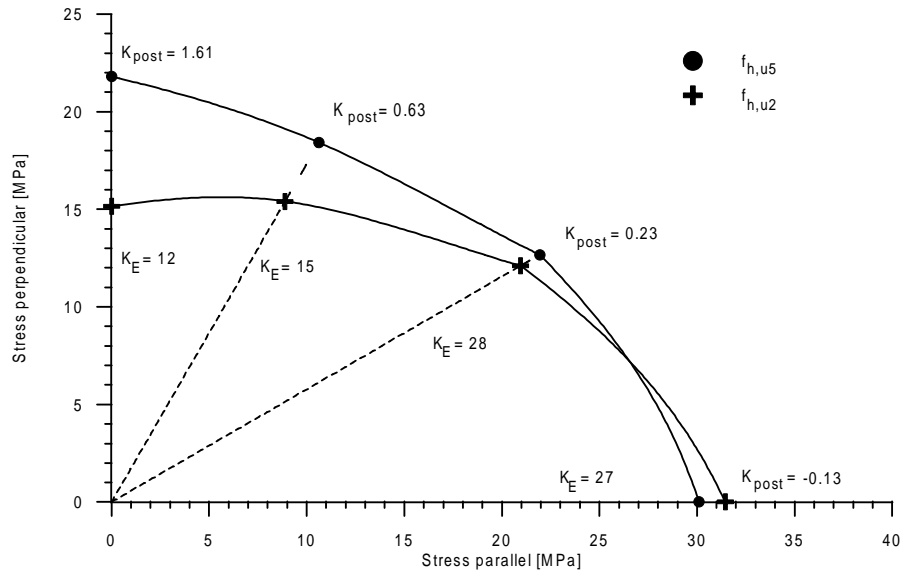


**Figure 3.8:** Yield surface based on experiments with stiffness  $K_i$ , [MPa/mm], in four directions in both the elastic and plastic regions.

### 3.3.2 Yield surface

Figure 3.8 presents a yield surface for the embedment established from the results of the complete block test, Table 3.1. The yield surface utilizes an idealization into an elastic region with stiffness  $K_E$ , and a plastic region with hardening or softening and stiffness  $K_{post}$ . The yield surface is drawn by a simple spline function both at onset of yielding,  $f_h$ , and after 5 mm plastic deformation,  $f_{h,y5}$ .

### 3.4 Dowels

The bending capacity of dowels is the counterpart of the embedment strength. Johansen (1941) uses the elastic bending capacity of the dowel whereas in the Eurocode and in the Danish code the capacity of the dowel is determined on basis of the fully developed plastic state. For a dowel with circular cross section and diameter  $d$  the full yield capacity is:

$$M_y = f_{y, \text{steel}} \frac{1}{6} d^3, \quad (3.10)$$

where  $f_{y, \text{steel}}$  is the yield strength of the dowel steel. In (EC5-1 1995)  $f_{y, \text{steel}}$  is suggested determined as:

$$f_{y, \text{steel}} = 0.8 f_{u, \text{steel}}, \quad (3.11)$$

where  $f_{u, \text{steel}}$  is the tensile strength of steel. In (Jorissen & Blass 1998) it is confirmed that the yield strength determined according to (3.11) is coinciding with the yield strength determined in bending at plastic deformation with  $45^\circ$  mutual bending angle. It is observed that dowel yield moment is a function of bending angle,  $M_y(\alpha)$ , both due to material and geometrical hardening. This poses a problem as pointed out by Blass, Bienhause & Krämer (2000), as the bending angle at failure generally is much lower than  $45^\circ$ .

In (Blass et al. 2000) it is suggested to determine the bending capacity of the dowel corresponding to the bending angle at failure. The theoretical bending angle at failure is determined at a prescribed deformation assuming ideal stiff-plastic behaviour of wood and dowel. The bending angle,  $\alpha$ , depends upon the wood properties and the dowel yield moment,  $M_y(\alpha)$ . Hence, an iterative procedure is employed to determine  $M_y(\alpha)$  in the connection by use of  $M_y(\alpha)$  determined in a bending test of dowels. This iterative method is clearly needed when the strength is to be evaluated at large deformations and hardening is present in the dowel.

#### 3.4.1 Dowel bending tests

In order to determine the bending capacity of the dowels used in the full scale tests reported in Chapter 5, three point bending tests have been performed. The dowels were taken to failure with a central load in a 100 mm span. Load and central deflection was recorded. The following three types of dowels were tested with 9 repetitions for each type:

- Electro galvanized standard BMF dowels,  $d12$ . These dowels are used in full scale tests in Chapter 5.

	$M_y$	$M_y(\alpha = 5^\circ)$
Electro galvanized, 12 mm	180	203
hot dip galvanized, 12 mm	160	184
Slender dowels, 6 mm	24.5	28

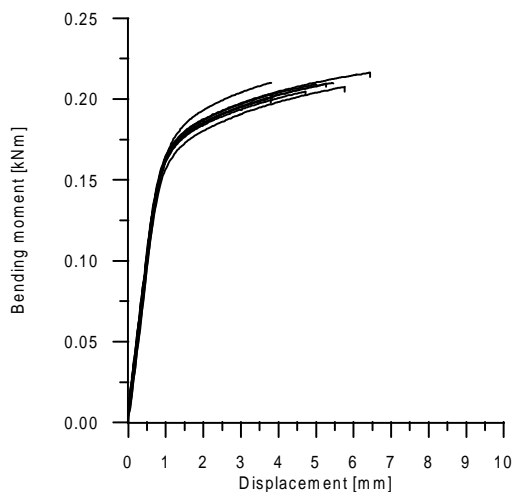
**Table 3.5:** Yield capacity of dowels, [Nm].  $M_y$  corresponds to initial yielding and  $M_y(\alpha = 5^\circ)$  is the bending capacity at a rotation angle of  $5^\circ$ .

- Hot dip galvanized standard BMF dowels,  $d12$ . These dowels are the most frequently used in timber construction
- Slender  $d6$  dowels with high strength corresponding to the dowels used in the block test of plastic connector failure modes mentioned in Chapter 2.

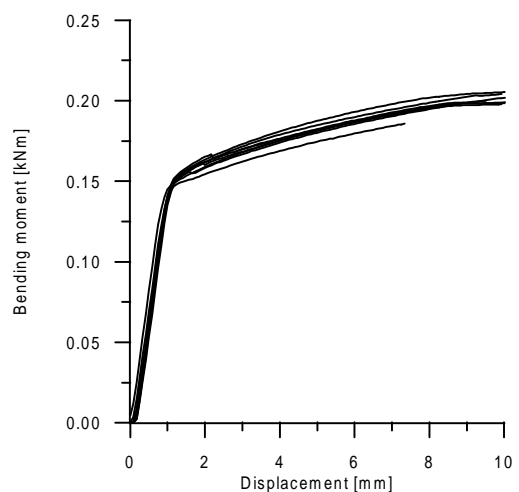
### 3.4.2 Determination of bending capacity

In Figure 3.9 (a)-(c) bending moment versus central deflection for the three dowel types are given. Figure 3.9(d) shows bending moment versus plastic rotation, the curve has been constructed by subtracting all elastic deformation in Figure 3.9(a) from the moment deformation curve. The rotation angle  $\alpha$  is determined from the geometry,  $\tan(\alpha) = 2 \text{ deflection} / \text{span}$ . It is noted that the  $M_y(\alpha)$  relation in (Blass et al. 2000) includes elastic deformation.

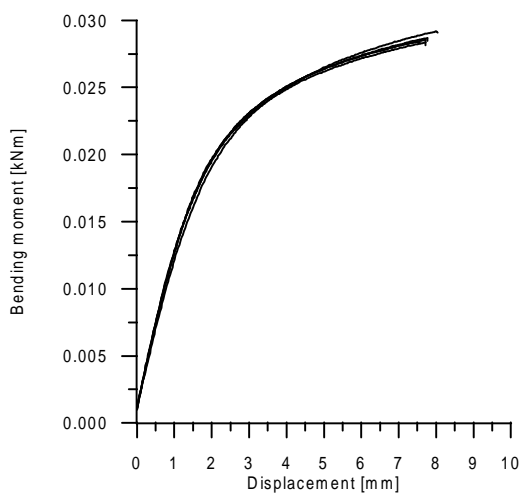
In Table 3.5 the values of the bending moment in the transition between elastic and plastic behaviour,  $M_y$ , is given. With the used test geometry and for the 12 mm dowels this corresponds to 1 mm deflection, as seen in Figures 3.9(a) and (b).



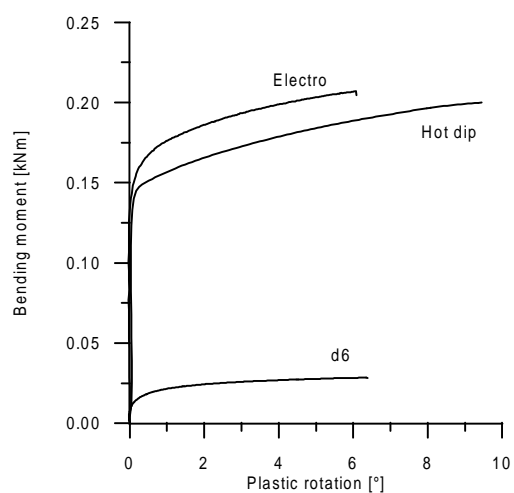
(a) Electro galvanized standard BMF dowels,  $d_{12}$



(b) Hot dip galvanized standard BMF dowels,  $d_{12}$



(c) Slender  $d_6$  dowels



(d) Plastic rotation of dowels

**Figure 3.9:** *Bending moment versus central deflection / plastic rotation in dowel bending tests*



## Chapter 4

# Tension splitting due to transverse load

In the preceding chapter it was shown that the embedment strength perpendicular to grain is overestimated by the rules of the Eurocode. The scope of this chapter is to demonstrate that for a simple dowel connection with slotted-in steel plates the empirical embedment strength is not even reached at failure, as this is a premature tension splitting rupture perpendicular to the grain.

### 4.1 Material and methods

Tension splitting in dowel type connections due to transverse load has been investigated on planks consisting of two boards glued together. The test material is taken from a batch of Norwegian grown Norway spruce *Picea abies*. A total of 3 m<sup>3</sup> of 38 x 150 mm boards with an approximate length of 5 m were subdivided into three groups using an annual ring width criterion. In each group the boards were paired and glued sapwood to sapwood yielding planks with symmetrical cross sections, which were subsequently planned to final dimensions of 50 x 130 mm. On specimens from this batch of material three types of tests have been made:

- Four-point bending tests on dowelled connections
- Embedment and small compression tests
- Tension perpendicular to grain tests

The special symmetrical cross section made it possible to design tests primarily utilizing the radial oriented material in the centre of the cross section.

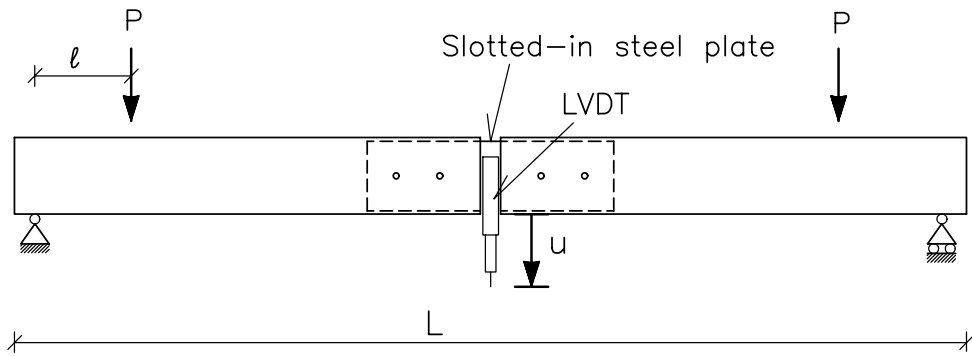


**Figure 4.1:** Four point bending test set-up.

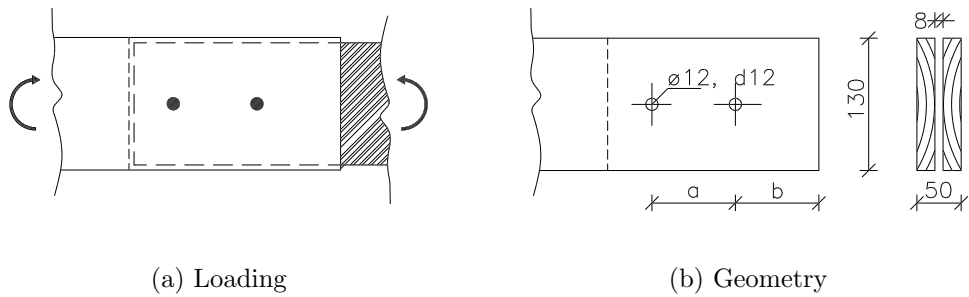


**Figure 4.2:** Geometry and loading of specimens utilizing  $f_{h,90}$ .

#### 4.1.1 Bending tests

Four point bending tests in a test set-up as shown in Figure 4.1 with  $L = 1740$  mm and  $l = 270$  mm have been made on beams with a central slotted-in dowel type connection with geometry as shown in Figure 4.2(b). Only one joint was tested at a time, i.e. one side of the symmetrical set-up in Figure 4.1 was a steel dummy. Tests of the following joints have been performed:

- A total of 46 joints with a geometry as shown in Figure 4.2(b) with  $a = b = 7d$ , in equilibrium with 65 % RH.
- A total of 15 joints tested in a small block test covering three planks and three different joint geometries, i.e. the distances  $a$  and  $b$  take values of either 7 or 14  $d$ , in equilibrium with 65 % RH.

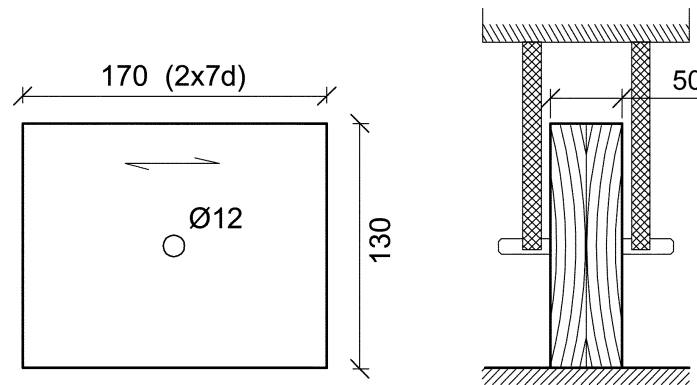


**Figure 4.3:** *Embedment tests in a radial plane of special glued beams.*

- A total of 8 joints with a geometry as shown in Figure 4.2(b) with  $a = b = 7d$ , in equilibrium with 85 % RH.

All joint tests were load controlled with a rate of 0.03 kN/s giving a test duration of approximately 180 seconds.

#### 4.1.2 Embedment and compression tests

Embedment tests perpendicular to the grain have been made in a radial plane using material from the planks tested in bending. The test geometry is given in Figure 4.3. Tests were conducted both on planks in equilibrium with 65 % RH and on planks in equilibrium with 85 % RH. Test conditions were as for the embedment tests described in Chapter 3. The oriented embedment tests utilizes the compressive strength in the tangential direction. As the compressive strength is dependent upon direction in the radial-tangential plane, a small indicative block test of the compressive strength in radial and tangential direction has been made. Small cubic specimens, with side measure 25 mm were taken from the same batch of material as the oriented embedment specimens and taken to failure in compression.

#### 4.1.3 Transverse tension tests

Material from 10 different planks from the batch of planks with symmetrical cross sections were used for short term testing of the strength perpendicular to the grain in the centre radial plane. The test series were conducted as a block test covering all planks with a total of 60 specimens at 65 % RH and 30 specimens at 85 % RH. The specimen geometry

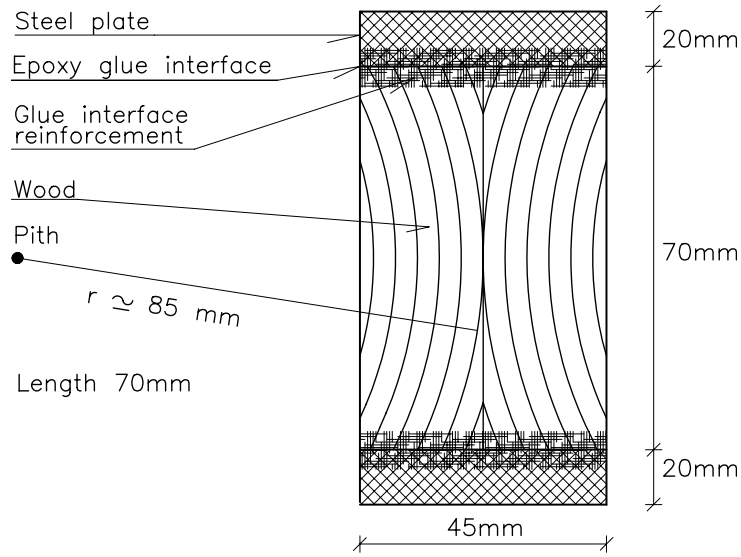


**Figure 4.4:** *Geometry of small specimen used in fatigue testing.*

and design were as shown in Figure 4.4. The load was applied in a double hinge set up at a stress rate of 0.026 MPa/s giving times to failure of approximately 100 s.

## 4.2 Results

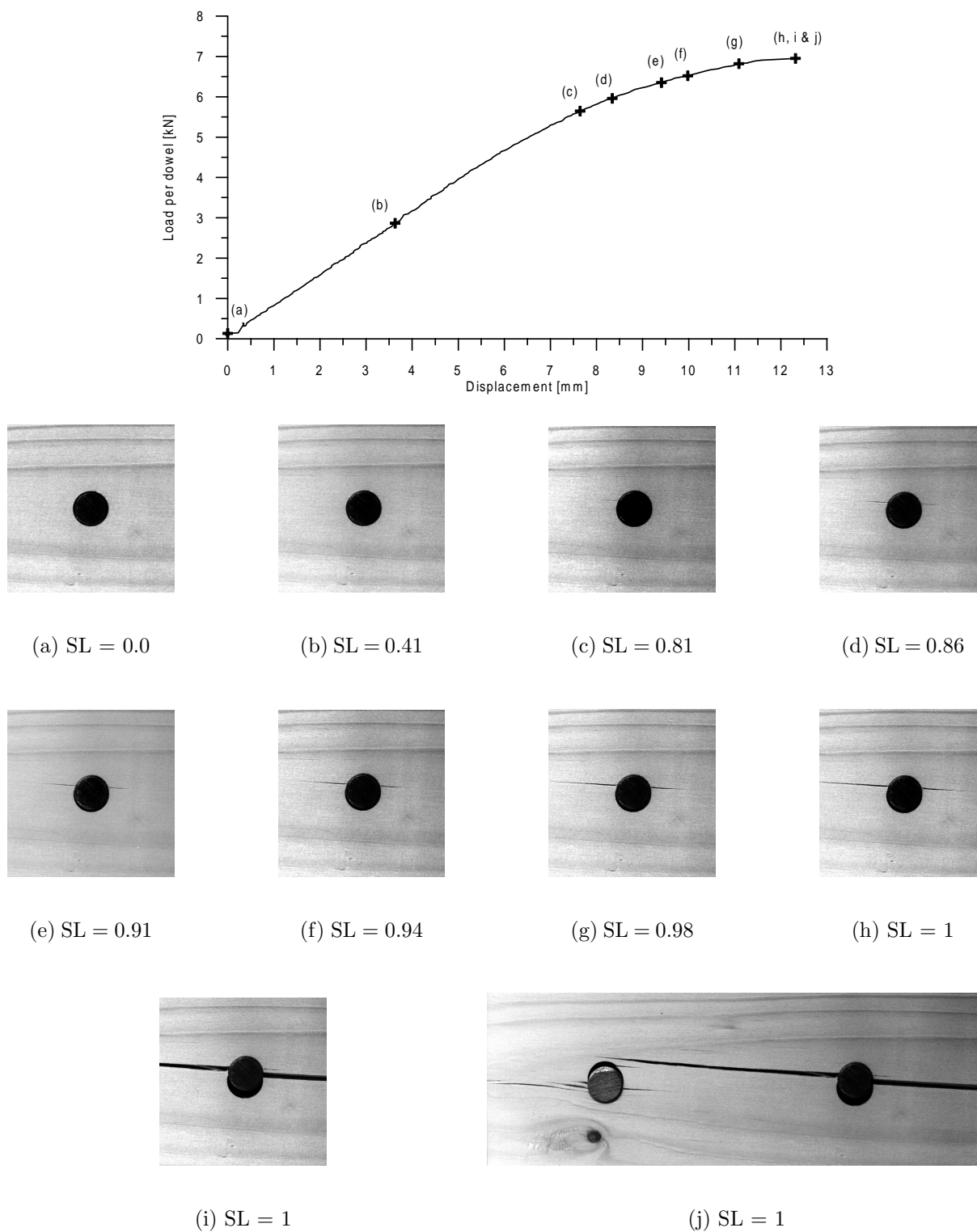
### 4.2.1 Bending tests

Table 4.1 lists mean value and standard deviation of the strength per shear plane,  $F_y$ , along with the density,  $\rho$ , of the wood used. No bending of dowels was observed and no embedment indentation was observed prior to splitting failure.

	n	Density, $\rho_{12}$		$F_{ult}$	
		mean	stdev	mean	stdev
65 % RH	46	473	32	3.70	0.44
85 % RH	8	457	23	3.68	0.34

**Table 4.1:** *Density, [kg/m<sup>3</sup>], ultimate strength pr. shear plane, [kN], of specimens taken to failure in 4-point bending at 65% RH or 85% RH.*

Figure 4.5 shows a typical load displacement curve along with photos of the dowel proximity taken at different stages of the test progression. It is clear that the failure is



**Figure 4.5:** Load displacement curve and tension crack development at various stages,  $SL = F/F_{ultimate}$ .

Dowel spacing	7d	14d	7d
End distance	7d	7d	14d
n	3	6	6
Mean	3.70	4.29	3.90
Stdev	0.49	0.15	0.34

**Table 4.2:** *Ultimate strength pr. shear plane, [kN], obtained with different dowel spacings and end distances.*

a tension splitting rupture. The non-linearity of the load displacement curve is initiated approximately in point (c) on the load-displacement curve, corresponding to a stress level, SL, equal to 80 % of the ultimate strength. From the photographs it is observed that this non-linear behaviour corresponds to the shown crack growth.

### Spacing variation

In the indication test of the influence of the spacing,  $a$ , and end distance,  $b$ , Figure 4.2, five specimens from each of three planks have been tested in a block test. The geometry combinations used and the resulting strengths are given in Table 4.2. It is seen that the strength for  $a = b = 7d$  is equal to the mean strength for the same geometry reported in the previous section. Increased inter-dowel spacing is seen to increase the ultimate strength whereas increased end distance has less pronounced effect on the strength.

A linear two-factor statistical model is used to analyze the strength response,  $F_{ijk}$ , from the effect of plank and the effect of joint geometry of the individual specimen:

$$F_{ijk} = \mu + p_i + g_j + E_{ijk} \quad (4.1)$$

$$\text{where: } \begin{cases} \mu & \text{overall mean} \\ p_i & i = 1, 2, 3 \text{ effect of plank} \\ g_j & j = 1, 2, 3 \text{ effect of joint geometry} \\ E_{ijk} & k = 1, 2 \text{ random error} \end{cases}$$

In the analysis the effect of joint geometry is a fixed effect. The effect of plank may be interpreted as a fixed effect due to characteristic plank properties, e.g. density. From bending tests with material from 11 different planks with 4 replicates in each it is known that the strength variation due to the effect of plank is significant at a level of confidence in excess of 99 %, as the scatter between planks is three times larger than the scatter within planks. This effect of plank is however poorly correlated with the density. Table

Source of Variation	Sum of Squares	Deg. of Freedom	Mean Square	$F_0$	P-Value
Board	3.63	2	1.81	6.05	> 97.5%
Joint geometry	4.30	2	2.15	7.17	> 97.5%
Error	3.04	10	0.30		

**Table 4.3:** Analysis of variance of strength as function of geometry.

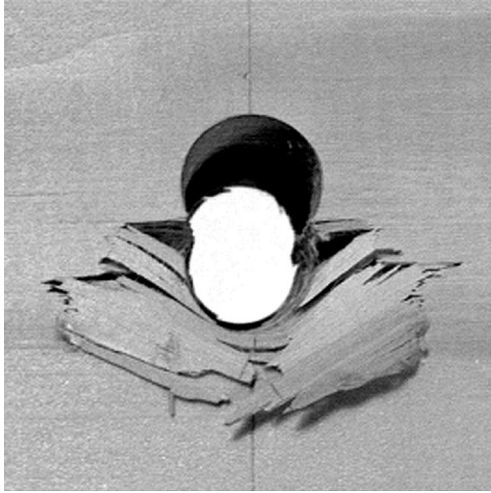
		Density, $\rho_{12}$		$f_{h,u2}$		$K_E$	
		mean	stdev	mean	stdev	mean	stdev
65 % RH	16	461	25	16.4	1.2	10.9	1.1
85 % RH	19	457	23	14.1	1.8	9.4	1.4

**Table 4.4:** Density,  $[kg/m^3]$ , embedment strength,  $[MPa]$ , and stiffness,  $[MPa/mm]$ , of oriented specimens tested at 65% RH or 85% RH.

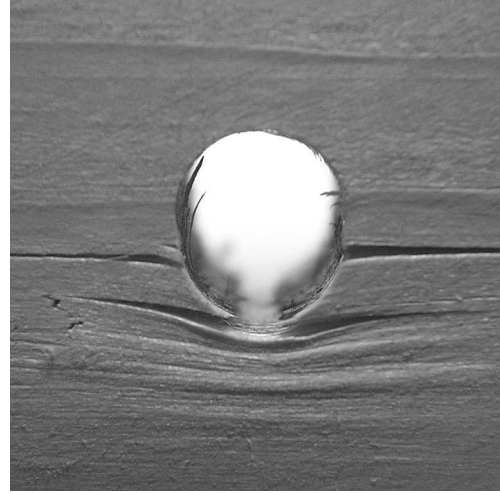
4.3 shows the analysis of variance of the influence of joint geometry.<sup>1</sup> The effect of joint geometry is obviously significant. In a Newmann-Keuls test comparing the individual means the effect of increasing the end distance is found to be not significant whereas the effect of increasing the dowel spacing is significant at a 95% level of confidence.

#### 4.2.2 Embedment and compression tests

Values for  $\rho_{12}$ ,  $f_{h,u2}$  and  $K_E$  are given in Table 4.4, the density for the moist specimens has been referred to RH 65 %. The same mean density is observed for both moist and dry specimens. The approximately 14 % strength and stiffness reduction from dry to moist condition can be referred to the increased moisture content. Figure 4.6 shows failure at the two levels of moisture content, a tendency is observed for the embedment to crush in the dry specimens ultimately whereas it is densified in the moist specimens. The embedment strength,  $f_{h,u2}$ , has been determined by use of the procedure described in Chapter 3. It should be observed that compression hardening is present and much higher values of the embedment strength is reached at larger deformations as shown in Figure 3.5.



(a) Equilibrium with RH 65%



(b) Equilibrium with RH 85%

**Figure 4.6:** *Embedment failures at  $\alpha = 90^\circ$  for oriented specimens at two different levels of moisture content.*

Direction perpendicular to grain	Density, $\rho_{12}$		Strength		Stiffness	
	Mean	Stdev	Mean	Stdev	Mean	Stdev
Radial	440	44	4.2	0.9	785	171
Tangential	439	43	5.6	1.0	533	165

**Table 4.5:** *Density,  $[\text{kg}/\text{m}^3]$ , compressive strength,  $[\text{MPa}]$ , and stiffness,  $[\text{MPa}]$ , of small oriented specimens tested in the radial and tangential direction.*

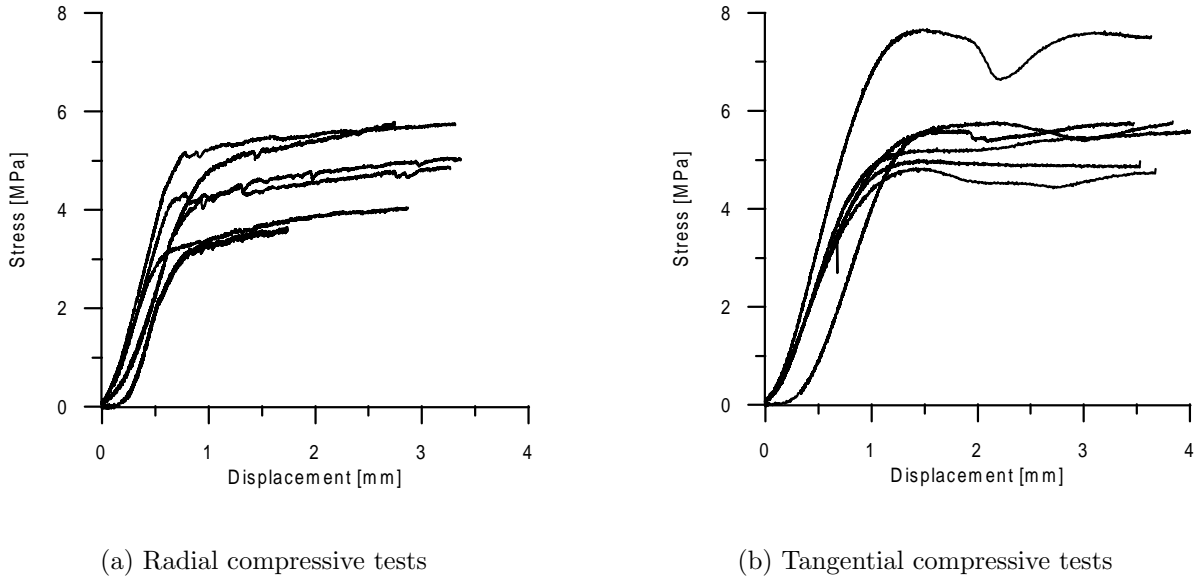


**Figure 4.7:** *Stress displacement curves for small oriented specimens (the displacement includes elastic deformation in soft intermediate plates between specimen and traverse).*

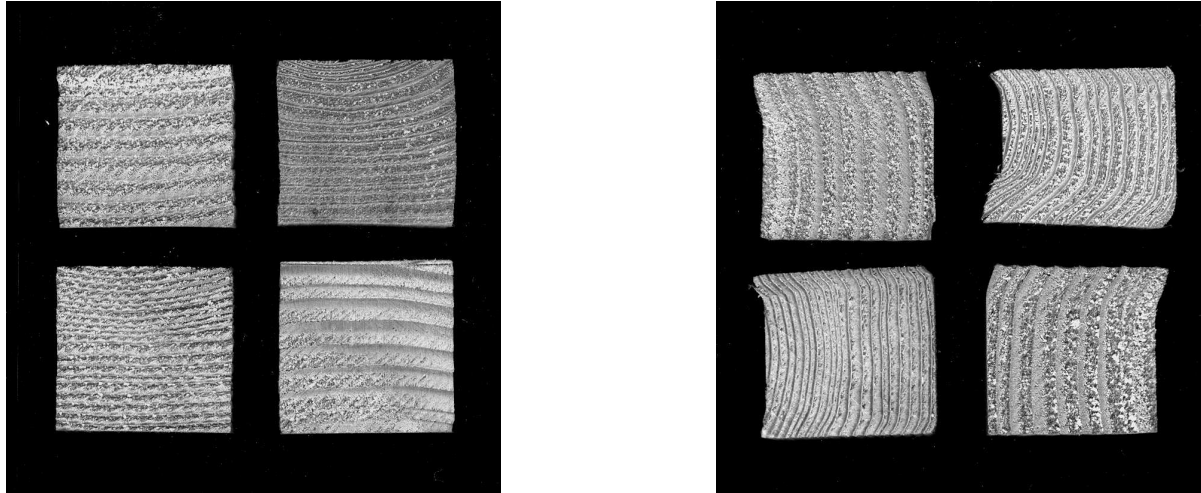
### Oriented compressive tests

The results from compression tests of small specimens in the radial and tangential directions are given in Table 4.5. The stress-displacement curves are shown in Figure 4.7. The tangential compressive strength is 33 % higher than the radial compressive strength while the radial compressive stiffness is 47 % higher than the tangential compressive stiffness. The radial tests have squeeze-like failure, Figure 4.8 (a), whereas the tests in the tangential direction, Figure 4.8 (b), exhibits buckling-like failure. These failure mechanisms are reflected in the stress displacement curves where compression squeeze hardening is seen in Figure 4.7 (a) and buckling strength loss is observable in Figure 4.7 (b).

#### 4.2.3 Transverse tension tests

In Table 4.6 the tension strengths for small oriented specimens are given. The moisture content is seen to have no effect on the brittle tension strength. The volume of the tested specimens was 70 x 45 x 45 mm and the failures were all in the central radial plane. The reason for the deterministic failure location is explained in (Pedersen, Clorius, Damkilde,

<sup>1</sup>The degrees of freedom for the error term is reduced because the block test is incomplete.



(a) Radial compressive failure

(b) Tangential compressive failure

**Figure 4.8:** *Compressive failures, squeeze-like failure in radial direction and buckling-like failure in tangential direction.*

	n	Density, $\rho_{12}$		$f_{t,90}$	
		mean	stdev	mean	stdev
65 % RH	60	454	37	2.20	0.37
85 % RH	30	454	37	2.16	0.23

**Table 4.6:** *Density, [kg/m<sup>3</sup>], tension strength perpendicular to the grain, [MPa], of oriented specimens tested at 65% RH or 85% RH.*

Hoffmeyer & Traberg 1999) and (Pedersen, Clorius, Damkilde & Hoffmeyer 2000) by use of a deterministic model utilizing the stiffness distribution in the RT-plane.

### 4.3 Predicting failure

The reported failures for the dowel connections in bending were clearly splitting failures. Ultimately, a splitting failure is anticipated in a connection utilizing the transverse strength. However, for the reported tests the splitting failure takes place at loads below or close to the yield strength determined by use of a conservative value of the embedment strength. In Table 4.7 the theoretical strengths,  $F_y(f_{h,u2})$ , according to (2.4) is determined by use of the embedment strength,  $f_{h,u2}$ , determined in Section 4.2.2. The embedment strength value used corresponds to small plastic deformations. Theoretical strength by

	$F_{ult}$	$F_y(f_{h,u2})$	$F_y(f_{h,EC5})$
65 % RH	3.70	4.13	5.62
85 % RH	3.68	3.55	-

**Table 4.7:** *Ultimate strength per shear plane, [kN], and yield strength by use of empirical embedment strength and embedment according to EC5.*

use of EC5 embedment strength determination is also given.

From Table 4.7 it is seen that the experimental ultimate capacity is lower than the anticipated plastic failure capacity. The failures are obviously due to tension stresses in the direction perpendicular to the grain. Within the codes, this problem is usually handled as a shear problem utilizing reduced cross section heights corresponding to the distance from the loaded edge to the furthest fastener or connector. However, the problem is more likely closer related to tension perpendicular to the grain stresses. The shear formulation of the problem is used because it is easy to determine a generalized shear stress within the beam theory. A generalized tension perpendicular to the grain stress cannot be generated within the beam theory.

If it is assumed that the splitting failures are governed by the shear capacity of the cross section with reduced height,  $b_e$ , the shear strength corresponding to  $F_{ult}$  is:

$$f_v = \frac{3}{2} \frac{F_{ult}}{t \cdot b_e} = \frac{3}{2} \frac{3.7}{21 \cdot 65} = 4 \text{ MPa} \quad (4.2)$$

This is an unrealistic value of the shear strength, which probably has a mean value of approximately 7 MPa. It should however be remembered that  $f_{v,TL} \leq f_{v,RL}$  and due to the orientation of the specimens the former is the relevant shear strength.

The shear approach to the splitting failures is not able to explain the strength increase with increased inter dowel spacing. In a tension perpendicular to grain formulation it is more obvious how increased spacing could have a direct effect on the strength. An indication in favour of a tension perpendicular to the grain formulation of the splitting failures is found in the moisture independence of both  $f_{t,90}$  and  $F_{ult}$ .

## 4.4 Wood structure in RT-plane

There is a difference in embedment strengths and stiffness values between the oriented specimens reported in this chapter and the specimens tested at 90° reported in Chapter 3, Table 3.4. The oriented specimens are approximately 9 % stronger than the corresponding

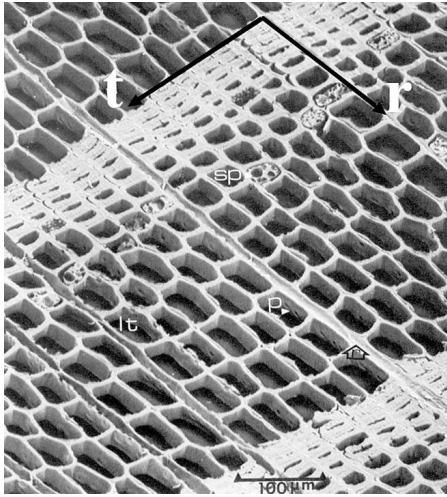
	Strength	Stiffness
Embedment	$\frac{f_{h,90T,u2}}{f_{h,90random,u2}} = 1.09$	$\frac{K_{E,90T}}{K_{E,90random}} = 0.76$
Pure compression	$\frac{f_{c,90T}}{f_{c,90R}} = 1.33$	$\frac{E_{c,90T}}{E_{c,90R}} = 0.68$

**Table 4.8:** Comparison of strength and stiffness dependency of orientation in RT-plane for both embedment and pure compressive tests.

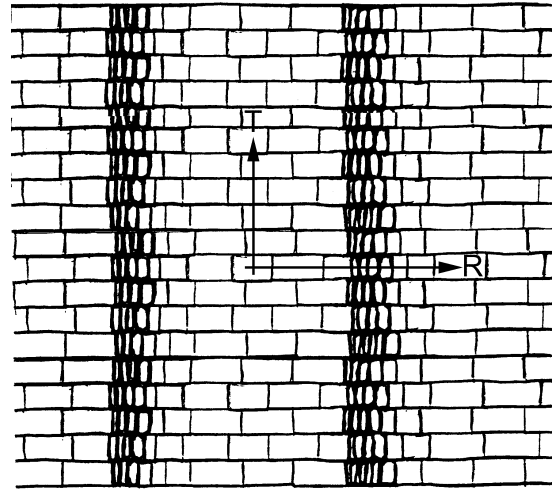
specimens with random orientation, but the oriented specimens show approximately 32 % lower stiffness.

This observation cannot be referred to density differences. However, structural differences in the RT-plane may explain the observation as the oriented specimens utilize the compressive strength in the tangential direction, and this direction represents a compressive strength maximum in the RT-plane. In Table 4.8 the difference between tangential embedment strength and embedment strength perpendicular to grain with random orientation in RT-plane is given along with a comparison of compressive properties in tangential and radial directions. The experimentally found ratio between  $E_{c,90T}$  and  $E_{c,90R}$  corresponds to the ratio given in (Dinwoodie 1981), where a ratio  $E_{c,90T}/E_{c,90R} = 0.61$  for Norway spruce (*Picea abies*) is quoted from (Hearmon 1948).

The strength and stiffness differences in the RT-plane can be explained with reference to the structure of wood. In Figure 4.9 a micrograph of the structure of softwood in the RT-plane is given along with a schematized version of the structural principle. In Table 4.9 the possible structural mechanisms governing strength and stiffness in the RT-plane are described with reference to the drawings in Figure 4.10. Inspiration for the suggested mechanisms is found in (Gibson & Ashby 1988) where simple microstructural mechanisms governing overall strength and stiffness for cellular materials are discussed. The failure mechanisms sketched in Figure 4.10 corresponds to the failure mechanisms observed as shown in Figure 4.8. With respect to the embedment properties the observation is that in the tangential direction the strength is higher than in any other direction in the RT-plane while the stiffness is lower and this can be explained by simple structural mechanisms.



(a) Scanning electron micrograph, softwood

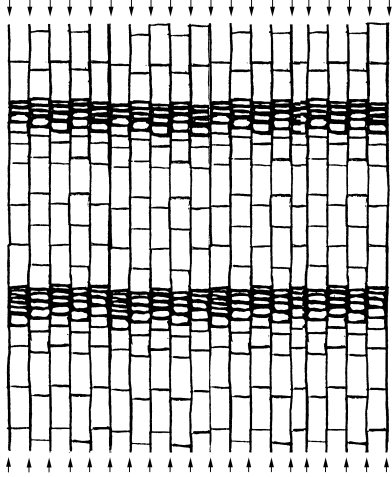


(b) Structural principle

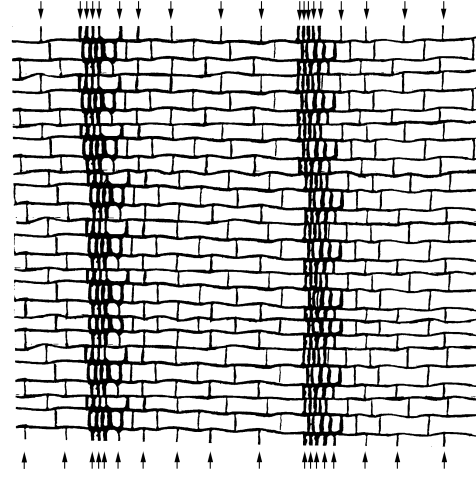
**Figure 4.9:** Cell structure in RT-plane, micrograph from (Core, Côté & Day 1976).

Comparison	Radial direction	Tangential direction
Stiffness $E_{c,90R} > E_{c,90T}$	Line oriented cell wall columns very stiff in R-direction. All material oriented in R-direction in direct column use	Load carried by latewood columns. Material in earlywood do not contribute to stiffness due to beam-function of line oriented cell walls in R-direction.
Strength $f_{c,90R} < f_{c,90T}$	Squeeze-like failure of earlywood due to buckling of line oriented cell wall in R-direction	Buckling of latewood columns. Earlywood carry little load due to low stiffness caused by beam-function of line oriented cell walls in R-direction

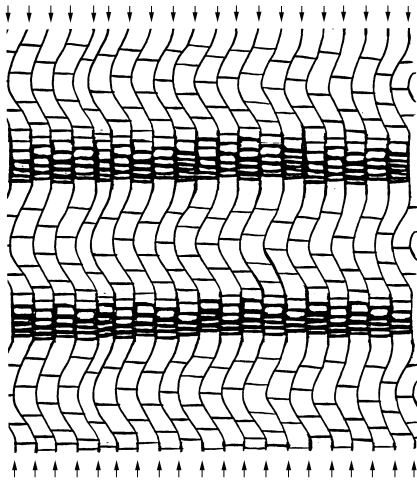
**Table 4.9:** Principal structural aspects governing strength and stiffness in radial and tangential direction.



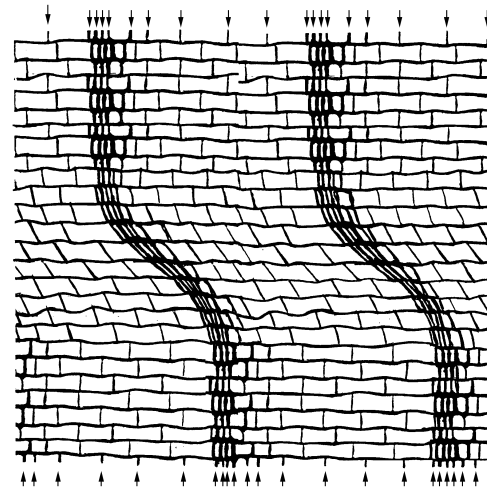
(a) Radial stiffness governed by column function of radial cell walls



(b) Tangential stiffness governed by column function of late wood



(c) Radial strength governed by radial cell wall buckling failure in early wood



(d) Tangential strength governed by late wood buckling failure

**Figure 4.10:** Schematized structural mechanisms governing stiffness and strength in radial and tangential direction.

## Chapter 5

# Full scale connections

In Chapter 4 it was shown that a brittle splitting failure may occur in advance of a ductile connector failure. Though somewhat simplified, the joint in Chapter 4 exemplifies the problem of transverse load met in real structural design. Large primary connections such as apex or foot point connections in e.g. 3-hinge arches or the connections in large glulam truss girders are designed to carry load primarily in the axial direction. For the axial loads the connections may be both strong and ductile, inevitable however these connections will also be subjected to transverse loads. This may be a direct function of the external loading, e.g. transfer of shear forces, or it may be the indirect consequence of a connection modelled as an ideal hinge which in reality transfers moment according to its relatively uncontrolled bending rigidity.

The scope of the present chapter is to trace the effect of eccentric transverse loading of full scale connections with slotted-in steel plates primarily loaded in the grain direction. The strength for different combinations of axial and transverse load is determined experimentally. A yield surface as function of angle to grain is established for the single connector by use of the results in Chapter 3. Full scale connections are modelled by use of the single connector yield surface and this plastic modelling is superimposed with brittle shear based failure criteria in Chapter 6.

## 5.1 Material and Method

### 5.1.1 Specimens

The test specimens consisted of 1.8 m long glulam beams with laminations of spruce (*Picea abies*). Each end of a specimen contained a dowel type joint designed with a slotted in steel plate and 4x4 dowels with diameter  $d = 12$  mm. Two series were tested, one series



with beam thickness of 140 mm and one with beam thickness of 90 mm. As the slots were 10 mm the corresponding wood member thicknesses was  $t = 65$  mm and  $t = 40$  mm. The variation in  $t$  corresponds to a variation in the slenderness ratio from  $\lambda = 5.4$  to  $\lambda = 3.3$ . The dowels were standard electro galvanized dowels with yield moment  $M_y=180$  Nm, this value was experimentally determined in Chapter 3. The joint geometry is shown in Figure 5.1(a). For the  $t = 40$  mm specimens the holes in the wood were tight fitting but for the  $t = 65$  mm specimens the holes were 1 mm oversized. The central steel plate was 8 mm thick and had 13 mm holes allowing the dowels to form one central hinge.

### 5.1.2 Test conditions

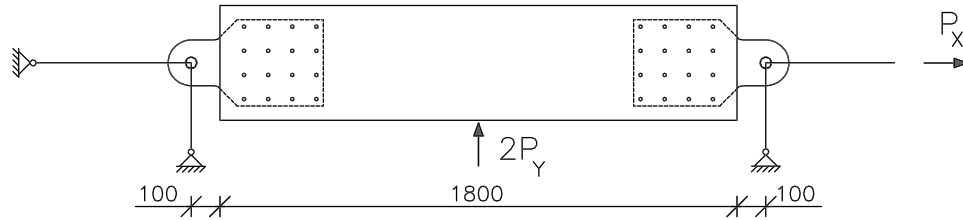


**Figure 5.2:** Overall geometry and loading condition.

The specimens were tested in a set-up as shown in Figures 5.2 and 5.1(b). A hydraulic actuator with a capacity of 500 kN was placed horizontally to provide the axial load  $P_X$ . The slotted in steel plates were tied to the strong floor with hinged steel rods and the transverse load,  $P_Y$ , was provided by an actuator placed mid span. The transverse load acted with an eccentricity of 310 mm relative to the centre of the dowel group, Figure 5.1(a). To keep track of the transverse load each rod was equipped with strain gauges. The load conditions were with reference to Figure 5.1(a):

- Pure axial loading ( $P_Y = 0$ )
- Eccentric pure transverse loading ( $P_X = 0$ )
- Combinations of transverse and axial loading

In load cases including both axial and transverse load the transverse load was applied with a fixed value of approximately 5, 10 or 15% of the axial strength and subsequently the specimens were taken to failure in a ramp of increasing axial load. The test duration

was between 5 and 15 minutes and the specimens were tested at a moisture content in equilibrium with 20°C and 65% *RH*. During tests, displacements  $w_{top}$  and  $w_{bot}$  were measured as shown in Figure 5.1(a).

## 5.2 Results

Tables 5.1 and 5.2 present test results for the two series of full scale tests. The following comments are made to the tables:

- $P_Y$  is the value of the eccentric transverse load per joint, Figure 5.1(a). For combined load  $P_Y$  is held at a constant value. For load cases comprising only eccentric transverse loading,  $P_Y$  is the ultimate strength.
- $P_{X,N}$  and  $P_{X,S}$  is the strength for the joints in each end of the specimens, i.e. the north and south end.
- In case of yielding it was often possible to determine  $P_{X,N}$  and  $P_{X,S}$  independently as in e.g. Figure 5.3. The yield strength was determined as the intersection between the elastic and plastic part of the load displacement curves, Figure 5.3.
- In case of premature splitting failures  $P_{X,i}$  is evaluated as the load corresponding to the occurrence of a crack which was both observed during testing and which was traceable on the load displacement curves, e.g. Figure 5.5. In some cases it was possible to determine independent splitting strengths for each end.
- The failures corresponding to the strength values  $P_{X,N}$  and  $P_{X,S}$  are evaluated as either plastic or splitting type.
- The ultimate strength,  $P_{X,ult}$ , is determined as the load corresponding to the highest load obtained before final splitting failure. It is observed that this value approaches  $P_{X,N}$  and  $P_{X,S}$  for high values of the transverse load.

Figures 5.3 to 5.7 show load displacement curves and failure modes for the five different load combinations in the  $t = 40$  mm series. In cases of dominating axial load, the mean value of  $w_{top}$  and  $w_{bot}$  is shown for each joint. In cases including substantial rotation, each of the four displacement measurements are shown. The photos in Figures 5.3 to 5.7 show the dowels laid out in the central section of the joints with the longitudinal axis perpendicular to the direction in which the dowel was embedded at failure. It is seen

$\rho_{12}$ [kg/m <sup>3</sup> ]	$P_Y$ [kN]	$P_{X,N}$ [kN]	$P_{X,S}$ [kN]	Mean [kN]	Stdev. [kN]	Failure type	$P_{X,ult}$ [kN]	Mean [kN]
460	-	313	312			Plastic	340	
464	-	320	325			Plastic	367	
473	-	342	334			Plastic	389	
465	-	310	302	320	13	Plastic	346	361
473	17	314	314			Plastic	347	
465	17	332	330			Plast/split	360	
472	17	323	323			Split/plast	323	
465	17	318	328	323	7	Plastic	372	351
448	33	268	264			Split/plast	302	
459	33	261	261			Splitting	261	
465	33	252	322			Splitting	322	
472	33	270	270	271	21	Splitting	270	289
473	50	204	204			Splitting	204	
465	50	207	220			Splitting	220	
461	50	234	261			Splitting	261	
467	50	151	151	204	38	Splitting	151	209
467	71	-	-			Splitting	-	
482	79	-	-			Splitting	-	
473	67	-	-			Splitting	-	
467	82	-	-	75	7	Splitting	-	

**Table 5.1:** *Strength and density for full scale specimens with  $t = 40\text{mm}$ .*

$\rho_{12}$ [kg/m <sup>3</sup> ]	P <sub>Y</sub> [kN]	P <sub>X,N</sub> [kN]	P <sub>X,S</sub> [kN]	Mean [kN]	Stdev. [kN]	Failure type	P <sub>X,ult</sub> [kN]	Mean [kN]
490	-	283	339			Plastic	393	
442	-	348	338			Plastic	395	
473	-	304	294			Plastic	377	
449	-	316	314	317	23	Plastic	370	384
468	38	300	300			Splitting	331	
471	39	250	253			Split/plast	311	
476	40	309	316			Plastic	339	
459	40	298	305			Plastic	363	
441	40	271	250			Plast/split	271	
471	40	338	353			Plastic	372	
442	44	305	230			Plast/split	305	
464	40	298	298	292	33	Splitting	298	324
505	60	146	146			Splitting	146	
459	60	169	183			Splitting	183	
469	60	204	227			Splitting	227	
474	60	197	189	183	28	Splitting	197	188
478	72	-	-			Splitting	-	
437	80	-	-			Splitting	-	
459	85	-	-			Splitting	-	
502	89	-	-	81	7	Splitting	-	

**Table 5.2:** *Strength and density for full scale specimens with  $t = 65\text{mm}$ .*

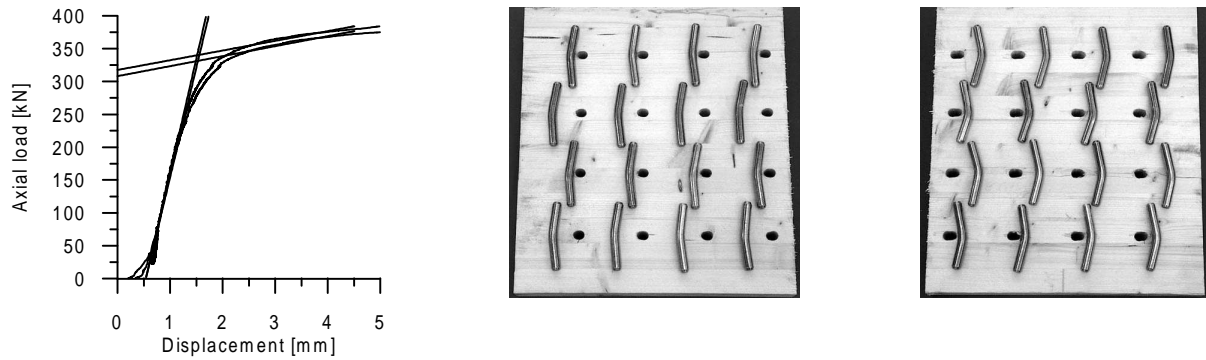


**Figure 5.3:** *Axial testing,  $t = 40\text{mm}$ .*

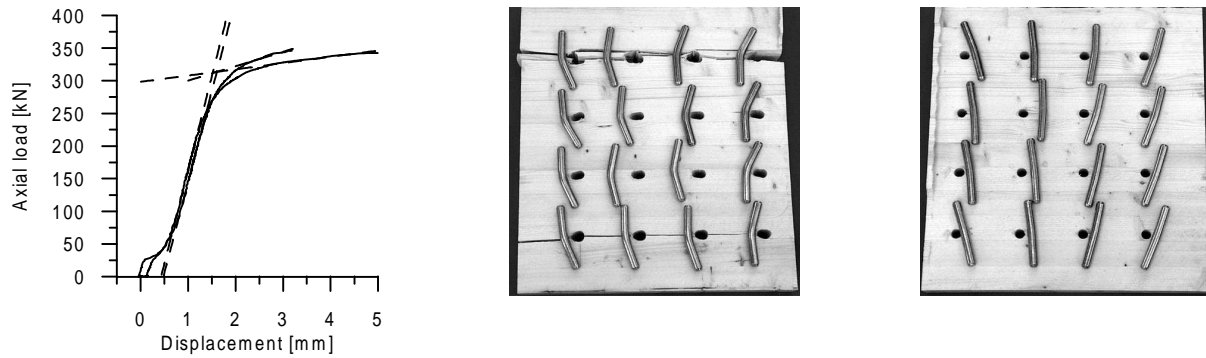


**Figure 5.4:** *Axial testing combined with approx. 5% transverse load,  $t = 40\text{mm}$ .*

that in the pure axial load case, Figure 5.3, all dowels bend plastically, else the pattern is that for increased transverse load the dowels act increasingly rigid and in case of pure transverse load, Figure 5.7, none of the dowels exhibit plastic bending. The results from Tables 5.1 and 5.2 are resumed in Figures 5.8 and 5.9 where the failures are given in diagrams of axial and transverse load. A brittle capacity in excess of the yield strength is observed for low values of the transverse load. The mode shift from plastic failures to splitting failures for increased transverse load is shown by means of different data point marks for the two failure types.

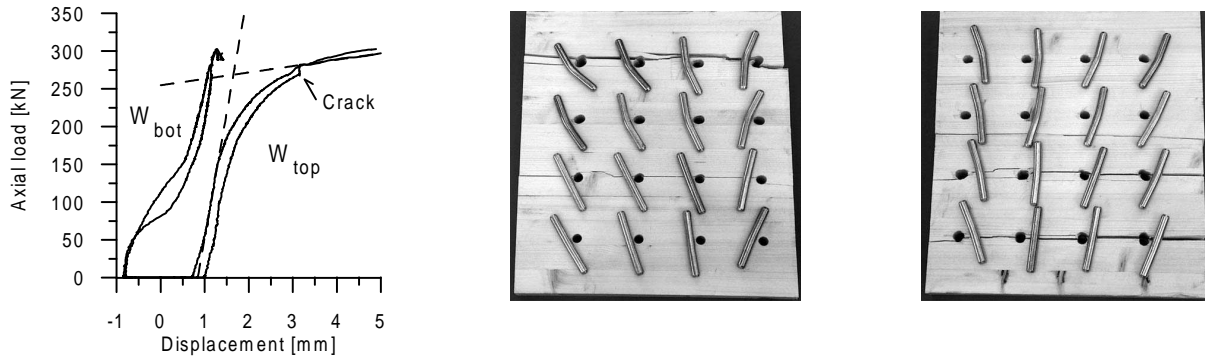


Figure 5.5: Axial testing combined with approx. 10% transverse load,  $t = 40\text{mm}$ .

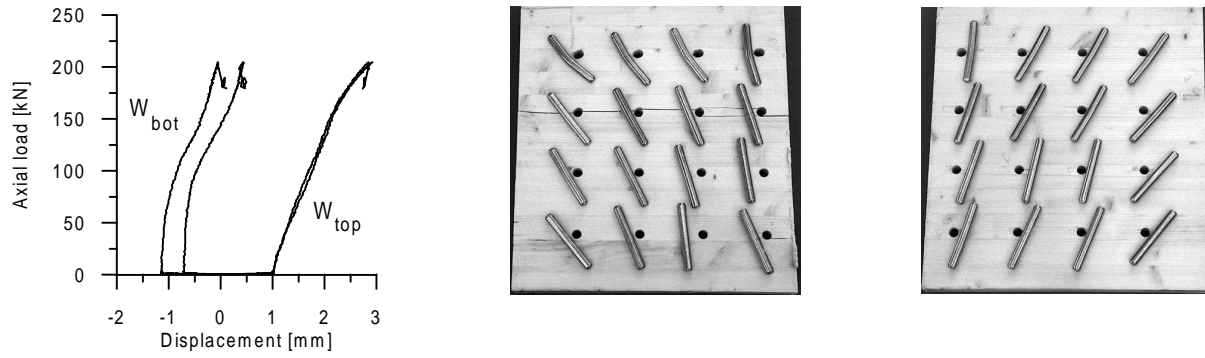


Figure 5.6: Axial testing combined with approx. 15% transverse load,  $t = 40\text{mm}$ .

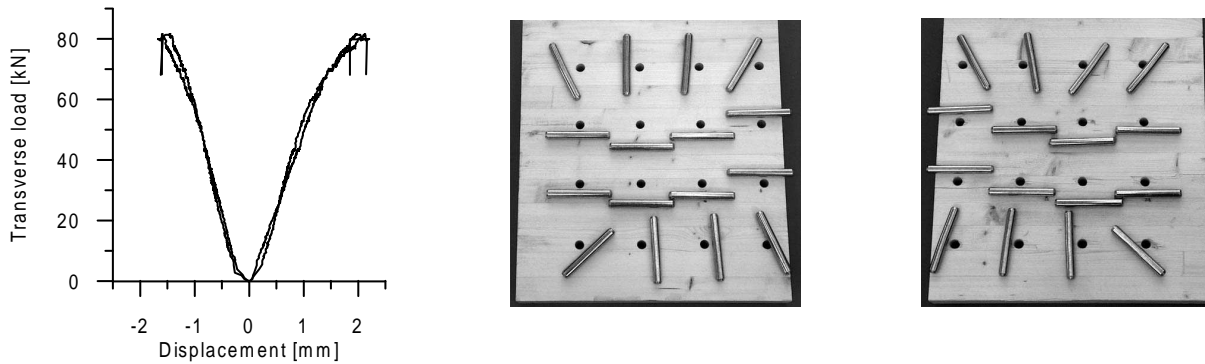


Figure 5.7: Eccentric pure transverse testing,  $t = 40\text{mm}$ .

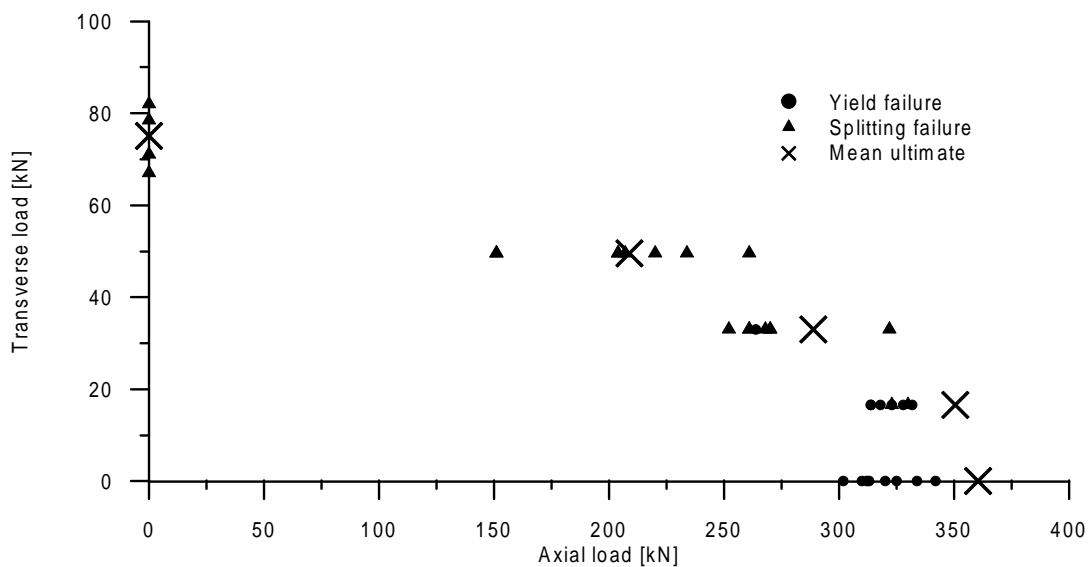


Figure 5.8: Experimental failure surface for full scale joint,  $t=40\text{mm}$ .

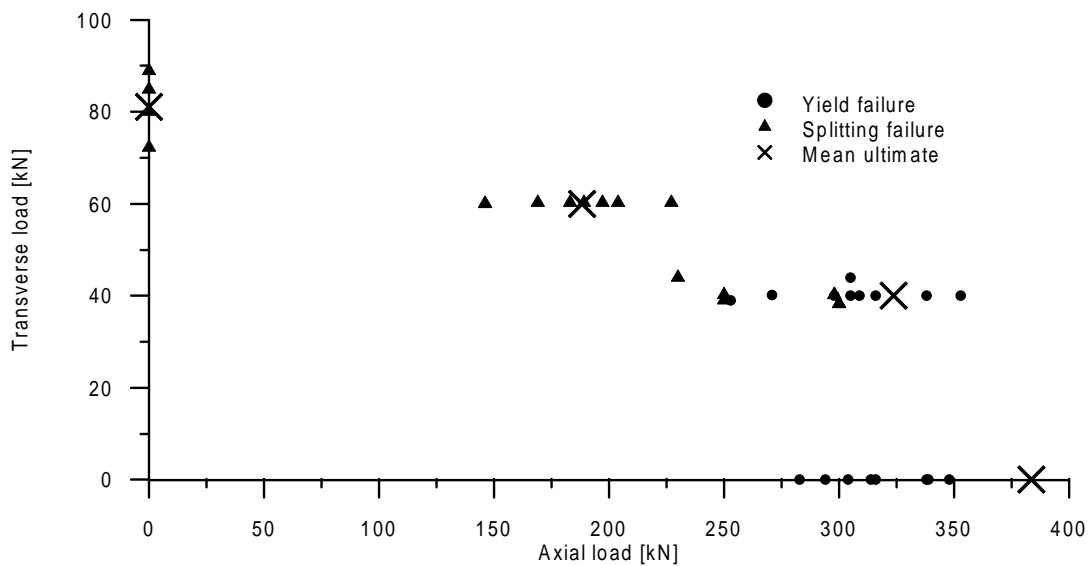


Figure 5.9: Experimental failure surface for full scale joint,  $t=65\text{mm}$ .



## Chapter 6

# Discussion on full scale connections

In Chapter 5 it was shown that the full scale connections failed in regular yield failures for dominating axial load whereas the failures become increasingly dominated by splitting for increased transverse load. This chapter aims primarily at assessing to what extent a yield modelling of the joint overestimates the strength when this is determined by splitting and to assess whether the splitting failures can be explained by exceeded shear capacity.

## 6.1 Modelling full scale connections

### 6.1.1 Single connector description

In order to establish a yield model for the single connector one of the mechanical models for double shear connections with a central steel plate given in Chapter 2 has to be chosen. Both the  $t = 40$  mm series and the  $t = 65$  mm series were characterised by a slot eccentricity and further the  $t = 65$  mm series had oversized holes. Hence, the model including slot eccentricity (2.5) is adequate for the  $t = 40$  mm test series and the model (2.6) is adequate for the  $t = 65$  mm test series. The model adequacy is seen from Table 6.1 where the experimental mean connector strength per shear plane is given along with strengths determined on basis of the models (2.4), (2.5) and (2.6) and the material parameters,  $f_h$  and  $M_y$ , determined in Chapter 3.

	$\bar{F}_{y, experimental}$	$F_{y, eq (2.4)}$	$F_{y, eq (2.5)}$	$F_{y, eq (2.6)}$
$t = 40$	10.0	11.9	10.4	-
$t = 65$	9.9	13.9	12.6	9.9

**Table 6.1:** Comparison of experimental and theoretical values of strength per shear plane for loading in the grain direction [kN].

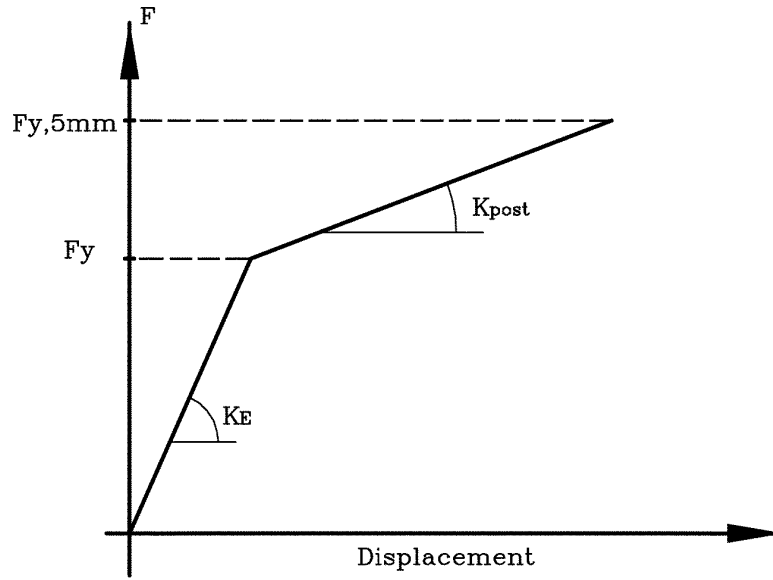


**Figure 6.1:** Schematized force displacement curve for the single connector.

For a given angle to grain the force displacement curve for the single connector is characterized by the following material parameters:

- The elastic stiffness  $K_E$
- The transition yield strength  $F_y$  corresponding to the embedment strength  $f_h$ .
- The post elastic stiffness  $K_{post}$
- The yield strength  $F_{y,5mm}$  corresponding to embedment strength at 5 mm plastic deformation  $f_{h,y5}$ .

The characterizing parameters are schematized in Figure 6.1. In Figure 6.2  $F_y$  and  $F_{y,5mm}$  have been determined as function of angle to grain by use of the relevant failure models and the embedment strength at four angles as given in Table 3.4. The fits are purely empirical. The embedment stiffness can not directly be used to model the connector stiffness due to the effects of bending in dowel and unequal stress distribution along the dowel. The connector stiffness as function of angle to grain has been determined using stiffness determined empirically in connector tests, results are given in Table 6.2. The empirical connector stiffness determined at  $0^\circ$  and  $90^\circ$  has been interpolated linearly. The post elastic stiffness  $K_{post}$  is determined as the slope between  $F_y$  and  $F_{y,5mm}$ .

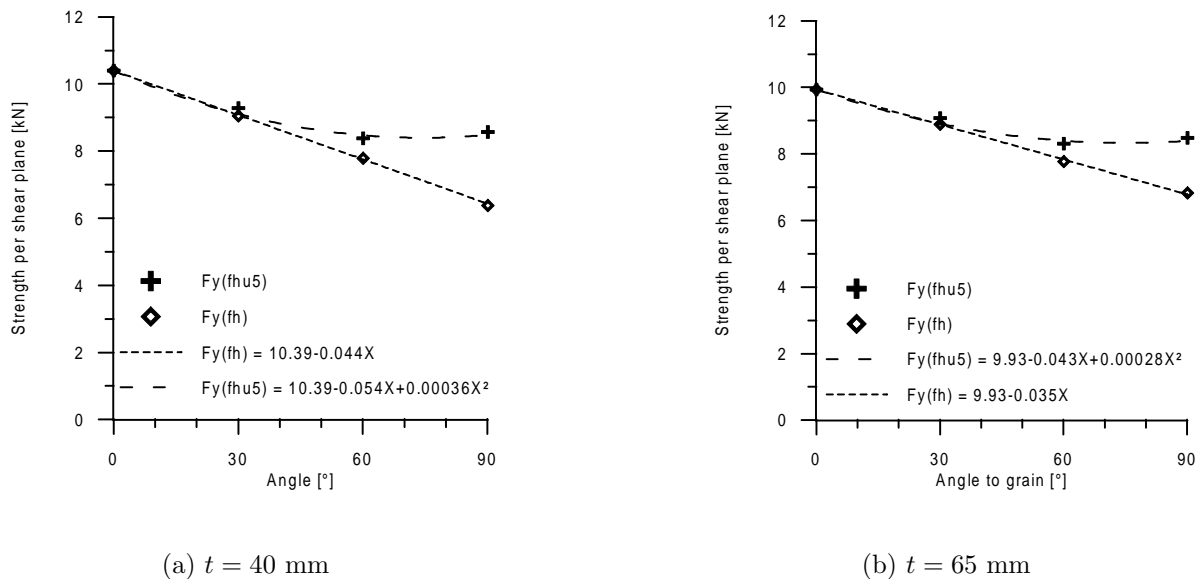


**Figure 6.2:** Yield capacity per shear plane as function of angle to grain.

	$K_{0,t=40}$ [kN/mm]	$K_{90,t=40}$ [kN/mm]	$K_{0,t=65}$ [kN/mm]	$K_{90,t=65}$ [kN/mm]
Mean	10.5	5.9	8.6	5.7
Stdev	0.8	0.8	1.2	1.6

**Table 6.2:** Connector stiffness.

**Model parameters for  $t=40$  mm**

For the  $t = 40$  mm series the dowel properties per shear plane as function of angle to grain is expressed by the following fits:

$$F_y(\alpha) = 10.4 - 0.044\alpha \quad [\text{kN}] \quad (6.1)$$

$$F_{y,5mm}(\alpha) = 10.4 - 0.054\alpha + 0.00036\alpha^2 \quad [\text{kN}] \quad (6.2)$$

$$K_E(\alpha) = 10.5 - 0.051\alpha \quad [\text{kN/mm}] \quad (6.3)$$

$$K_{post}(\alpha) = -0.0020\alpha + 0.72 \cdot 10^4 \alpha^2 \quad [\text{kN/mm}] \quad (6.4)$$

**Model parameters for  $t=65$  mm**

For the  $t = 65$  mm series the dowel properties per shear plane as function of angle to grain is expressed by the following fits:

$$F_y(\alpha) = 9.9 - 0.035\alpha \quad [\text{kN}] \quad (6.5)$$

$$F_{y,5mm}(\alpha) = 9.9 - 0.043\alpha + 0.00028\alpha^2 \quad [\text{kN}] \quad (6.6)$$

$$K_E(\alpha) = 8.6 - 0.032\alpha \quad [\text{kN/mm}] \quad (6.7)$$

$$K_{post}(\alpha) = -0.0016\alpha + 0.56 \cdot 10^4 \alpha^2 \quad [\text{kN/mm}] \quad (6.8)$$

**6.1.2 Yield modelling of full connection**

Yield modelling of the full connection has been made with an ideal plastic assumption, i.e. the deformation hardening observed for increased angle to grain is neglected. The yield capacity for the single connector is determined as function of angle to grain by use of the empirically determined embedment yield surface given in Figure 3.8 and the dowel bending capacity  $M_y = 180$  Nm determined in Chapter 3.

In Figures 6.3 and 6.4 the yield surface is given for the  $t=40$  mm and the  $t=65$  mm tests respectively under the assumption that the load bearing capacity is determined by (2.4), i.e. the original yield model not taking into account effects of eccentricity and oversized holes. The yield surfaces are given for both first yield and for full plastic behaviour. First yield corresponds to the load where yielding is initiated in one of the connectors, i.e. the limit of the elastic capacity. Full plastic behaviour corresponds to the load where all connectors are in yielding. The modelling in Figures 6.3 and 6.4 overestimates the strength for pure axial loading by approximately 20% in the case of the  $t=40$  mm tests and by approximately 40% in the case of the  $t=65$  mm tests. In Figures 6.5 and 6.6 the model refinements discussed in Chapter 2 are included. For the  $t = 40$  mm tests slot

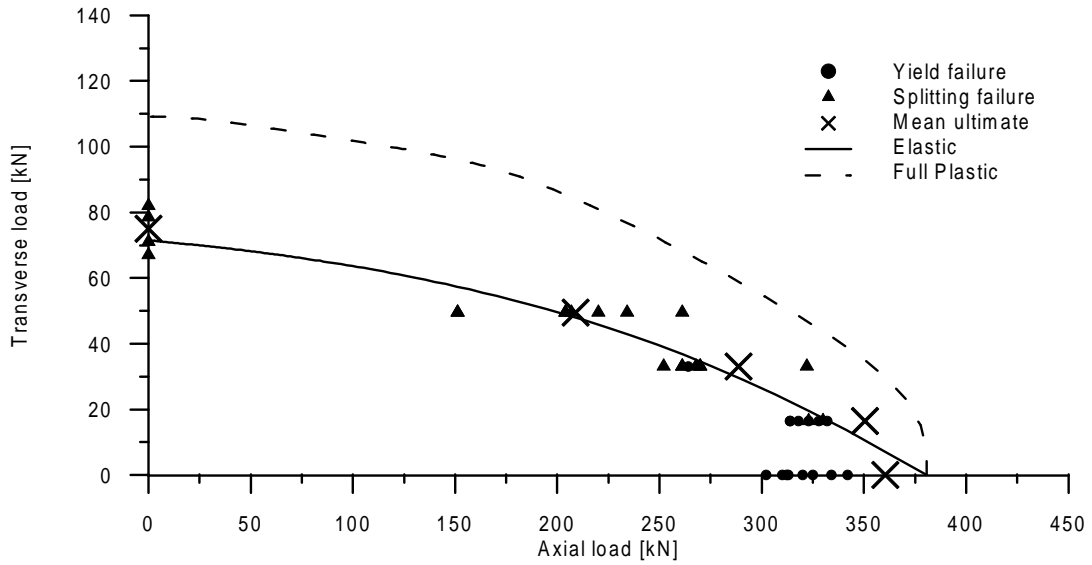


**Figure 6.3:** Yield surface according to (2.4) for full scale joint,  $t=40\text{mm}$ , plotted with experimental results. Axial load =  $P_X$ . Transverse load =  $P_Y$ .

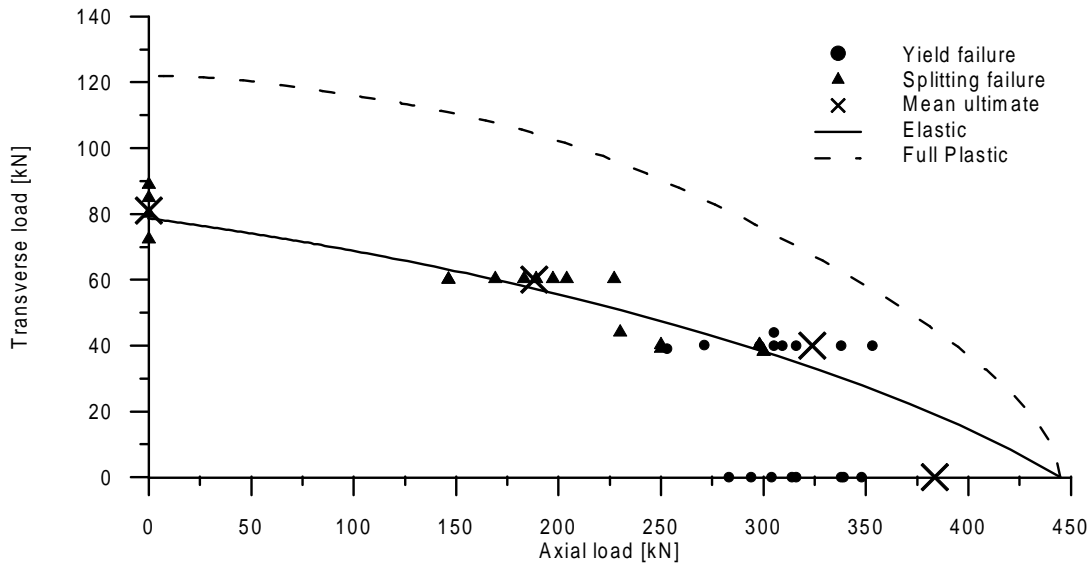


**Figure 6.4:** Yield surface according to (2.4) for full scale joint,  $t=65\text{mm}$ , plotted with experimental results. Axial load =  $P_X$ . Transverse load =  $P_Y$ .

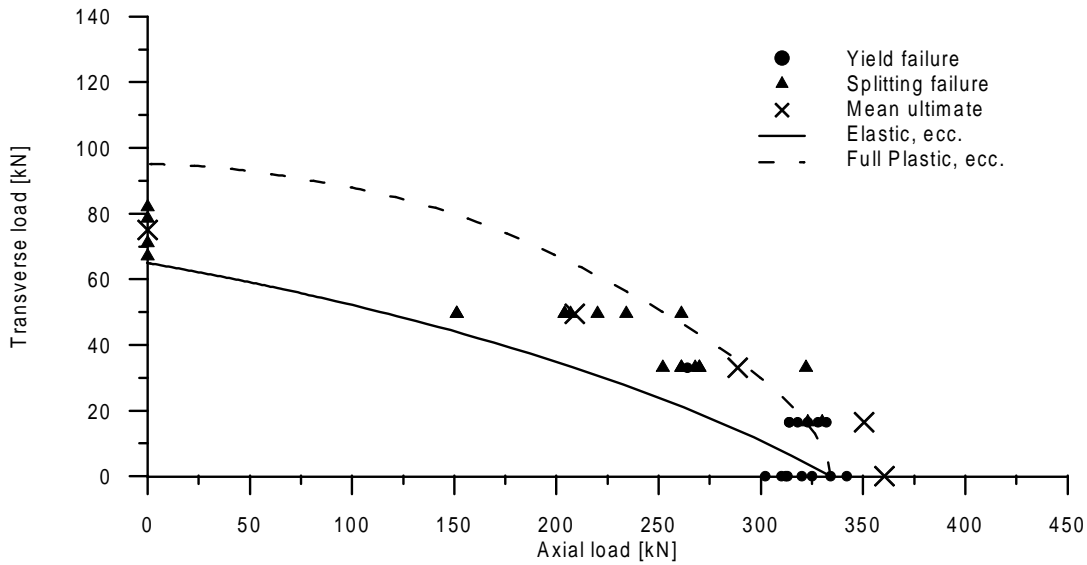


**Figure 6.5:** Yield surface according to (2.5) for full scale joint,  $t=40\text{mm}$ , plotted with experimental results. Axial load =  $P_X$ . Transverse load =  $P_Y$ .

eccentricity is included in the modelling corresponding to yield model (2.5) and for the  $t = 65$  mm tests both eccentricity and oversized dowel holes are included in the modelling corresponding to yield model (2.6). For these improved models the yield capacity for pure axial loading is well predicted as shown in Table 6.1. For other load combinations the ultimate elastic capacity is always predicted below the observed failure loads. The full plastic capacity is only reached in the connections for small values of the transverse load, for failures dominated by the transverse load the full plastic modelling overestimates the strength. For pure transverse loading the overestimation is approximately 30% for the  $t=40$  mm tests and approximately 20% for the  $t=65$  mm tests.

For the tested joint geometry an elastic load bearing determination is a safe design criteria. However, for small values of the transverse load where it is too conservative a full plastic determination of the capacity can be used.

## 6.2 Brittle modelling of full scale connections

### 6.2.1 Shear based failure modelling

For high values of the transverse load the failures were of the splitting type. That is splitting of the cross section was observed before reaching the full plastic capacity determined on basis of the plastic capacity of the individual connectors. These failures may be the

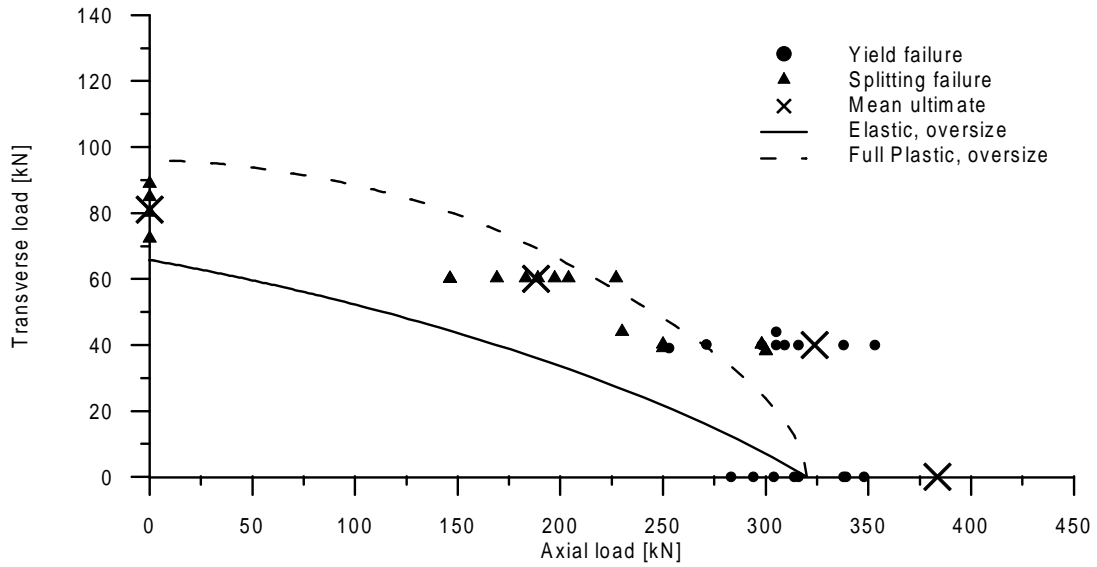


**Figure 6.6:** Yield surface according to (2.6) for full scale joint,  $t=65\text{mm}$ , plotted with experimental results. Axial load =  $P_X$ . Transverse load =  $P_Y$ .

consequence of the shear capacity of the cross section being exceeded.

According to (EC5-1 1995) the shear capacity of the joints should be determined as:

$$V_{max} \leq \frac{2f_v \cdot b_e \cdot 2t}{3}, \quad (6.9)$$

where  $b_e$  is the distance from the loaded edge to the furthest connector, i.e.  $b_e = 400 - 74$  according to Figure 5.1 (a). A mean value of the shear strength is according to (Larsen & Riberholt 1988) approximately 7 MPa, but the value 5.7 MPa is used based on shear tests on 9 specimens. Hence, the shear capacity can be estimated to:

$$V_{max} = \begin{cases} 99 \text{ kN} & \text{for } t = 40\text{mm} \\ 161 \text{ kN} & \text{for } t = 65\text{mm} \end{cases} \quad (6.10)$$

Determined in this way the capacity for the  $t = 40$  mm specimens is overestimated by 30 % and for the  $t = 65$  mm specimens by 100 %. This determination of the shear capacity substitutes a complex problem of tension perpendicular to the grain stresses by a shear design over a reduced cross section. A more elaborate model based on fracture mechanics is proposed by Van der Put (1990). This model takes the influence of the beam depth  $h$  into account. For  $M/(V \cdot h) \leq 2.1$  the shear capacity is determined as:

$$V_{max} \leq \frac{2f_v \cdot b_e \cdot 2t}{3} \sqrt{\frac{130}{h} \frac{2.1}{M/(V \cdot h)}}, \quad (6.11)$$

where  $M$  is the maximum bending moment nearest to the joint,  $M/(V \cdot h) = 1.09$ . For the two beam thicknesses the shear capacity is estimated to:

$$V_{max} = \begin{cases} 78 \text{ kN} & \text{for } t = 40\text{mm} \\ 127 \text{ kN} & \text{for } t = 65\text{mm} \end{cases} \quad (6.12)$$

A shear based failure criteria as (6.9) or (6.11) could be used to predict the ultimate brittle strength of 75 kN for pure transverse loading for the  $t = 40$  mm specimens. The models are however not able to explain why the brittle strength of the  $t = 65$  mm specimens only increases marginally (8 %) when the thickness is increased 60 %. Further there is an interaction between the axial load and the transverse load in a way that does not make it possible to determine the shear capacity independent of the axial load.

In Figures 6.7 and 6.8 the mean ultimate brittle strengths are shown along with simple proposals for interactions between axial and transverse load. The first proposal (6.13) states that the degree of utilization of the brittle capacity is linear in both the ultimate brittle strength in the axial direction  $P_{X,ult}$  and the ultimate brittle strength for pure transverse load  $P_{Y,ult}$ , the second proposal (6.14) is quadratic in the transverse term:

$$\frac{P_X}{P_{X,ult}} + \frac{P_Y}{P_{Y,ult}} \leq 1 \quad (6.13)$$

$$\frac{P_X}{P_{X,ult}} + \left(\frac{P_Y}{P_{Y,ult}}\right)^2 \leq 1 \quad (6.14)$$

The implication of the linear proposal (6.13) is that full utilization of the capacity in tension perpendicular to the grain is the sum of the degree of direct utilization by transverse load and the degree of utilization by the tension perpendicular to grain stresses due to axial load. Tension perpendicular to grain stresses arising due to axial load is reported in e.g. (Jorissen 1998). The linear criterion is however too conservative. The semi quadratic proposal, which fits the data well, is the result of curve fitting. The implication of the semi quadratic proposal is from a design point of view comforting as a connection primarily designed to take axial loads can take small values of transverse load without major reduction of the brittle strength.

### 6.2.2 Slenderness ratio

The most disconcerting observation made when comparing the tests at  $t = 40$  mm with the tests at  $t = 65$  mm is that only an insignificant increase in the brittle strength is obtained for 60 % increase in wood member thickness. The slenderness ratio,  $\lambda = t/d$ , is

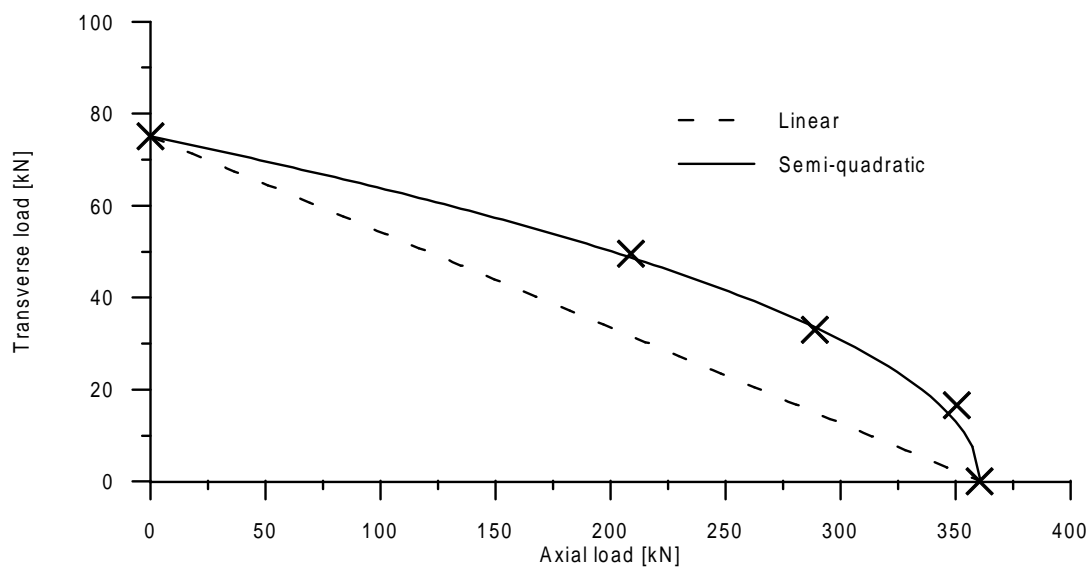


**Figure 6.7:** *Splitting capacity for  $t=40$  mm. Axial load =  $P_X$ . Transverse load =  $P_Y$ .*

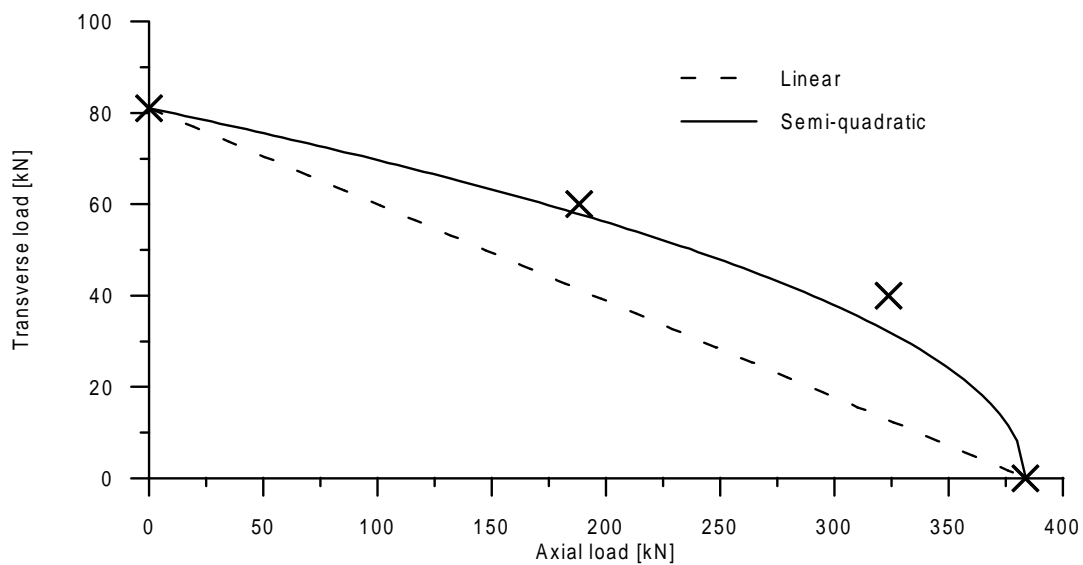


**Figure 6.8:** *Splitting capacity for  $t=65$  mm. Axial load =  $P_X$ . Transverse load =  $P_Y$ .*

increased from 3.3 to 5.4 and the relative slenderness ratio,  $\lambda_r$ , from 0.46 to 0.74 parallel to grain and from 0.29 to 0.48 perpendicular to grain. The relative slenderness ratio is defined as the slenderness ratio relative to the slenderness ratio corresponding to mode III failure:

$$\lambda_r = \frac{\lambda}{\lambda_y} = \frac{t/d}{\sqrt{\frac{16 M_y}{d^3 f_h}}} \quad (6.15)$$

Though the slenderness ratio is more favourable for the wide specimens no corresponding increase in ultimate strength is observed. This may lead to the conclusion that the mean overall utilization of the cross section is not the only parameter governing splitting failure.

In the Danish code low relative slenderness ratios due to dowels with high strength steel are treated by prescribing spacing increased by  $\sqrt{f_y/240}$  for steel with yield strength in excess of 240 MPa. The necessity of this is not verified by the reported experiments. The tests with dominating axial load show that splitting-cracking failure does not precede plastic connector failure when dowels with  $f_y = 640$  MPa are used without increasing dowel spacing.

## Chapter 7

# Fibre reinforced plastic in dowel type connections

### 7.1 Background

The use of fibre reinforced plastic, FRP, as substitute for steel in traditional dowel type timber connections with steel dowels and slotted in steel plates is an idea conceived in the United Kingdom. The substitution of steel plates and dowels in timber connections with FRP has been worked on primarily by an English group of researchers, (Drake, Ansell, Aram, Mettem & Bainbridge 1996), (Drake, Ansell, Aram, Mettem & Bainbridge 1998*a*), (Drake, Aram & Ansell 1998*b*), (Drake, Ansell, Aram, Mettem & Bainbridge 1999), and (Drake & Ansell 2000). The anticipated advantages of replacing steel with FRP in slotted-in dowel type connections are as follows:

- Production ease
  - The slotted-in plates are easily cut to size and do not need to be pre-manufactured in a steel workshop
  - It is possible to drill directly through wood and inserted FRP-plate, hereby facilitating the production process
- Production accuracy
  - Drilling through plate and wood in one process enhances the accuracy and hereby the reduction in load bearing capacity for multiple dowels in row may be minimized
- Non-corrosiveness

- The use of FRP as substitute for steel will eliminate any problems with corrosion in aggressive environments (stables, swimming baths, etc.)
- Fire resistance
  - With a lower heat conductivity, FRP-dowels may be as wide as the timber and still have an active part in the fire case

## 7.2 Material and tests

In order to evaluate the feasibility of replacing steel with FRP materials in slotted-in timber connections tests were made to examine:

- Dowel properties
  - Bending strength in 3-point bending tests
  - Shear capacity in guillotine tests
- FRP plate embedment properties
  - Embedment tests in pultrusion direction
  - Embedment tests perpendicular to pultrusion direction
- Connector tests
  - Tests of single FRP-wood connection with different wood member thicknesses
  - Tests of single FRP-dowels in open holes
- FRP plate buckling properties
  - Plate bending tests to obtain plate  $EI$
  - Buckling tests for free pinned plates
  - Buckling tests for pinned plates in slots

The dowel material was cut from two samples of pultruded FRP rods with diameter 12 and 16 mm. The fibres were E-glas G017X in a matrix of isoftalacidpolyester P2600. The 8 mm FRP plates were cut from the web of pultruded FRP U-profile 48x160/8/8. The profile fibres were E-glas G567P in a matrix of isoftalacidpolyester P4506. The wood used was glued laminated timber (*Picea abies*), strength class L30-L40, with mean density 467 kg/m<sup>3</sup> conditioned to equilibrium with 65% RH at 20° C. The wood was taken from the remains of the beams reported in Chapter 5.

Span [mm]	n	$P_{max}$ [kN]		$M_{max}$ [kNmm]		Stiffness [kN/mm]	
		mean	stdev.	mean	stdev.	mean	stdev.
300	2	1.54	0.26	116	19.5	0.056	0.01
150	6	2.82	0.33	106	12.5	0.42	0.03
100	6	4.43	0.20	111	5.0	1.13	0.03
50	6	6.33	0.32	79.1	4.0	3.4	0.1
25	5	9.50	0.28	59.4	1.8	9.0	0.3
12.5	6	22.04	1.45	68.9	4.5	11.3	0.9
$\simeq 0$	16	30.22	1.5	$\simeq 0$	$\simeq 0$	30.22	1.5

**Table 7.1:** Critical combinations of system force  $P_{max}$  and moment  $M_{max}$  and initial system stiffness determined in three point bending of 12 mm FRP dowels at different spans,  $n$ =number of tests.

Span [mm]	n	$P_{max}$ [kN]		$M_{max}$ [kNmm]		Stiffness [kN/mm]	
		mean	stdev.	mean	stdev.	mean	stdev.
400	6	2.59	0.13	259	13.0	0.084	0.002
200	6	5.06	0.19	253	9.5	0.67	0.02
100	6	8.43	0.21	211	5.3	3.29	0.10
50	6	11.8	0.51	142	9.6	11.2	0.6
25	6	26.5	1.42	159	8.5	25.0	1.18

**Table 7.2:** Critical combinations of system force  $P_{max}$  and moment  $M_{max}$  and initial system stiffness determined in three point bending of 16 mm FRP dowels at different spans,  $n$ =number of tests.

### 7.3 Dowel properties

The strength and stiffness of 12 and 16 mm diameter FRP-dowels have been determined in three-point bending tests with spans ranging from 400 mm to  $\simeq 0$ , the latter in guillotine tests. The guillotine tests were made on 12 mm dowels only. All dowel tests were deformation controlled with a target duration of 3 minutes to failure. The 3-point bending tests were made in an ordinary bending rig. In the guillotine test the dowel passed through a 13 mm hole going through three steel plates, the outer of 20 mm thickness and the inner 8 mm. The guillotine tests were inspired by tests described in (Drake et al. 1999).

The test results are given in Tables 7.1 and 7.2 and cover strength of the dowels

	Parallel	n=6	Perpendicular	n=6
	$f_{h,0}$ [MPa]	$K_0$ [kN/mm]	$f_{h,90}$ [MPa]	$K_{90}$ [kN/mm]
mean	285	37.0	138	22.2
stdev.	44	3.7	14	1.3

**Table 7.3:** *Embedment properties.*

in different combinations of shear and bending moment. Load-displacement curves are given in Figure 7.1 along with photos of failure morphology. The increase in ductility for decreased span corresponds to failures increasingly dominated by shear. The failures obtained in the guillotine tests on 12 mm dowels are cross-fibre-tearing failure as shown in Figure 7.2. Neither strength, stiffness nor failure morphology for these tests are in line with the values and failure modes for the other dowel tests.

## 7.4 FRP-embedment

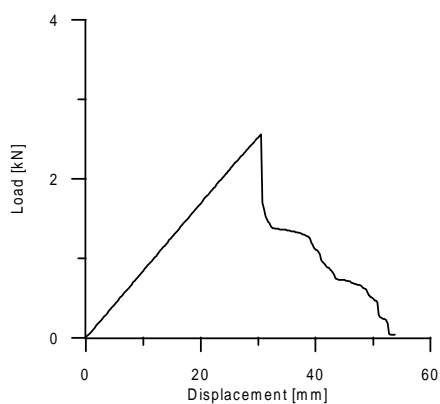
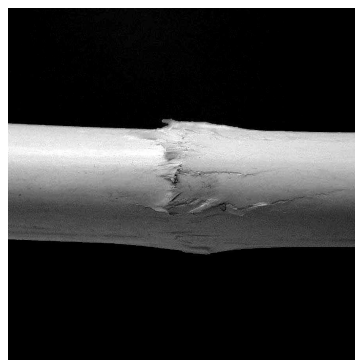
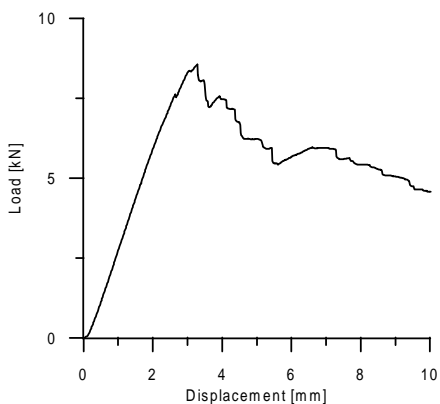
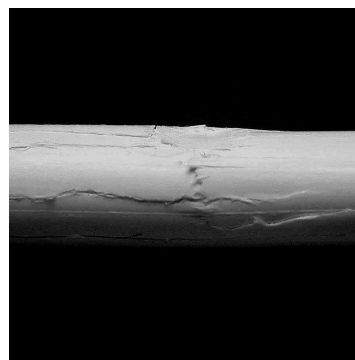
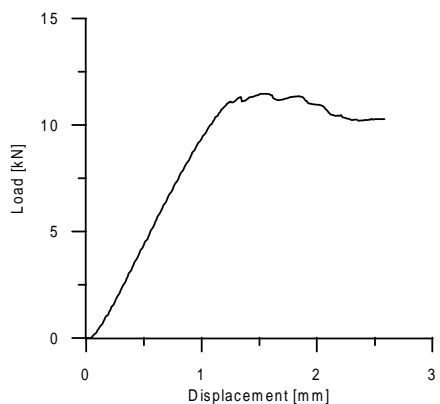
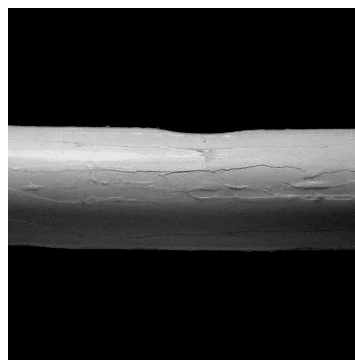
The embedment properties of the FRP-plates have been determined both parallel and perpendicular to the pultrusion direction, Figure 7.3. The specimens were  $8 \times 100 \times 100$  mm with a central 13 mm hole. A 12 mm steel dowel rested on the embedment. Embedment strength and initial stiffness are determined and given in Table 7.3. The embedment strength is determined as:

$$f_h = \frac{F_{ult}}{d \cdot t} \quad (7.1)$$

The stiffness is determined on basis of the displacement of the traverse, but relates primarily to local compression in the FRP-plate beneath the dowel.

## 7.5 Connector tests

Tests on single 12 and 16 mm FRP connectors in wood with slotted-in 8 mm FRP plates have been performed with different wood member thicknesses,  $t$ . Precision 8 mm slots were cut in the wood, FRP plates inserted and 12 or 16 mm holes drilled through wood and FRP in one operation. Load were applied in compression in the fibre direction of wood and in the pultrusion direction of the FRP plate. The geometry of the test specimens is seen in Figure 7.4. Tests were deformation controlled with target duration of approximately 5 minutes to final failure. Figure 7.5 shows load deformation for tests with different  $t$ .

(a) Brittle behaviour,  $l=400\text{mm}$ (b) Bending failure,  $l=400\text{mm}$ (c) Semi brittle behaviour,  $l=100\text{mm}$ (d) Bending/shear failure,  $l=100\text{mm}$ (e) Ductile behaviour,  $l=50\text{mm}$ (f) Shear failure,  $l=50\text{mm}$ 

**Figure 7.1:** Load mid deflection and failure morphology of bending tests on 16 mm dowels at different spans.

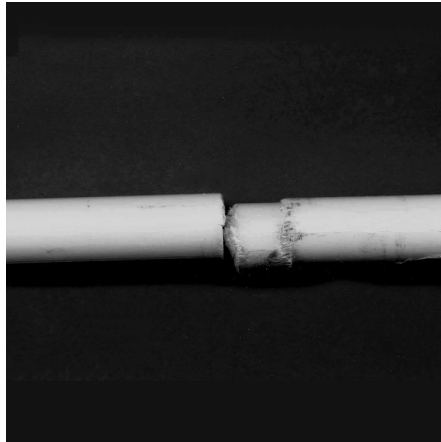


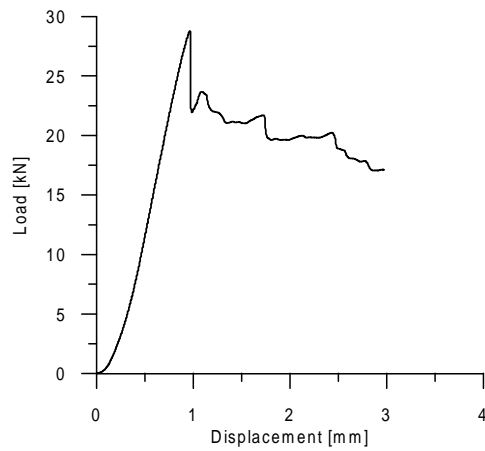
**Figure 7.2:** *Guillotine cross-fibre-tearing failure for 12 mm dowel.*

$t$ [mm]	n	$F_{bend}$ [kN]		$F_{ult}$ [kN]		$K_{init}$ [kN/mm]	
		mean	stdev.	mean	stdev.	mean	stdev.
21	10	6.1	0.2	6.9	0.36	5.4	0.6
46	10	6.4	0.6	9.7	0.97	5.3	0.8
66	10	6.4	0.4	10.6	0.99	5.3	0.7

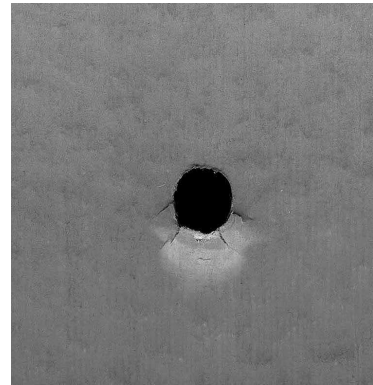
**Table 7.4:** *Load per shear plane for 12 mm connectors at onset of plastic behaviour,  $F_{bend}$ , and at final failure,  $F_{ult}$ . Stiffness per shear plane,  $K_{init}$ , determined at the initial linear part of the load displacement curve.*

Tables 7.4 and 7.5 list ultimate strengths,  $F_{ult}$ , and load corresponding to bend over from the elastic to the plastic regime,  $F_{bend}$ . The values of  $F_{ult}$  is seen to increase with  $t$  whereas the value of  $F_{bend}$  increases markedly less with thickness. The stiffness per shear plane,  $K_{init}$ , has been determined from the initial elastic part of the load displacement curves and is given in Tables 7.4 and 7.5. The initial stiffness is seen not to be influenced by wood member thickness.

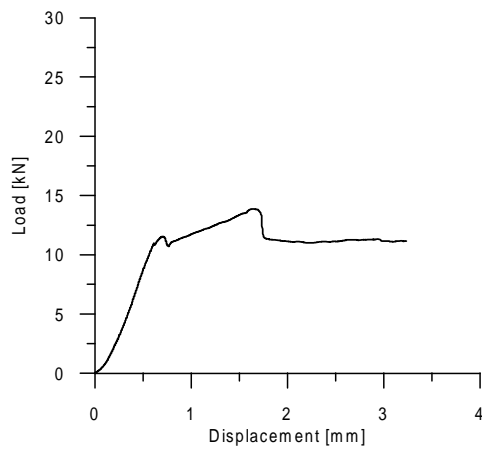
Examples of failed specimens are shown in Figure 7.6. The increased restriction of dowel rotation is seen in Figure 7.6(a)–(c), in Figure 7.6(d)–(e) the failed specimens have been cut open revealing the local plastic failure in the wood. The failures were all regular dowel failures correlated to dowel strength respectively strength of embedment, and not failure correlated to embedment strength of FRP plate, global splitting or shear capacity of wood or FRP plate. For the specimens with 16 mm dowels ultimate dowel failure was



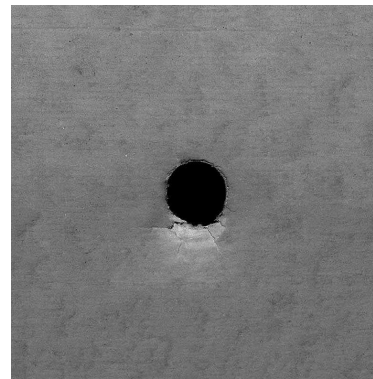
(a) Load displacement, parallel



(b) Embedment failure, parallel



(c) Load displacement, perpendicular



(d) Embedment failure, perpendicular

**Figure 7.3:** *Embedment tests parallel and perpendicular to pultrusion direction.*

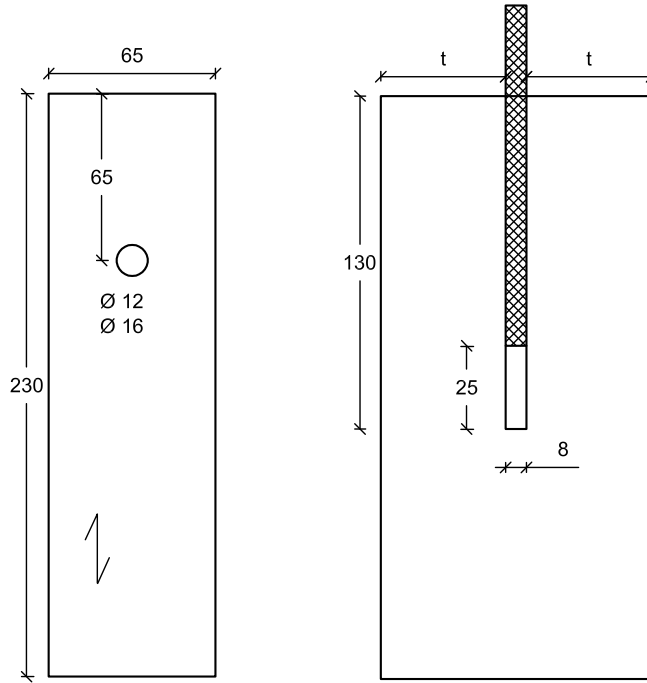


**Figure 7.4:** *Test specimen geometry.*

$t$ [mm]	n	$F_{bend}$ [kN]		$F_{ult}$ [kN]		$K_{init}$ [kN/mm]	
		mean	stdev.	mean	stdev.	mean	stdev.
26	10	10.7	0.3	12.1	0.46	8.7	0.3
56	10	10.6	0.6	15.8	0.72	8.1	1.0
90	10	11.4	0.6	18.3	0.79	8.9	0.8

**Table 7.5:** *Load per shear plane for 16 mm connectors at onset of plastic behaviour,  $F_{bend}$ , and at final failure,  $F_{ult}$ . Stiffness per shear plane,  $K_{init}$ , determined at the initial linear part of the load displacement curve.*

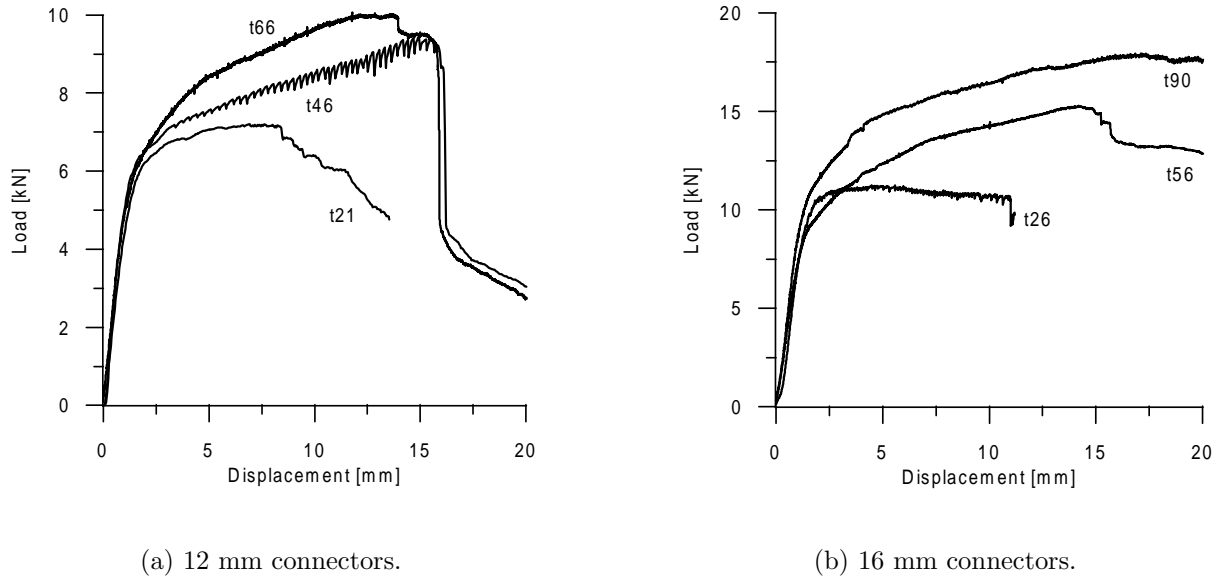


**Figure 7.5:** Load deformation of connector tests with three different wood member thicknesses for both 12 and 16 mm dowels.

followed by brittle wood splitting both in the dowel plane and in the plane of the slotted in plate.

In addition to ordinary connector tests reported in Table 7.4, five tests were made on 12 mm connectors in open holes. The point of this kind of tests is that the failure mode will correspond to the transition between Mode I and Mode II, see Equation (8.2). A mean strength of 11.7 kN (stdev. 0.55 kN) and a length of the embedment failure zone,  $t_{ef}$ , of 16 mm was observed.

## 7.6 Buckling properties

### 7.6.1 Plate bending tests

Three-point bending tests with  $l = 250$  mm were made on  $300 \times 100 \times 8$  mm FPR plates in order to determine the plate bending stiffness. The tests were load controlled with a rate of 0.5 kN/min. The slope of the load-displacement curve,  $P/u$ , is reported in Table 7.6 along with the emerging plate stiffness  $EI$ , which is used to determine the Euler-load.

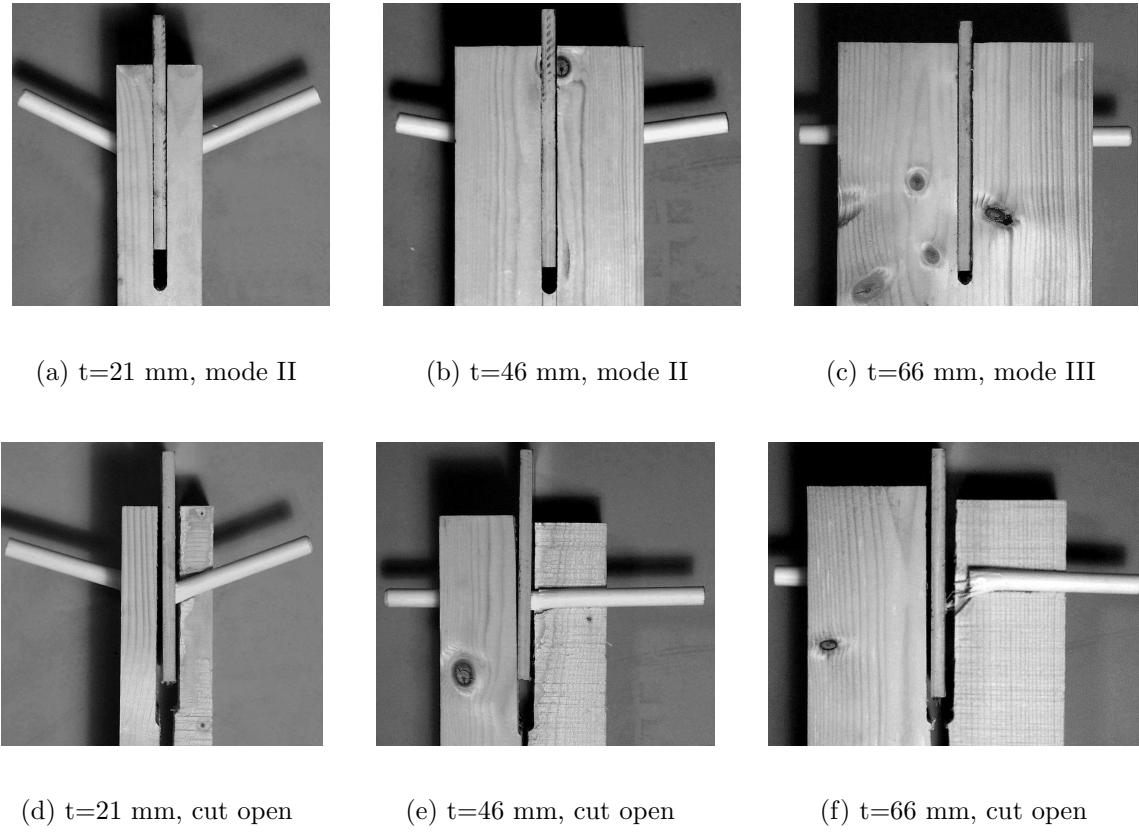


**Figure 7.6:** *Specimens with failed 12 mm dowels.*

	$P/u$ [N/mm]	$EI$ [ $10^6$ Nmm <sup>2</sup> ]	$E$ [GPa]
mean	233	75.8	17.8
stdev.	13.4	4.4	1.0

**Table 7.6:** *Stiffness parameters from 3-point bending tests on plates,  $n=6$*

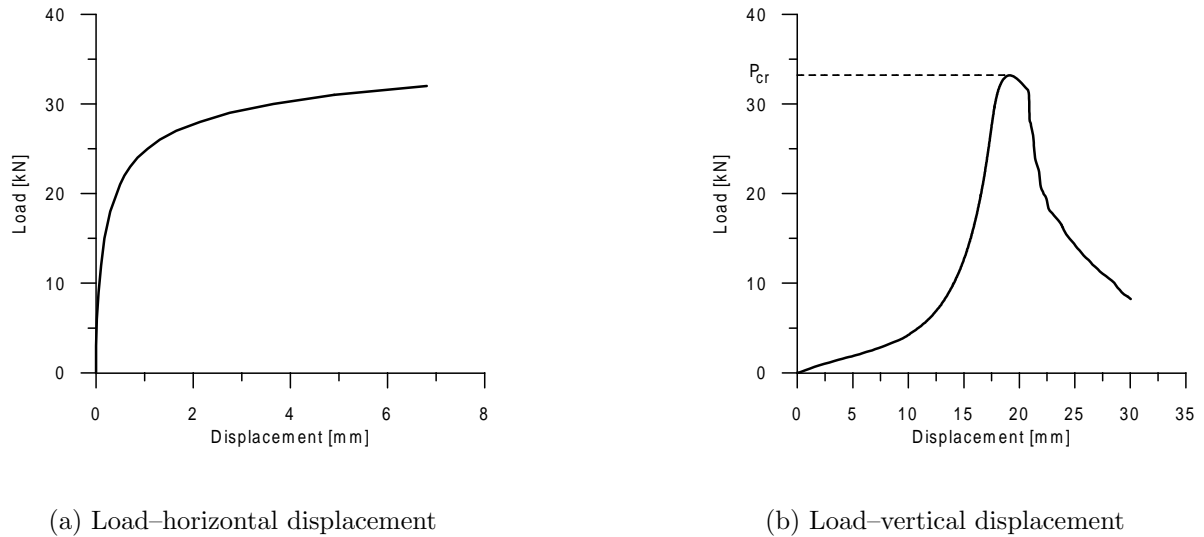


**Figure 7.7:** *Load-displacement curves in buckling.*

### 7.6.2 Buckling tests

The Euler-load  $P_{cr}$  has been determined directly from tests on free simple supported plates. Further tests were made on simple supported plates in slots of different width in order to estimate the stabilising effect of the adjacent wood members. The plates were  $180 \times 100 \times 8$  mm and the tests were load controlled at a rate of 6 kN/min. The critical load,  $P_{cr}$ , given in Table 7.7, is determined as the load corresponding to final failure as shown in Figure 7.7. The initial consolidation seen in Figure 7.7(b) is due to compression of intermediate layers of soft masonite securing pinned like support conditions. The slots used for tests on plates inserted in wood were provided by two pieces of wood spaced by 8, 10 or 12 mm spacers and held together by two clamps. In these tests the critical load was ultimately governed by the external clamping force provided by the clamps. The onset of buckling were in the case of oversized slots observed at the same load level as for the free plates.

Four tests were conducted without intermediate layers of soft masonite. The mean ultimate load for these was 59.9 kN (stdev. 7.4 kN). In these tests the support conditions were between clamped and pinned. After failure, compression indentation was visible at the support edge in the compression side of the buckled specimen.

	Free plate n=6	Slot $w = 12$ mm n=5	Slot $w = 10$ mm n=5	Slot $w = 8$ mm n=6
mean	29.5	47.7	55.6	>100
stdev.	2.8	2.6	7.2	

**Table 7.7:** *Critical load,  $P_{cr}$  [kN], determined on simple supported free plates, and identical plates placed in slots of different width.*

## Chapter 8

# Modelling FRP in dowel type connections

### 8.1 FRP connector modelling

Some of the basic assumptions behind the K. W. Johansen yield theory for dowel connectors may be violated for FRP dowels. They may not be stiff enough to act rigid before plastic failure, the stiffness of FRP is in the order 1/10 of the stiffness of steel, the bending strength is influenced by shear forces and the dowels do not have a plastic plateau unless the failure is dominated by shear. In order to include these deviations from the assumptions of the yield theory the following four models are discussed:

- The traditional plastic strength model with a modification to include shear in the dowel failure criterion.
- The English model, a modified version of the traditional yield model using the dowel cross breaking strength as substitute for the yield moment.
- Models inherited from wood dowels either in form of empirical modifications to the traditional yield model or as extensions including other types of failures.
- A model assuming the FRP dowel is an elastic beam on an elastic-plastic foundation.

#### 8.1.1 Traditional model including shear in dowel

This failure model is a simple extension of the traditional model, just taking into consideration that the strength of FRP dowels cannot be based on bending strength alone, as shown in Chapter 7. Opposed to steel dowels a coupling between shear and moment is

necessary to model the FRP dowel strength. The simplest failure surface in  $M$  and  $V$  is linear, formally stated as:

$$\frac{M}{M_u} + \frac{V}{V_u} = 1, \quad (8.1)$$

where  $M_u$  is the bending strength in a pure bending test and  $V_u$  is the shear strength in a pure shear test. Replacing the yield moment of the dowel in the traditional model with a combined failure criterion as given in 8.1 it is possible to rewrite the traditional strength criterion:

$$F_{M+V} = \min \begin{cases} t d f_h & \text{Mode I} \\ \left( \sqrt{2 + 4 \frac{M_u}{t^2 d f_h} + 4 \frac{M_u}{t V_u} + 4 \left( \frac{M_u}{t V_u} \right)^2} - 1 - 2 \frac{M_u}{t V_u} \right) t d f_h & \text{Mode II} \\ \sqrt{4 M_u d f_h + \left( \frac{M_u d f_h}{V_u} \right)^2} - \frac{M_u}{V_u} d f_h & \text{Mode III} \end{cases} \quad (8.2)$$

### 8.1.2 English model

Due to the observation that the pultruded dowels fail in inter fibre shear rather than yield bending, Drake & Ansell (2000) suggest to replace the plastic yield moment:

$$M_y = f_y \frac{d^3}{6}, \quad (8.3)$$

with a somewhat spurious yield moment determined by use of the cross breaking shear strength,  $f_{c,b}$ :

$$M_y = f_{c,b} \frac{d^3}{6}, \quad (8.4)$$

where the term  $f_{c,b}$  is determined from guillotine shear tests. The mechanics of (8.4) is unclear but it is of course inspired by the experimental fact that shear failure governs the strength of FRP-dowels in wood.

### 8.1.3 Inherited model from wood dowels

Due to the structural similarity between wood dowels and FRP dowels - i.e. high strength and stiffness in fibre direction, low across - and due to the fact that they both differ from steel by means of a lower stiffness, models describing the behaviour of wood dowels may be useful. In (Blass, Ernst & Werner 1999b) experiments on double shear timber to timber connections with wood members of coniferous species and hardwood dowels of oak, beech or azobe are reported. Tests were made at different slenderness ratios,  $\lambda$ , defined as the ratio between middle member thickness,  $t_2$ , and dowel diameter. For  $\lambda \geq 3$  failure is seen in both middle and side member with no increase in strength for higher values, i.e.

the mode III maximum strength is reached. However, the strength cannot be predicted adequately by the mode III load bearing formulae even when the plastic bending moment is replaced by an elastic moment capacity,  $M_{max}$ , of the wood dowel. Hence, a reduction factor,  $\delta$ , to the embedment strength is introduced and the mode III reads:

$$F_{max} = \sqrt{2M_{max} d \delta f_h} \quad (8.5)$$

For  $\delta = 0.75$  the model fits the experimental results. However, the reduced strength could also be due to lack of stiffness of the wood dowels and the hereby reduced rotational restriction capacity.

Sandberg, Bulleit & Reid (2000) treats tenon and mortise joints with wood dowels. For this double shear timber to timber connection the traditional mode I, II, and III failures are given along with dowel bearing failure and dowel cross grain shear failure. Tests are made at different orientations of side and middle member and most reported failures are of the type dowel cross grain shear failure. Though the stiffness of the connection is modelled by use of dowel and wood member stiffness and assumption of stress distribution along the dowel, no attempt is made to revise the K. W. Johansen strength model by use of this more appropriate stress distribution.

#### 8.1.4 Elasto-plastic model

All the preceding models work within the framework of the K. W. Johansen strength model, i.e. with a stress distribution assuming the dowel very stiff compared to the embedment. A more appropriate approach may be to revise the stress distribution by means of a finite element model using empirical values for dowel and embedment stiffness superimposed with a plastic failure criterion for the embedment and an appropriate failure criterion for the dowel. The latter may in the case of FRP dowels be of the form (8.1).

## 8.2 Model implementation

### 8.2.1 Traditional model including shear in dowel

In order to implement the modified failure criterion given in (8.2) a failure surface for the dowels of the form (8.1) is made by use of the experimental data given in Chapter 7.

#### Dowel strength

The strength of the dowels in 3-point bending at different spans is given in Tables 7.1 and 7.2 as critical combinations of system force,  $P$ , and moment,  $M$ . In Figure 8.1 the

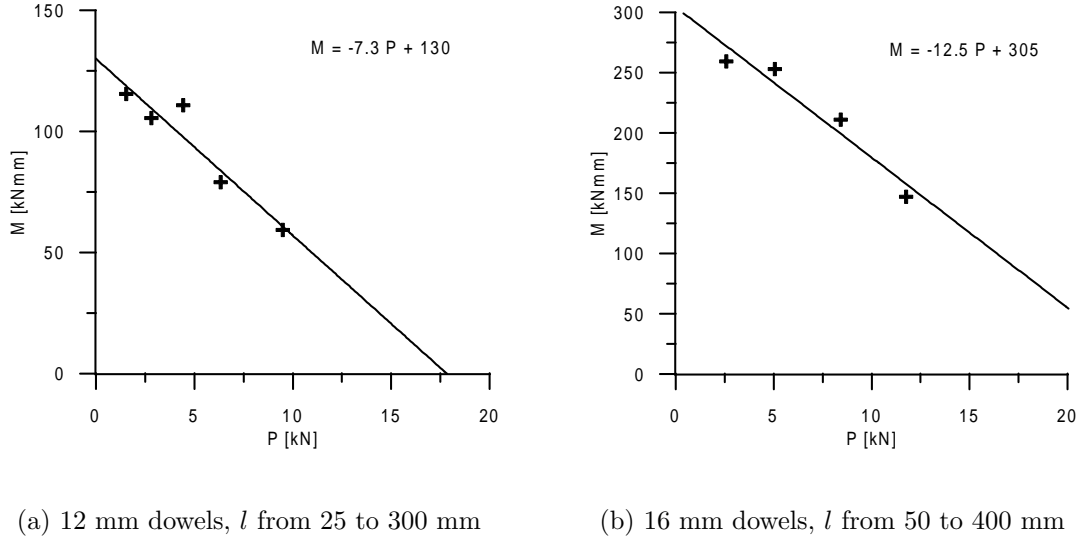


**Figure 8.1:** *Combinations of moment and system shear force leading to dowel failure in 3-point bending at different spans.*

critical combinations have been interpolated to a failure surface for both 12 and 16 mm dowels. For 12 mm dowels the results for spans larger than or equal to 25 mm form a continuum and an interaction between shear and moment is observed. The guillotine and the  $l = 12.5$  mm tests fall outside this continuum as the load cannot be assumed carried according to the technical beam theory. For the same reason the results for 25 mm span have been excluded for 16 mm dowels. The linear failure criterion in shear and moment, (8.1), is verified empirically in Figure 8.1. Using the fits in the figures, observing that  $P_u = 2V_u$ , the failure criterion (8.1) reads:

$$\frac{M}{130 \text{ kNmm}} + \frac{P}{17.8 \text{ kN}} = 1 \quad \text{for } d = 12 \text{ mm} \quad (8.6)$$

$$\frac{M}{305 \text{ kNmm}} + \frac{P}{24.4 \text{ kN}} = 1 \quad \text{for } d = 16 \text{ mm} \quad (8.7)$$

The failure criterion given in (8.1) may be generalised in an elastic or plastic version as given in equations (8.8) and (8.9).

$$\frac{M}{\frac{\pi}{32}d^3 f_m} + \frac{V}{\frac{27}{128}\pi d^2 f_v} = 1 \quad \text{Elastic} \quad (8.8)$$

$$\frac{M}{\frac{1}{6}d^3 f_m} + \frac{V}{\frac{\pi}{4}d^2 f_v} = 1 \quad \text{Plastic} \quad (8.9)$$

	d=12	d=16	mean
$f_m$	767	759	763
$f_v$	93	72	83

**Table 8.1:** *Elastic evaluation of shear and bending strength for 12 and 16 mm dowels, [MPa].*

$t$ [mm]	$F_{bend}$ [kN]	$F_{ult}$ [kN]	Mode	$F_{yieldmodel}$ [kN]	Mode	$F_{M+V}$ [kN]	Mode
21	6.3	6.7	II	7.8	I	5.5	II
46	6.5	8.6	II	10.8	II	7.4	II
66	6.9	9.9	III	12.9	III	9.1	III

**Table 8.2:** *Ultimate strength per shear plane [kN] and failure mode, experimental and modelled, 12 mm dowels.*

The experiments do not leave room for an independent model evaluation, but assuming brittle elastic behaviour the fits corresponding to (8.6) and (8.7) give the bending strengths and shear strengths in Table 8.1. For long spans, when failure is dominated by bending, the test conditions are close to ideal, which is reflected in the identical bending strengths found for the two diameters. For shorter spans, when failure is dominated by shear, the test conditions become increasingly less ideal, as load may not be carried according to the technical beam theory. This may explain the 30 % difference in shear strength found between the 12 and 16 mm dowels. In Table 8.1 the mean value of bending and shear strength based on the two fits (8.6) and (8.7) are given. These values are used for modelling in the proceeding section.

### Connector strength

In Tables 8.2 and 8.3 the mean values of bend over strength,  $F_{bend}$ , and ultimate strength,  $F_{ult}$ , are given. The failure criterion in (2.4) has been used to determine the strengths  $F_{yieldmodel}$ . The value of the plastic yield moment,  $M_y$ , is determined from the bending strengths in Table 8.1. The failure criteria in (8.2) has been used to determine the strengths  $F_{M+V}$  given in Tables 8.2 and 8.3. The value of the ultimate bending strength,  $M_u$ , and the value of ultimate shear strength,  $V_u$ , is determined by use of the mean values of  $f_m$  and  $f_v$  in Table 8.1. The embedment strength is set to 31 MPa, corresponding to the value for all embedment tests in the fibre direction reported in Chapter 3. Neither

$t$ [mm]	$F_{bend}$ [kN]	$F_{ult}$ [kN]	Mode	$F_{yield\ model}$ [kN]	Mode	$F_{M+V}$ [kN]	Mode
26	10.7	12.1	II	12.9	I	9.8	II
56	10.6	15.8	II	18.6	II	12.4	II
90	11.4	18.3	III	23.1	III	16.1	III

**Table 8.3:** *Ultimate strength per shear plane [kN] and failure mode, experimental and modelled, 16 mm dowels.*

$t$ [mm]	$F_{bend}$ [kN]	$F_{ult}$ [kN]	Mode	$F_{c,b,103}$ [kN]	Mode	$F_{c,b,158}$ [kN]	Mode
21	6.3	6.7	II	5.1	II	6.0	II
46	6.5	8.6	II	6.4	III	8.2	III
66	6.9	9.9	III	6.4	III	8.2	III

**Table 8.4:** *Ultimate strength per shear plane [kN] and failure mode, experimental and modelled, 12 mm dowels.*

of the models are able to model  $F_{bend}$ . The yield model is too optimistic in the prediction of ultimate strength, which reflects that the model cannot take into account the shear dependency of the dowel strength. The model including shear is somewhat conservative - probably because not all load is carried according to the beam theory, some is taken from plate to embedment in compression through the dowel as a solid. The model has however the merit of being able to predict the correct failure modes.

### 8.2.2 English model

In Tables 8.4 and 8.5 the strength per shear plane,  $F_{c,b}$ , is determined by use of the yield model, (2.4), and dowel yield moment determined by use of the cross breaking strength, (8.4), as suggested in (Drake & Ansell 2000). Two model evaluations are made using different cross breaking shear strengths determined from guillotine tests. Drake & Ansell (2000) reports a mean value of  $f_{c,b} = 103$  MPa, whereas the value  $f_{c,b} = 158$  MPa is found from Table 7.1 using the transformed shear area  $A_w = \frac{27}{128}\pi d^2$ . The dowel material behind both values have identical fibres and matrix. The values  $F_{c,b,103}$  underestimates  $F_{ult}$  whereas  $F_{c,b,158}$  yields better predictions both in strength and failure mode. Even so, the theory behind the model is highly unclear as a shear strength is used to determine a bending strength.

$t$ [mm]	$F_{bend}$ [kN]	$F_{ult}$ [kN]	Mode	$F_{c,b,103}$ [kN]	Mode	$F_{c,b,158}$ [kN]	Mode
26	10.7	12.1	II	8.8	II	10.5	II
56	10.6	15.8	II	11.8	III	14.2	II
90	11.4	18.3	III	11.8	III	14.6	III

**Table 8.5:** *Ultimate strength per shear plane [kN] and failure mode, experimental and modelled, 16 mm dowels.*

### 8.2.3 Inherited models

A use of the cross breaking strength more rational than in the English model is to add a cross breaking failure mode as an additional mode to the traditional bending or bearing modes, as done in (Sandberg et al. 2000). However, a direct use of the guillotine cross breaking strength gives strength per shear plane of 15.1 kN for 12 mm dowels and 26.8 kN for 16 mm dowels. As seen from the ultimate strengths in Table 8.4 and 8.5 this failure mode is never realised.

### 8.2.4 Elasto-plastic model

The lack of rigidity of the FRP dowels may lead to a stress distribution along the embedment which differs significantly from the stress distribution assumed under the rigid plastic assumption by K. W. Johansen. The need for an elasto-plastic modelling of the FRP-dowels arises as the invariance of  $F_{bend}$  to wood member thickness points to the lack of bending rigidity of the dowels. The aim is to model the bend over point from elastic to plastic regime as seen in Figure 7.5. In order to make a numerical simulation of the stress distribution the embedment stiffness and the dowel stiffness is needed.

#### Dowel stiffness

The experimentally determined system stiffnesses reported in Chapter 7 are resumed in Tables 7.1 and 7.2. The system stiffness is determined as  $P/u_{tot}$ , where  $u_{tot}$  is the mid span deflection determined in 3-point bending. Taking both shear and moment deformation into consideration the total mid span deflection is:

$$u_{tot} = u_M + u_V = \frac{Pl^3}{48EI} + \frac{Pl}{4GA_w}, \quad (8.10)$$

where  $A_w$  is the transformed shear area  $\frac{27}{128}\pi d^2$  and  $E$  and  $G$  are the longitudinal E-modulus and the inter-fibre shear modulus, respectively. In Tables 8.6 and 8.7 the system

Span $l$ [mm]	Experimental stiffness [kN/mm]	Modelled stiffness excl. shear [kN/mm]	Modelled stiffness incl. shear [kN/mm]
300	0.056	0.069	0.065
150	0.42	0.55	0.44
100	1.13	1.86	1.20
50	3.4	14.9	4.6
25	9.0	120	12.1
12.5	<i>11.3</i>	<i>956</i>	<i>26.2</i>
$\simeq 0$	<i>30.22</i>	-	-

**Table 8.6:** *Experimental and modelled system stiffness in three point bending of 12 mm dowels.*

Span $l$ [mm]	Experimental stiffness [kN/mm]	Modelled stiffness excl. shear [kN/mm]	Modelled stiffness incl. shear [kN/mm]
400	0.084	0.092	0.087
200	0.67	0.74	0.59
100	3.29	5.9	2.97
50	11.2	47	9.6
25	25.0	<i>378</i>	<i>22.6</i>

**Table 8.7:** *Experimental and modelled system stiffness in three point bending of 16 mm dowels.*

stiffness has been modelled by use of the compliance:

$$\frac{u_{tot}}{P} = \frac{u_M + u_V}{P} = \frac{l^3}{48EI} + \frac{l}{4GA_w} \quad (8.11)$$

The longitudinal E-modulus and inter-fibre shear modulus is set to  $E = 38$  GPa and  $G = 0.88$  GPa, respectively. It is seen that the system stiffness cannot be adequately modelled without shear deformations. For small span-to-diameter ratios load is not carried according to the technical beam theory and deflections cannot be modelled according to (8.10). A small span-to-diameter ratio is found for  $l$  below 25 mm for 12 mm dowels and for  $l$  below 50 mm for 16 mm dowels, hence modelled and experimental values for these spans are set in italic in Tables 8.6 and 8.7.

Dowel $d$	Embedment		Dowel	
	$f_h d$ [MPa mm]	$K_{Ed}$ [MPa]	$EI$ [MN mm <sup>2</sup> ]	$GA$ [kN]
12 mm	378	382	38.7	95
16 mm	504	509	122	149

**Table 8.8:** *Model input for numerical modelling of elastic FRP dowels on elasto-plastic embedment.*

### Elasto-plastic model input

A two-dimensional numerical model of an elastic FRP dowel modelled as an elastic beam resting in an elasto-plastic embedment is made using the input data in Table 8.8. The embedment properties are taken from Table 3.4 with  $\alpha = 0^\circ$ ; the used assumption of perfect plasticity in the grain direction is verified from Figure 3.4 (a). The dowel properties are calculated under the assumption that the dowel carries the load as a beam with bending and shear deflections governed by the stiffness parameters  $E$  and  $G$  as determined in the preceding section. The geometry used in the modelling corresponds to the geometry for the experiments reported in Chapter 7.

### Elasto-plastic model results

The modelling result is shown in Figure 8.2. It is obvious from the nonlinear load displacement result of the modelling that the behaviour is not rigid plastic. That is, the uneven stress distribution along the dowel gradually plasticize the embedment. However, this nonlinear response is way to weak to explain the shape of the experimental load displacement curves. Variations have been made to the elastic stiffness of the dowels and it is not possible to obtain a realistic load displacement response within realistic variations of the stiffness parameters. In other words, the elasto-plastic model shows that it is not the lack of elastic stiffness of the dowels that governs the value of  $F_{bend}$  and its invariance to wood member thickness.

## 8.3 Model comparison

### 8.3.1 Failure definition

From the experimental results in Chapter 7 it is observed that for a given dowel diameter the bend-over point from elastic to plastic regime is independent of wood member thickness. This is very different from the behaviour of a steel dowel connection. In order

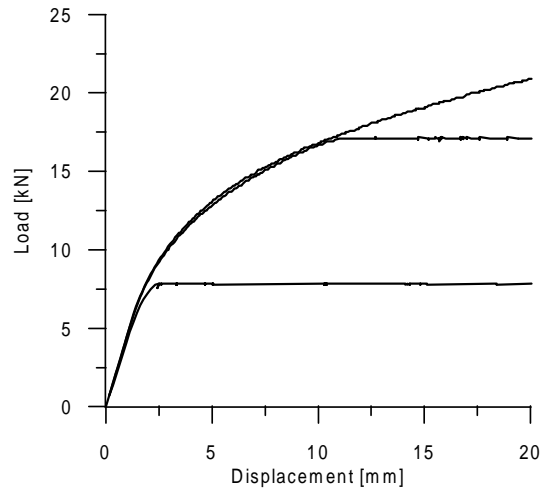


**Figure 8.2:** Load displacement from elasto-plastic modelling,  $d=12$  mm and  $t=21$  mm,  $t=46$  mm and  $t=66$  mm.

to compare the behaviour of a steel dowel with the behaviour of an FRP dowel, load displacement curves are given for both types of connections. Figure 8.3(a) shows load displacement curves for double shear steel dowel connections with three different wood member thicknesses realising all three failure modes. The load displacement curves have been normalized with the maximum value for load and displacement for the mode III connection. Figure 8.3(b) shows the same for FRP dowel connections. In the steel connections the difference between  $F_{ult}$  and  $F_{bend}$  is insignificant, at least for loading in the grain direction, and the values of  $F_{bend}$  lies distinct for the different modes. Contrarily for FRP dowels, a difference between  $F_{ult}$  and  $F_{bend}$  is observed and the values of  $F_{bend}$  are independent of failure mode or wood member thickness as seen in Figure 8.3(b). Though it is observed that the ultimate strength of FRP connectors follows the anticipated trend where connectors in wider pieces of wood gain in strength, Tables 8.2 and 8.3, the coinciding values of  $F_{bend}$  make this observation more academic. This is of course a matter of failure definition. As the rigid plastic assumption is appropriate for a steel connector and as a such connection exhibits almost perfect plasticity, at least in the grain direction, the failure strength is the strength at onset of plastic behaviour. To use the ultimate strength as a measure for failure strength of FRP connectors entails up to 60 % overestimation of the strength corresponding to onset of plastic behaviour. Hence, the ultimate strength is clearly unsatisfying as measure for failure strength as the failure strength must be identified with the load at which permanent damage first occurs, i.e.  $F_{bend}$ .

In terms of failure definition and basic model assumptions all models discussed except

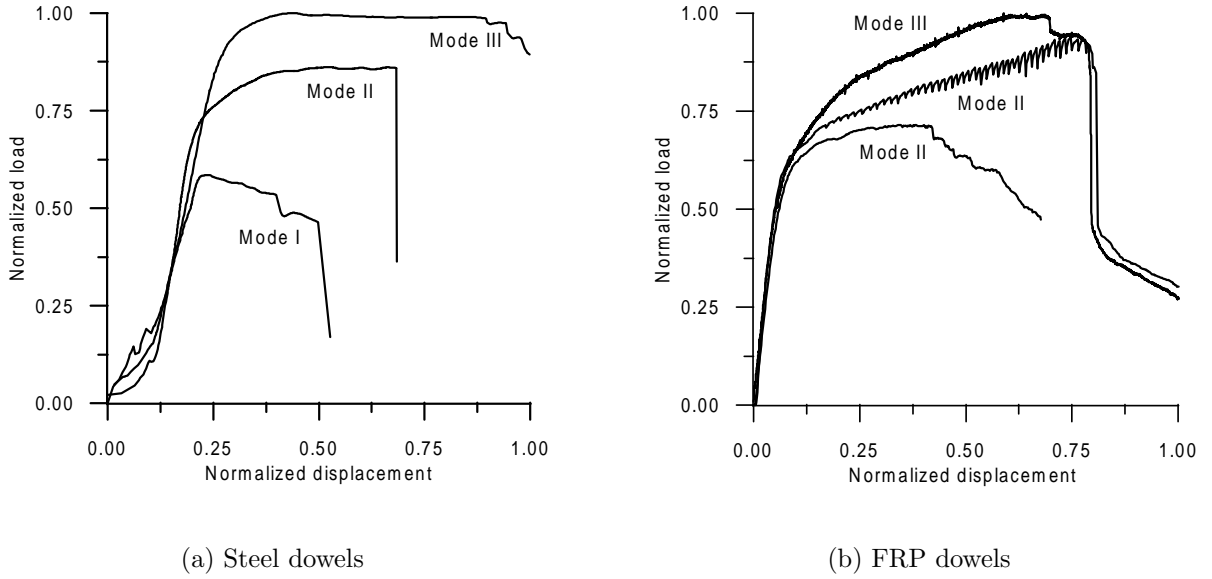


**Figure 8.3:** Normalized load displacement curves for steel and FRP connectors loaded in the grain direction.

the elasto-plastic work within the dowel rigidity assumption of K. W. Johansen, where wider wood members enhance the rotational restriction and increases the strength.

### 8.3.2 Comparison between models

As a tool to compare the strength prediction efficiency of the models the model coefficient of variance,  $COV_{model}$ , is used. It is determined as:

$$COV_{model} = \frac{\sqrt{\frac{\sum_{i=1}^n (F_{model} - F_{ult})^2}{n}}}{\bar{F}_{ult}} \quad (8.12)$$

In Table 8.9  $COV_{model}$  is given along with model failure mode score. The models  $F_{M+V}$  and  $F_{c,b,158}$  predicts ultimate strengths closest to the experimental results. The model  $F_{M+V}$  yields the highest score on correct failure mode prediction and is to be preferred compared to the cross breaking models for theoretical reasons.

The elasto-plastic modelling showed that lack of elastic stiffness of the dowel was not able to explain the invariance of  $F_{bend}$  to wood member thickness. The main reason to employ an elasto-plastic modelling of the FRP-dowels was the idea that low dowel stiffness decreased the ability to transfer the clamping moment from the outer part of the dowel to the loaded central section. Though this cannot be explained by the low elastic

	$F_{yield}$	$F_{M+V}$	$F_{c,b,103}$	$F_{c,b,158}$
$COV_{model}$ [%]	23	17	32	16
Failure mode score	4/6	6/6	4/6	5/6

**Table 8.9:** *Coefficient of variation and failure mode score between model prediction and experimental results of  $F_{ult}$ .*

stiffness of the FRP-dowels the experimental evidence is that the FRP connectors enter the plastic regime at a load  $F_{bend}$  which is only marginally influenced by the wood member thickness. As already mentioned this is a behaviour very different from the behaviour of steel connectors as shown in Figure 8.3.

The elasto-plastic model is clearly too simple with respect to the material properties of the FRP-dowels as the observed shear plasticization, Figure 7.1 (e) and (f), is not included. An impending shear delamination and corresponding plasticization is obviously equal to loss of stiffness. What actually happens in the dowels may be a more complex matter not adequately described by the combined failure criteria (8.1) implemented in the yield model (8.2).

In an effort to model the invariance of  $F_{bend}$  a simplified and conservative means is to neglect the clamping moment at onset of shear dominated failure as shown in Figure 8.4. Neglecting the clamping force corresponds to stipulate that  $F_{bend}$  takes place in the transition between mode I and II.

The wood member thickness in the transition between mode I and II,  $t_{I-II}$ , can by use of the connection strength criterion given in (8.2) be expressed as:

$$t_{I-II} = \sqrt{\left(\frac{M_u}{V_u}\right)^2 + \frac{2 M_u}{d f_h}} - \frac{M_u}{V_u} \quad (8.13)$$

The theoretical strength in the transition,  $F_{M+V, \text{transition I-II}}$ , is determined by use of  $t_{I-II}$  and the failure criteria for 12 and 16 mm dowels in (8.6) and (8.7). The experimental transition strength,  $\bar{F}_{open}$ , is found from four tests with dowels in open holes, a geometry which automatically seeks the transition between mode I and II. In Table 8.10  $F_{M+V, \text{transition I-II}}$  and  $\bar{F}_{open}$  are given along with  $\bar{F}_{bend}$ . There is full correspondence between  $F_{M+V, \text{transition I-II}}$  and  $\bar{F}_{open}$ , however the mean values of  $F_{bend}$  are higher than  $F_{M+V, \text{transition I-II}}$  as the model is conservative due to the total negligence of clamping moment. What the coarse model proposes is simply to neglect wood member thickness in excess of  $t_{I-II}$  and to use (8.13) in combination with (8.2) to determine  $F_{bend}$ . The ultimate brittle strength  $F_{ult}$  is determined by use of the true wood member thickness

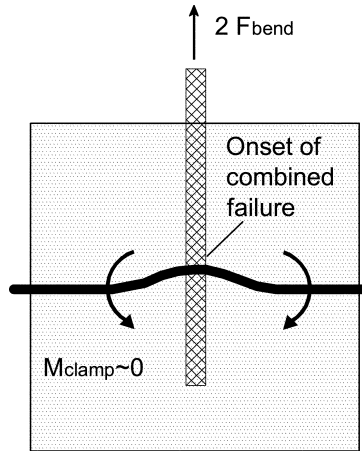


**Figure 8.4:** Clamping condition at  $F_{bend}$  assuming  $M_{clamp} \sim 0$

$d$ [mm]	$F_{M+V, \text{transition I-II}}$	$\bar{F}_{open}$	$\bar{F}_{bend}$
12	5.8	5.9	6.6
16	9.0	-	10.9

**Table 8.10:** Theoretical value of strength in transition between mode I and II compared with test results from dowels in open holes and mean value of  $F_{bend}$ .

in (8.2). This coarse two step model fits the experimental data. However, it has a clear theoretical flaw as it is unclear how the central moment can be relieved after onset of shear plasticization which entail loss of bending stiffness.

### 8.3.3 Comparison with steel

When FRP connectors are appraised for their large ductility, (Drake et al. 1999), it should be observed that this ductility is on the expense of strength and that the ductility entails local plastic damage of the wood at low load levels. In Table 8.11 values for the strength of steel dowels in wood members of the same thickness as used in the FRP experiments are given. The value of  $F_y$  based on Equation (2.4) is given as mean value based on experiments on standard electro galvanized dowels,  $f_{y,steel} = 640$  MPa. In the Danish code, (Larsen & Riberholt 1991), a characteristic yield strength in excess of 240 MPa cannot be used unless the dowel spacing in the fibre direction is increased with the factor  $\sqrt{f_{y,k}/240}$ . Hence,  $F_y$  is also given as a pseudo mean value based on the maximum

	12 mm dowels			16 mm dowels		
	t=21	t=46	t=66	t=26	t=56	t=90
$F_{bend}$ - FRP	6.3	6.5	6.9	10.7	10.6	11.4
$F_y$ - Steel, 640 MPa	7.8	12.2	13.9	12.9	21.3	25.0
$F_y$ - Steel, 240 MPa	7.2	10.1	10.1	12.7	15.4	18.0

**Table 8.11:** Comparison FRP and steel, strength per shear plane, [kN].

	$F_{h,FRP,0}$	$F_{h,FRP,90}$	$2F_{bend}(max,FRP)$	$2F_y(mode III, steel)$
d12	27.4	13.2	13.8	33.1
d16	36.5	17.7	22.8	58.8

**Table 8.12:** Embedment capacities of 8 mm FRP plates and maximum load bearing capacities for double shear dowels of FRP and steel, [kN].

allowed characteristic yield strength of the dowel steel  $f_{y,steel} = 240$  MPa. In both cases an experimental mean value of the embedment strength of 31 MPa is used. The bend-over strengths of the FRP connectors are significantly smaller than the corresponding strengths for a standard steel dowel connection.

## 8.4 FRP plates

### 8.4.1 Embedment strength of FRP plates

In Table 8.12 the embedment capacities of 8 mm FRP plates are given both parallel and perpendicular to pultrusion direction based on the experimental values in Table 7.3. Further, the table lists maximum dowel capacities for double shear FRP and steel connectors. The FRP embedment strength is prohibitive in the direction perpendicular to pultrusion when using FRP dowels and always prohibitive in case of steel dowels. It should be observed that  $2F_y(mode III, steel)$  is based on the experimental mean of a standard dowel with mean  $f_y = 640$  MPa and not the maximum allowed characteristic value, the latter is found by division with 1.6. Besides embedment failure Fiberline Composites (1995) lists four other failure mechanisms of an FRP plate loaded through a dowel, none of which are prohibitive.

### 8.4.2 Buckling of FRP plates

The use of thin slotted-in elements in connections in compression may lead to stability failure of the slotted-in element. Stability failure poses a real problem for slotted-in FRP plates compared to steel as the stiffness of FRP is only approximately 10% of that of steel. In a compressive connection, buckling of the slotted-in FRP plate may be strength limiting unless the adjacent wood members are able to provide transverse support. By use of the mean stiffness  $EI$  determined from bending, Table 7.6, the theoretical Euler load of 180 mm high 100 x 8 mm plates is found to be 23 kN using:

$$P_{Eu} = \frac{\pi^2 EI}{l_s^2} \quad (8.14)$$

This value is somewhat lower than the experimental mean value,  $P_{cr} = 29.5$  kN, found for the free simple supported plate in Table 7.7. The discrepancy probably arises as the tested plates were not ideally pinned. The tests without intermediate layers of masonite, resulting in less pinned border conditions, had buckling loads two times higher than the more pinned tests with intermediate layers of masonite.

The ability of the adjacent wood members to support the plates and increase the buckling loads is observed in Table 7.7. The tighter fitting slots the higher critical load. For both 10 and 12 mm slot widths, buckling of the FRP-plate was initiated at the same load level as for the free plate, but ultimately the critical load was governed by the unknown clamping force provided by the adjacent wood members. For tight fitting slots buckling failure was not observed below the test machine capacity of 100 kN. Though not directly quantified, the forces required to open the clamps as shown in Figure 8.5 were substantial. As a rough estimate based on observed yielding in the clamps, final failure was reached when the transverse stabilizing force was in the order 1 kN.

An estimate of the buckling problem in structural use of slotted-in FRP plates could be made as follows:

- The width of the buckling plate is 100 mm, with  $4d$  inter dowel column spacing corresponding to two columns of 12 mm dowels.
- The free length of 180 mm corresponds to the maximum free length between dowel rows in two butt jointed glulam elements connected with a slotted-in plate and 12 mm dowels, i.e.  $180 \text{ mm} \simeq 2 \cdot 7 \cdot 12 \text{ mm}$ .
- Assuming a maximum strength per dowel of approximately 14 kN, about 2 consecutive dowel rows are possible if the slots are 2 mm oversized,  $2 \cdot 2 \cdot 14 \text{ kN} \leq 56 \text{ kN}$ .

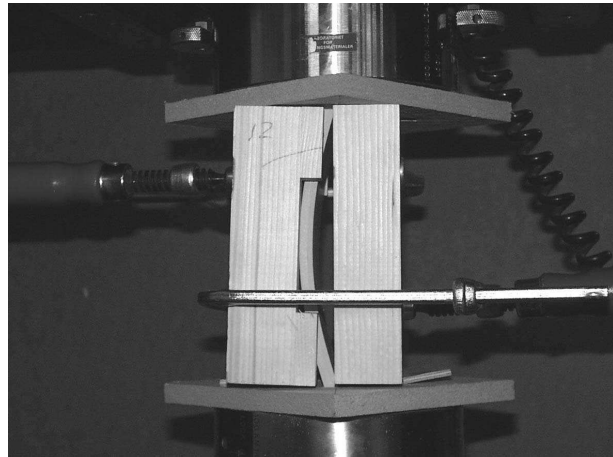


**Figure 8.5:** *Buckling of plate in oversized slot, clamps opened by horizontal buckling generated forces.*

- This requires a transverse support of the order 1 kN.

This estimate covers the worst case scenario, a more common use would be the connection between web and flange in a glulam truss girder. In this case the distance between rows in web and flange would be  $11d$  leaving room for 3 consecutive dowel rows – and of course if the slots fit tighter and higher transverse forces are obtainable in real structures the number of possible dowel rows will increase.

## Chapter 9

# Conclusion

Dowel type timber connections have been studied with main focus on loading where the dowels act on the embedment with an angle to the grain. Splitting failures are known to occur even for dowel type connections loaded in the grain direction. However, in this work splitting is studied when the dowels act directly in the transverse direction of the wood. The objective is to study the range of validity of yield modelling of dowels and dowel groups when transverse load is present. This is done by means of a yield surface determined for the single connectors, implemented in a modelling of joints containing a group of dowels exposed to loads in the axial and transverse direction of the wood member.

Further a study on the use of fibre reinforced plastic, FRP, as replacement for steel in dowels as well as insertion plates is presented.

In order to construct a realistic yield surface for the single connector, the embedment strength has been determined in a block test covering glulam specimens with an average density of  $470 \text{ kg/m}^3$  and angles to grain of 0, 30, 60 and  $90^\circ$ . With respect to the current code rules the following observations are made:

- For loading in the grain direction the embedment acts elastic-perfect plastic and the embedment strength corresponding to transition from elastic to plastic regime can be determined by use of the density-diameter rule in (EC5-1 1995).
- For loading perpendicular to the grain the embedment acts elastic-plastic hardening. The embedment strength corresponding to transition from elastic to plastic regime is overestimated approximately 50 % by the rule in (EC5-1 1995). The embedment strength perpendicular to the grain predicted by the Eurocode rules corresponds to approximately 5 mm plastic deformation. This deformation is two to three times larger than the deformation at onset of plastic behaviour for loading parallel to the grain.

- Differences in the embedment strength perpendicular to grain is traced when the embedment utilizes the compression strength in the radial and tangential direction respectively. This difference is explained by use of structural differences of the cell wall layout in the two directions.
- The embedment perpendicular to grain is tested at two levels of moisture content and a strength reduction corresponding to approximately 2% per percent nominal increase in moisture content is found.

Moment rigid joints containing two dowels and a slotted in steel plate have been tested in bending at two moisture levels and with different end and inter dowel spacings. The findings are:

- Brittle splitting failure is obtained prior to a load corresponding to embedment failure for joints designed in accordance with the distance requirements in (EC5-1 1995).
- The brittle splitting strength is found to increase for increased inter dowel spacing and to be almost invariant to end distance.
- The brittle splitting strength is found to be invariant to moisture content. Tension perpendicular to the grain tests exhibits the same invariance to moisture content.
- It is not possible to explain the splitting failures by a shear based design criterion.

Full scale joints designed with a slotted in steel plate and 4x4 dowels have been tested in axial tension, eccentric transverse loading and combinations of the two. Tests have been made with two different wood member thicknesses. A yield surface for the single connector is established by use of the empirically determined embedment and dowel properties. The conclusions are:

- For pure axial loading plastic modelling is sensitive to the accurateness of the mechanical part of the plastic model, that is:
  - The loading eccentricity of the dowel due to the width of the slot for the slotted in steel plate should be included in the model. Neglecting this eccentricity gives 20% to high estimates of the yield capacity. The eccentricity is not included in the Eurocode rules which assumes that the slot and steel plate has no extension.

- 
- For oversized dowel holes in the wood, clamping of the dowel may not be present and yielding takes place at lower loads than expected. In combination with the eccentricity this may lead to 40% to high estimates of the yield capacity. An approximate model taking the effect of oversized holes into account by limiting the effective wood member thickness to the transition between mode II and III is able to model the strength values obtained.
  - A plastic modelling of the connections assuming ideal plastic behaviour and using empirically determined strength values for the embedment shows that:
    - A first yield criteria corresponding to the limit of the elastic load bearing capacity for the severest loaded connector is a safe design criteria for all levels of the transverse load.
    - A full yield criteria corresponding to yielding in all connectors is safe only for small values of the transverse load. In the tested configuration this small value corresponds to 5% of the plastic axial capacity.
  - Brittle splitting failures are seen to take place at load combinations indicating a strong interaction between axial loading and transverse loading. The brittle failures cannot be modelled by assuming that the relative impact of each of the two load components is additive. A purely empirical fit fits the results assuming the impact of the relative transverse utilization to be quadratic and the axial to be linear. Any physical explanation to this has however not been investigated.
  - The brittle splitting capacity is found to be almost invariant to a 60 % increase in the wood member thickness. The finding cannot be explained by criteria that assumes the brittle strength, i.e. tension perpendicular to the grain or shear strength, to be linear in the wood member thickness.

The behaviour of FRP dowels in connections with slotted in FRP plates has been investigated. The test series comprises two dowel diameters, each studied at three wood member thicknesses. The objective was to assess whether FRP materials are feasible as replacement for steel in dowel type connections, the anticipated advantages being production ease, enhanced production precision and better performance in fire and aggressive environments. The following conclusions are made:

- The shear strength for FRP dowels is found to be low. Bending tests on FRP dowels

taken to failure at different spans show that a failure criterion for FRP dowels resting on both bending and shear stresses is appropriate.

- It is characteristic for the load displacement curves for the FRP dowel connections that after onset of plastic behaviour strain hardening is observed and the strain hardening increases with increased wood member thickness. Tests show an ultimate strength loss due to brittle dowel failure.
- The bend over strength of an FRP connector, i.e. the load corresponding to onset of plastic behaviour of the connector, is invariant to wood member thickness. That is, the classical yield theory cannot predict onset of plastic behaviour.
- An elasto-plastic model taking the low dowel stiffness into account has been employed in order to investigate if it is the low dowel stiffness that prevents effective use of the wood member thickness. This has not been verified.
- The bend over strength may be modelled by:
  - The dowel failure criterion combining moment and shear.
  - A modification to the traditional yield model for steel connectors in wood, to include the combined dowel failure criterion.
  - An effective wood member thickness corresponding to the transition from mode I to II.
  - For the investigated dowels the effective wood member thickness corresponds to 18 and 22 mm in the case of 12 and 16 mm dowels, respectively.
- The ultimate strength of an FRP connector can be modelled by use of:
  - The dowel failure criterion combining moment and shear.
  - A modification to the traditional yield model for steel connectors in wood, to include the combined dowel failure criterion.
- FRP connectors are found to be significantly weaker than standard steel connectors of the same diameter. For the widest wood members investigated the reduction compared to steel is in the order:
  - 50 % when comparing with the bend over strength of the FRP connector.
  - 25 % when comparing with the ultimate strength of the FRP connector .

- The use of FRP insertion plates is limited by two factors; buckling and embedment failure of the plate embedment. The stability load of FRP plates has experimentally been found to be prohibitive for an 8 mm plate and more than 2 dowels in a row. The embedment strength of FRP plates is too small to get full benefit of a steel dowel if an 8 mm plate is used.

Following from the above conclusions it cannot generally be recommended to use FRP dowels and plates as substitute for steel in timber connections. The production ease, production accuracy and the fire resistance arguments cannot counterweigh the lower strength compared to steel dowels. FRP materials may however have a role as a substitute for steel in aggressive environments.



# Bibliography

- Bertsche, P. (1993), A new connecting system for engineered wood constructions, *in* 'International workshop on wood connectors', Forest Products Society, pp. 65–66.
- Blass, H. J., Bienhause, A. & Krämer, V. (2000), Effective bending capacity of dowel-type fasteners, *in* 'CIB/W18 meeting Delft, The Netherlands', Universität Karlsruhe, pp. 33–7–5.
- Blass, H. J., Ehlbeck, J. & Rouger, F. (1999*a*), Simplified Design of Joints with Dowel-type Fasteners, *in* G. B. Walford & D. J. Gaunt, eds, 'Pacific Timber Engineering Conference', Vol. 3, Rotorua, New Zealand, pp. 275–279.
- Blass, H. J., Ernst, H. & Werner, H. (1999*b*), 'Verbindungen mit Holzstiften', *Bauen mit Holz* **99**(10), 45–52.
- Chen, C. J., Natterer, J. & Haller, P. (1994), Experimental Study on Fibre Glass Reinforced Timber Joints, *in* 'Proceedings of the Pacific Timber Engineering Conference, July 11–15, 1994', Vol. 2, Gold Coast, Australia, pp. 66–72.
- CIB (1983), Structural timber design code, Publication 66.
- Core, H. A., Côté, W. A. & Day, A. C. (1976), *Wood. Structure and identification*, Syracuse University Press, New York, USA.
- Dinwoodie, J. M. (1981), *Timber. Its nature and behaviour*, Van Nostrand Edition, London, England.
- Drake, R. & Ansell, M. P. (2000), 'Evaluation of double shear-joints for timber structures using pultruded grp dowels, and implication for ec5 based design', *The Structural Engineer* **78**(12), 28–32.

- Drake, R., Ansell, M., Aram, J., Mettem, C. & Bainbridge, R. (1996), Advancement of structural connection techniques for timber structures, *in* S. Aicher, ed., 'Proceedings of the 1996 International Conference on Wood Mechanics, Stuttgart, Germany, May 14–16, 1996', pp. 354–364.
- Drake, R., Ansell, M., Aram, J., Mettem, C. & Bainbridge, R. (1998*a*), Non-metallic Connections for Timber Structures, *in* J. Natterer & J.-L. Sandoz, eds, '5th World Conference on Timber Engineering, August, 1998', Vol. 2, Presses polytechniques et universitaires romandes, pp. 577–584.
- Drake, R., Ansell, M., Aram, J., Mettem, C. & Bainbridge, R. (1999), Non-metallic Adhesiveless Joints for Timber Structures, *in* 'CIB/W18 meeting, Graz, Austria', pp. 32–7–11.
- Drake, R., Aram, J. & Ansell, M. (1998*b*), 'The Performance of Pultruded GRP Connectors in Multiple Dowelled Double Shear Timber Joints', *Journal of the Institute of Wood Science* **14**(6), 277–283.
- DS 413 (1982), Danish Code for Timber Constructions (in Danish), Code NP-158-N, Dansk Ingeniørforening, Copenhagen, Denmark.
- DS 413 (5.1) (1999), Code of Practice for the structural use of timber (in Danish), Code NP-158-N, Dansk Ingeniørforening, Copenhagen, Denmark.
- EC5-1 (1995), Eurocode 5 – Design of timber structures – Part 1–1: General rules and rules for buildings, Preliminary building code prENV 1995-1-1, European Committee for Standardization.
- EC5-2 (1997), Eurocode 5 – Design of timber structures – Part 2: Bridges, Preliminary building code prENV 1995-2, European Committee for Standardization.
- EN 383 (1993), Timber structures – Test methods – Determination of embedding strength and foundation values for dowel type fasteners, Test method standard, European Committee for Standardization.
- Eskildsen, L. (1999), Samlinger i trækonstruktioner (in Danish), Final thesis, BKM, Technical University of Denmark.
- Fiberline Composites (1995), Fiberline – Designmanual, Technical report, Fiberline Composites A/S, Kolding, Denmark. in Danish.

- Gibson, L. G. & Ashby, M. F. (1988), *Cellular Solids, Structure and Properties*, Pergamon Press, Oxford, England.
- Haller, P., Chen, C. J. & Natterer, J. (1996), Experimental Study on Glass Fibre Reinforcement and Densified Timber Joints, *in* V. K. A. Gopu, ed., 'Proceedings of the International Wood Engineering Conference, October 28–31, 1996', Vol. 1, New Orleans, Louisiana, USA, pp. 308–314.
- Hearmon, R. F. S. (1948), The elasticity of wood and plywood, Special Report 7, Forest Products Research, London.
- Johansen, K. W. (1941), 'Forsøg med træforbindelser (in Danish)', *Bygningsstatistiske meddelelser*.
- Johansen, K. W. (1949), 'Theory of timber connections', *International Association of Bridge and Structural Engineering Publication 9*, 249–262.
- Jorissen, A. (1998), Double shear timber connections with dowel type fasteners, PhD thesis, Delft University.
- Jorissen, A. & Blass, H. J. (1998), The fastener yield strength in bending, *in* 'CIB/W18 meeting Savonlinna, Finland', Universität Karlsruhe, pp. 31–7–6.
- Larsen, H. J. & Enquist, B. (1996), Glass Fibre Reinforcement of Dowel-Type Joints, *in* V. K. A. Gopu, ed., 'Proceedings of the International Wood Engineering Conference, October 28–31, 1996', Vol. 1, New Orleans, Louisiana, USA, pp. 293–302.
- Larsen, H. J. & Riberholt, H. (1988), *Timber constructions, Design (in Danish)*, number 135, Statens Byggeforskningsinstitut, Hørsholm, Denmark.
- Larsen, H. J. & Riberholt, H. (1991), *Timber constructions, Connections (in Danish)*, number 140, Statens Byggeforskningsinstitut, Hørsholm, Denmark.
- Larsen, H. J. & Riberholt, H. (1999), *Timber constructions, Connections (in Danish)*, number 194, 3 edn, Statens Byggeforskningsinstitut, Hørsholm, Denmark.
- Madsen, B. (2000), *Behaviour of Timber Connections*, 1th edn, Timber Engineering ltd., Vancouver, Canada.

- Mohammad, M. A. H., Quenneville, P. & Smith, I. (1997), Bolted Timber Connections: Investigations on Failure Mechanism, *in* P. Hoffmeyer, ed., ‘Proceedings of the International Conference of IUFRO S 5.02 Timber Engineering, June 18 – 20, 1997’, Copenhagen, Denmark, pp. 211–226.
- Nielsen, T. F. & Johansen, M. (1970), Investigation of Timber Joints with Bolts and Connectors (in Danish), SBI-report 67, Statens Byggeforskningsinstitut, Hørsholm, Denmark.
- O86.1-94 (1994), Engineering design in wood (limit states design), Technical report, Canadian Standards Association, Etobicoke, Ontario, Canada.
- Pedersen, M. U., Clorius, C. O., Damkilde, L. & Hoffmeyer, P. (2000), ‘A Simple Size Effect Model for Tension Perpendicular to the Grain’, *Accepted for publication in: Wood Science and Technology*.
- Pedersen, M. U., Clorius, C. O., Damkilde, L., Hoffmeyer, P. & Traberg, S. (1999), Size Effect in Tension Perpendicular to the Grain, *in* B. Walford, ed., ‘Pacific Timber Engineering Conference, Rotorua, New Zealand March 1999’, Vol. 1, pp. 207–214.
- Sandberg, L. B., Bulleit, W. M. & Reid, E. H. (2000), ‘Strength and stiffness of oak pegs in traditional timber-frame joints’, *Journal of Structural Engineering* **126**(6), 717–723.
- Smith, I. (1993), Dowel-type fasteners: what’s in the pipeline? a canadian view, *in* ‘International workshop on wood connectors’, Forest Products Society, pp. 88–93.
- Van der Put, T. A. C. M. (1990), Tension perpendicular to the grain at nothes and joints, *in* ‘CIB/W18 meeting Lisbon, Portugal’, pp. 23–10–1.
- Whale, L. R. J., Smith, I. & Larsen, H. J. (1987), Design of nailed and bolted joints. Proposals for the revision of existing formulae in draft Eurocode 5 and the CIB code, *in* ‘CIB/W18 meeting Dublin, Ireland’, pp. 20–7–1.

# List of Symbols

- $\eta_0$  Efficiency factor,  $f_{h,0}/f_{t,0}$
- $\eta_{90}$  Efficiency factor,  $f_{h,90}/f_{t,90}$
- $\lambda$  Slenderness ratio (t/d)
- $\lambda_y$  Slenderness ratio at mode III limit
- $\lambda_r$   $\lambda_r = \lambda/\lambda_y$
- $\rho_k$  Characteristic density
- $\rho$  Density. Subscript indicates nominal level of moisture content
- $d$  Dowel diameter
- $E_{c,90R}$  Modulus of elasticity determined in compression at 90° to grain in radial direction
- $E_{c,90T}$  Modulus of elasticity determined in compression at 90° to grain in tangential direction
- $e$  Slot eccentricity relative to hinge
- $F_y$  Capacity per shear plane of a dowel type connection
- $F_y/t$  Capacity per timber thickness of a dowel type connection
- $f_{c,90R}$  Compressive strength at 90° to grain in radial direction
- $f_{c,90T}$  Compressive strength at 90° to grain in tangential direction
- $f_h$  Embedment strength for unspecified angle to grain
- $f_{h,\alpha}$  Embedment strength for angle  $\alpha$  to grain

## List of Symbols

---

$f_{h,u2}$	Embedment strength measured at 2 mm deformation
$f_{h,y5}$	Embedment strength measured after 5 mm yield deformation
$f_{u,steel}$	Tensile strength of dowel steel
$f_{ved}$	Danish for compression strength
$f_{v,RL}$	Shear strength in R direction in L plane
$f_{v,TL}$	Shear strength in T direction in L plane
$f_{y,steel}$	Yield strength of dowel steel
$K_E$	Elastic stiffness
$K_{post}$	Hardening stiffness
$k_{90}$	The ratio $f_{c,90}/f_{c,0}$ including non-linear loaded area modification
$k_{90,EC5}$	Inverse linearisation of $k_{90}$
$k_j$	Fabrication accuracy factor
$k_m$	Reduction factor for multiple rows
$M_y$	Dowel bending moment
$n_{ef}$	Effective number of dowels in a row
$s$	Standard Deviation
$t$	Wood member thickness per side

# List of Abbreviations

*COV* Coefficient of Variation

*COV<sub>model</sub>* Model coefficient of variance

FRP Fibre reinforced plastic

*MOE* Modulus of Elasticity

*RH* Relative humidity

*SL* Stress level relative to ultimate strength

# STRENGTH OF GLUED-IN BOLTS AFTER FULL-SCALE LOADING

By M. Uhre Pedersen,<sup>1</sup> C. O. Clorius,<sup>2</sup> L. Damkilde,<sup>3</sup> and P. Hoffmeyer<sup>4</sup>

**ABSTRACT:** In 1993 after 9 years of use, one of the wooden blades of a windmill was struck by lightning. After demounting, the damaged blade was handed over to the Technical University of Denmark, Lyngby, for the investigation of potential fatigue damage. This paper presents an experimental determination of the residual strength of the glued-in bolts that served as the blade to rotor hub connection in the windmill. The load history of the bolts, the test method, the observed fracture modes, and the force displacement curves are presented along with the recorded residual strength of the bolts. The bolts with a length of 500 mm had a special hollow tapering giving them a higher load-bearing capacity than solid bolts of equal dimensions. An FEM analysis confirms the higher load-bearing capacity. The mean residual strength was found to be 362 kN with a standard deviation of 37 kN, which is 95% of the predicted strength based on short-term tests on similar bolts. At fracture, a displacement between 0.4 and 1.0 mm was observed. In the majority of failures, the bolts were pulled out like a cork from a bottle.

## INTRODUCTION

Glued-in bolts in glulam make stiff and strong connections. Contrary to traditional timber connections, they transfer section forces directly into the inner part of the cross section. Traditional connections act through shear at the surface, which limits their load-bearing capacity and thus restricts the potential of wood structures. Though glued-in bolts have been known since the 1960s, they are only sparsely used, primarily due to the limited knowledge of the long-term strength.

The aim of this paper is to present an experimental assessment of the long-term strength as a function of full-scale loading (i.e., load duration, varying load levels, moisture fluctuations, and low frequency fatigue). The assessment is based on a number of pullout tests performed on glued-in bolts having served for 9 years in a large windmill as connectors between the blade and rotor-hub. A more demanding application of glued-in bolts is difficult to imagine with the forces being reversed at every rotation of the rotor and the blades being exposed to varying weather conditions. The wind and gravity load give mainly bending in the connection, and this results in axial load in the single bolt. The axial load changes between tension and compression during the rotation.

## WOODEN BLADES OF NIBE-B WINDMILL

During the early 1980s a group of Danish glulam manufacturers were inspired by American experience to develop a wooden construction for large aerogenerator rotor blades. This coincided with the desire for an alternative blade technology that could challenge the traditional fiberglass blade manufactures. In 1984 the first full-scale results were obtained as the fiberglass blades of the 20-m-radius rotor of the Nibe-B windmill were replaced by wooden blades by the Danish electricity company ELKRAFT.

The blades were 18 m long and had a solid leading edge of Swedish spruce glulam extending for about 30% of the blade

chord (Fig. 1). The trailing edge was built up with ribs, stringers, and a 7-mm birch plywood coating. The blades were sealed with a 1-mm polyurethane covering allowing some moisture diffusion. The blades had a final weight of 2,500 kg each. The connection between blade and hub was established by 28 glued-in bolts in each root section. The bolts were arranged in a circle with a diameter of 710 mm in the solid root section leaving 30 mm of glulam spacing between the bolts. The cylindrical glulam root section had a diameter of 860 mm, which left 50 mm of glulam from the bolt perimeter to the outer circumference.

Fig. 2 shows the geometry of the hollow tapered bolts. The glued-in length of the bolts was 500 mm and the diameter was 48 mm. The drilled holes in the glulam were 2 mm oversized and a two-component epoxy glue was used to bond the shot-blasted surface of the bolt to the glulam. The glue was prevented from entering the hollow tapering by inserting a wood plug into the end of the bolt. This is seen in Fig. 3 showing a photograph of a glued-in bolt. The bolt has been milled down to one-half.

## BACKGROUND

### Static Strength

The hollow tapered bolt used in the blade to hub connection of the Nibe-B windmill (Fig. 3) was developed at the Tech-

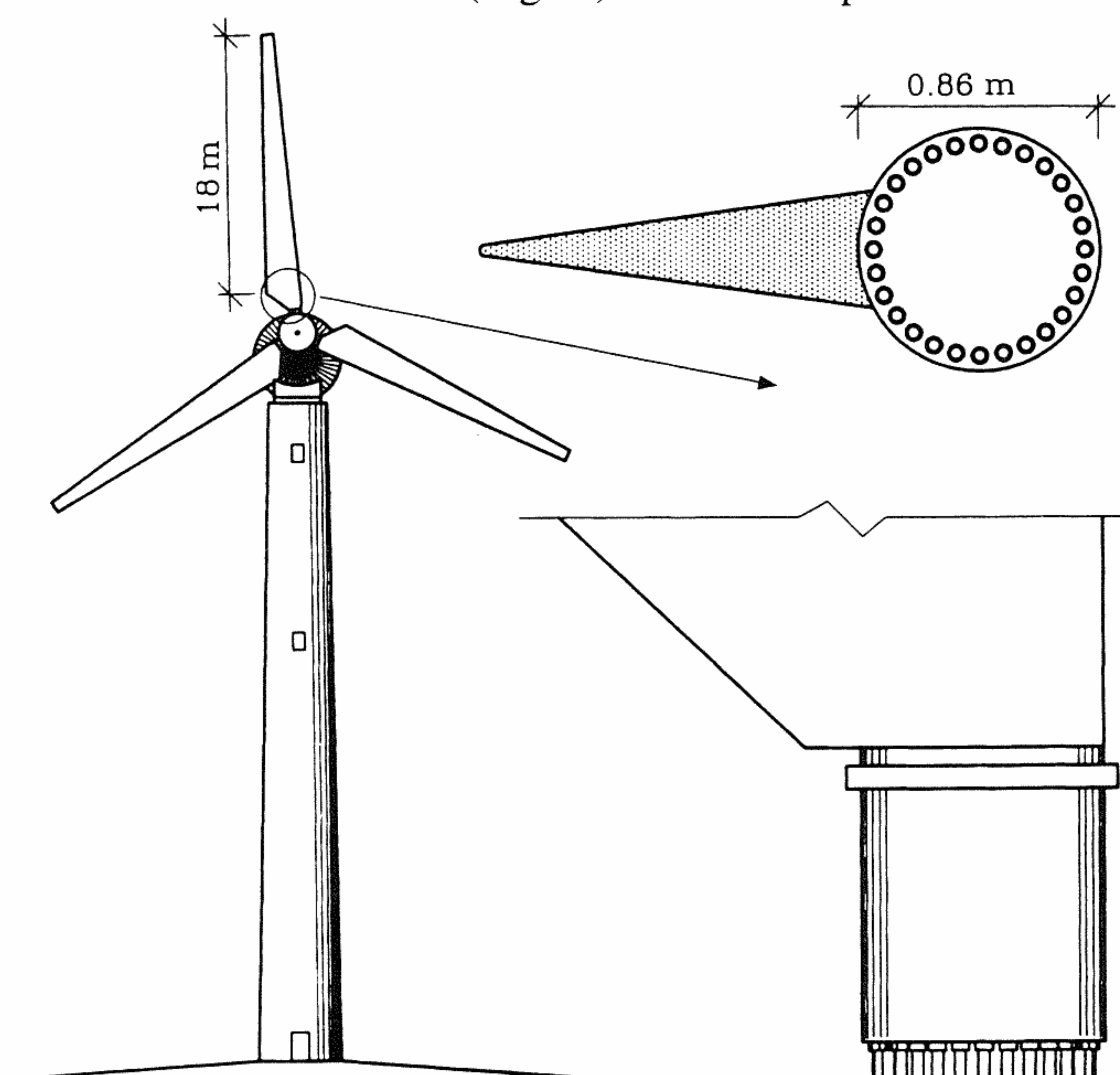


FIG. 1. Nibe-B Windmill with Detail from Blade to Hub Connection

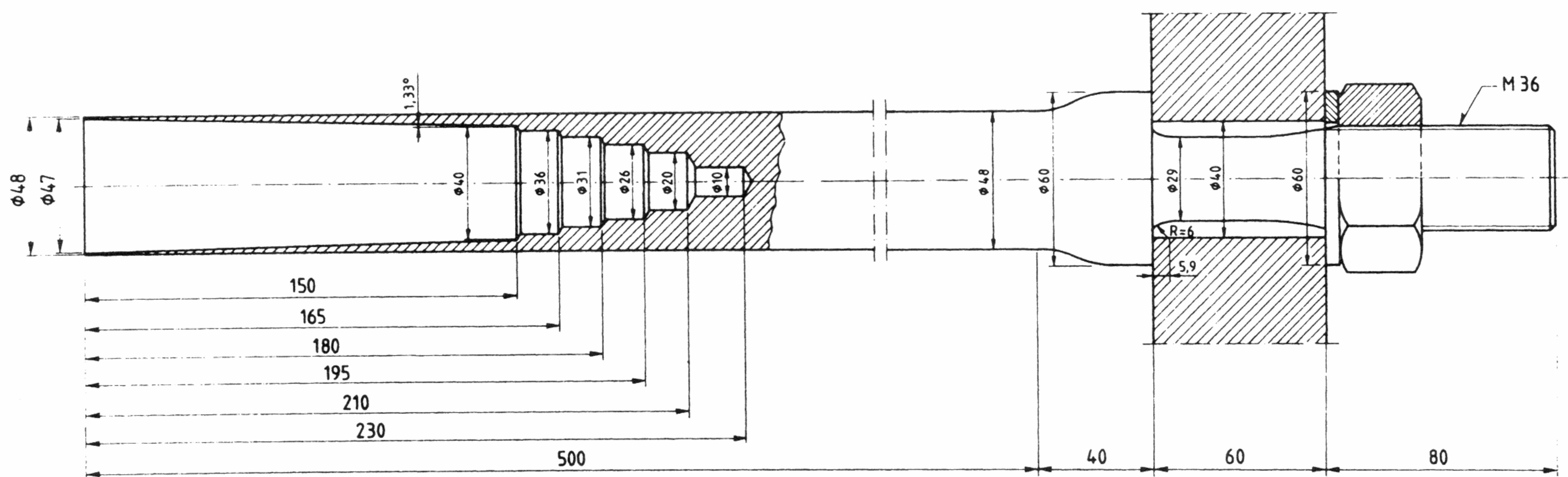
<sup>1</sup>PhD Student, Dept. of Struct. Engrg. and Mat., Tech. Univ. of Denmark, DK-2800 Lyngby, Denmark. E-mail: mup@bkm.dtu.dk

<sup>2</sup>PhD Student, Dept. of Struct. Engrg. and Mat., Tech. Univ. of Denmark, DK-2800 Lyngby, Denmark.

<sup>3</sup>Assoc. Prof., Dept. of Struct. Engrg. and Mat., Tech. Univ. of Denmark, DK-2800 Lyngby, Denmark.

<sup>4</sup>Assoc. Prof., Dept. of Struct. Engrg. and Mat., Tech. Univ. of Denmark, DK-2800 Lyngby, Denmark.

Note. Discussion open until January 1, 2000. To extend the closing date one month, a written request must be filed with the ASCE Manager of Journals. The manuscript for this paper was submitted for review and possible publication on November 11, 1997. This paper is part of the *Journal of Performance of Constructed Facilities*, Vol. 13, No. 3, August, 1999. ©ASCE, ISSN 0887-3828/99/0003-0107-0113/\$8.00 + \$.50 per page. Paper No. 16967.



TEW 34Cr4/BS0

FIG. 2. Geometry of Hollow Tapered Bolts

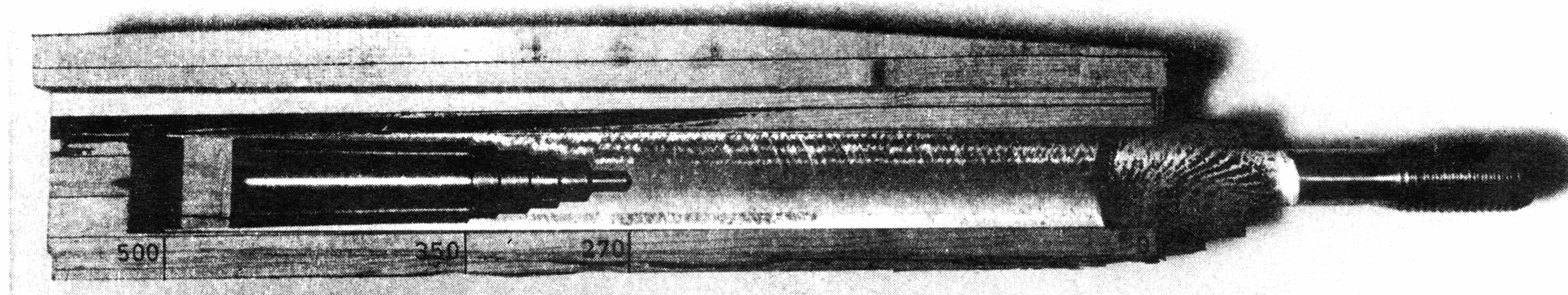


FIG. 3. Sectional View of Hollow Tapered Bolt (Measures in mm)

TABLE 1. Stiffness Parameters used in FEM

Parameter (1)	$E_l$ (GPa) (2)	$E_r$ (MPa) (3)	$G_r$ (MPa) (4)	$\nu_{lr}$ (5)
Wood	14	500	500	0.45
Glue	4	—	—	0.3
Steel	210	—	—	0.2

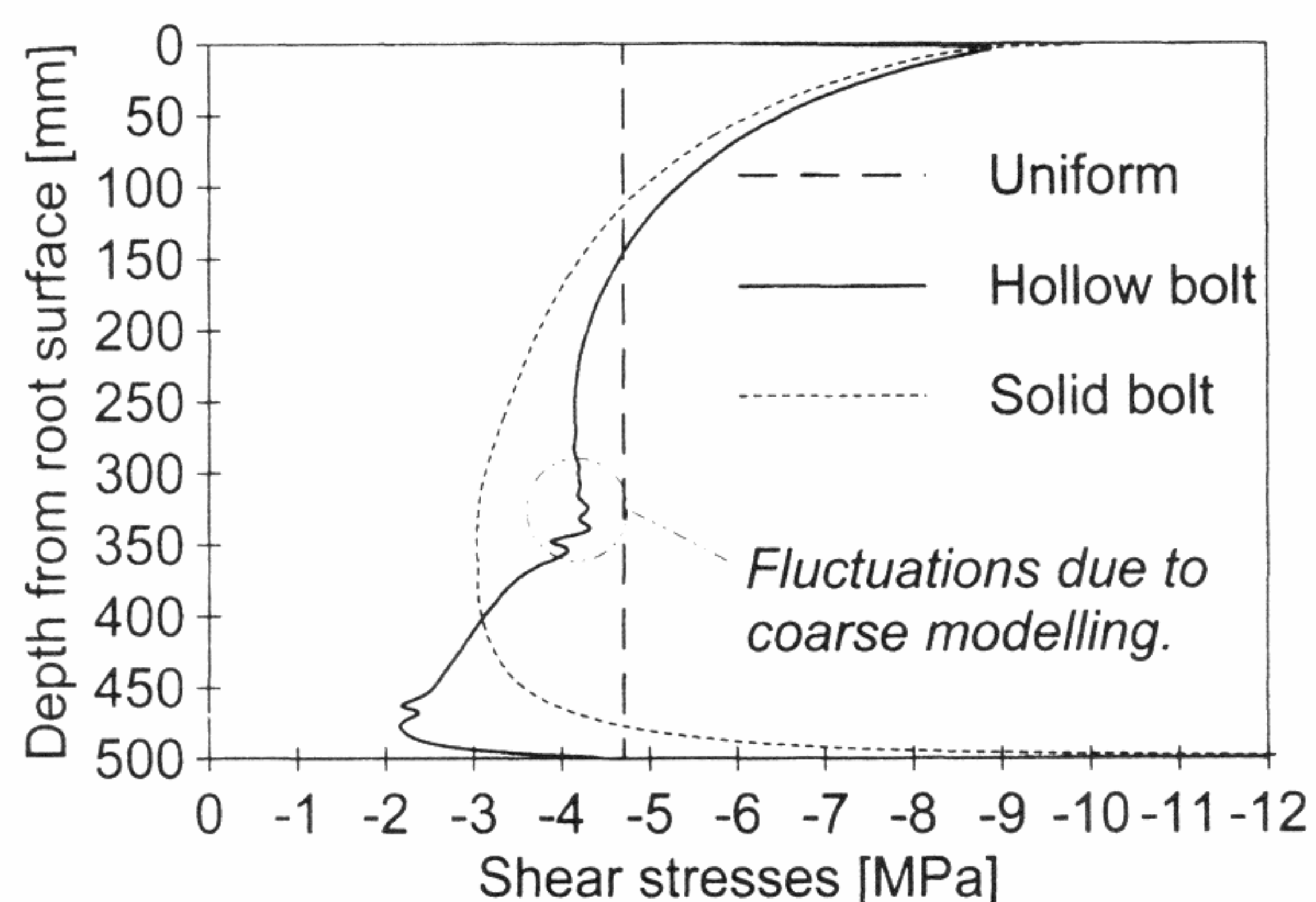


FIG. 4. Shear Stress Distribution along Hollow Tapered Bolt and Solid Bolt, respectively

nical University of Denmark, Lyngby, particularly for this purpose (Riberholt and Spøer 1983). Experimentally, Riberholt and Spøer established that the load-bearing capacity in axial tension is increased 20% by making the bolt hollow. This phenomenon is presumably explained by a stress peak leveling effect of the tapering. An accurate linear elastic finite-element analysis of the shear stress distribution along a glued-in bolt has been performed on solid and hollow tapered bolts. The stiffness parameters used in the rotational symmetrical modeling are given in Table 1. The wood parameters have been determined experimentally.

Fig. 4 shows the shear stress distribution in the middle of

the glue bond. The shear stresses correspond to a bolt force of 360 kN. The following three observations are made:

1. The magnitude of the shear stress peaks at the top and at the bottom end are smaller for the hollowed bolt.
2. The extension of the area with excessive stresses at the end is smaller for the hollowed bolt.
3. The stresses along the hollowed bolt are close to the uniform stress distribution over a larger area.

The first item should not be overemphasized as the peaks represent singularities not adequately evaluated by a linear elastic modeling. A strain softening model such as presented by Johansson et al. (1995) must be invoked to explain the material behavior at these singularities. However, the two last items constitute an explanation to the larger load-bearing capacity observed in the hollowed bolts.

The short term static strength of the hollow tapered bolts can be assessed on the basis of experiments by Riberholt and Spøer (1983). They reported the static strength of hollow tapered bolts to be 346 kN with a standard deviation of 31 kN. Riberholt and Spøer used a tapered geometry similar to the geometry used in the Nibe-B blades; however, the diameter of the Nibe-B bolts is 20% larger. Furthermore, the moisture content (MC) of the surrounding wood was 12.5% on average during testing of the Nibe-B bolts, whereas Riberholt and Spøer reported MC between 9 and 11% in the test specimens. The strength is assumed to be linear in the diameter, and the shear strength of the wood is assumed to decrease 3% for a 0.01 increase in MC. The short-term strength of the Nibe-B bolts is predicted by adjusting the values from Riberholt and Spøer (1983) for size  $k_d$  and moisture  $k_{MC}$

$$k_d = 1.20; \quad k_{MC} = 1 - 2.5 \cdot 0.03 = 0.92$$

The adjusted data predict the virgin static short-term strength,  $F_{static}$ , of the bolts to be

**TABLE 2. Laboratory Fatigue Tests on Glued-In Bolts**

Test (1)	Load range $\{\alpha_1, \alpha_2\}$ (%) (2)	$N$ ( $10^6$ ) (3)
I	{1, 60}	0.33
II	{2, 60}	0.13
III	{1, 60}	0.14
IV	{-20, 20}	12
V	{1, 30}	11
	{-20, 20}	30
VI	{1, 20}	12
	{1, 30}	44

$$F_{static} = k_d \cdot k_{MC} \cdot 346 \text{ kN} = 382 \text{ kN} \quad (1)$$

with a standard deviation of 34 kN.

### Fatigue Performance

Fatigue tests were carried out in the design phase on hollow tapered bolts (Riberholt and Spøer 1983). Six specimens failed in fatigue at a frequency of 8.3 Hz. In Table 2 the number of cycles to failure  $N$  are listed, along with the range of the imposed load level  $\{\alpha_1, \alpha_2\}$ , where

$$\alpha_1 = \frac{F_{fatigue,min}}{F_{static}}, \quad \alpha_2 = \frac{F_{fatigue,max}}{F_{static}} \quad (2a,b)$$

The two last tests quoted in Table 2 were carried out as a combination of two load levels.

The fatigue testing shows that two decades of load cycles are gained when the span of the imposed axial forces is halved. The wooden blades were planned to have a 20-year service life yielding a total of  $2.6 \times 10^8$  load cycles (Øye 1982). For a load variation within 15% of the axial tensile strength, failure is expected after  $10^8$  load cycles by simple extrapolation of the data in Table 2.

### Fatigue Reduction of Static Strength

The fatigue tested specimens (Table 2) contained a glued-in bolt in each end. After fatigue failure of one of the bolts in the test specimen, it was possible to pull out the other bolt in a static tension test. Hence, the fatigue tests gave two kinds of results: (1) The number of load cycles leading to failure for a given load excitation; and (2) the residual strength of the bolt that was exposed to the same load history but had not failed. Treated as a homogeneous entity the residual strength values of the bolts that did not fail in fatigue testing had a mean value of 327 kN with a standard deviation of 22 kN. An insignificant 5% reduction is observed compared with the static short-term strength of similar bolts. An explanation could be that fatigue damage accumulates around the weakest point of the test specimen, leaving the rest of the test specimens uninfluenced by the fatigue load.

### LOAD HISTORY

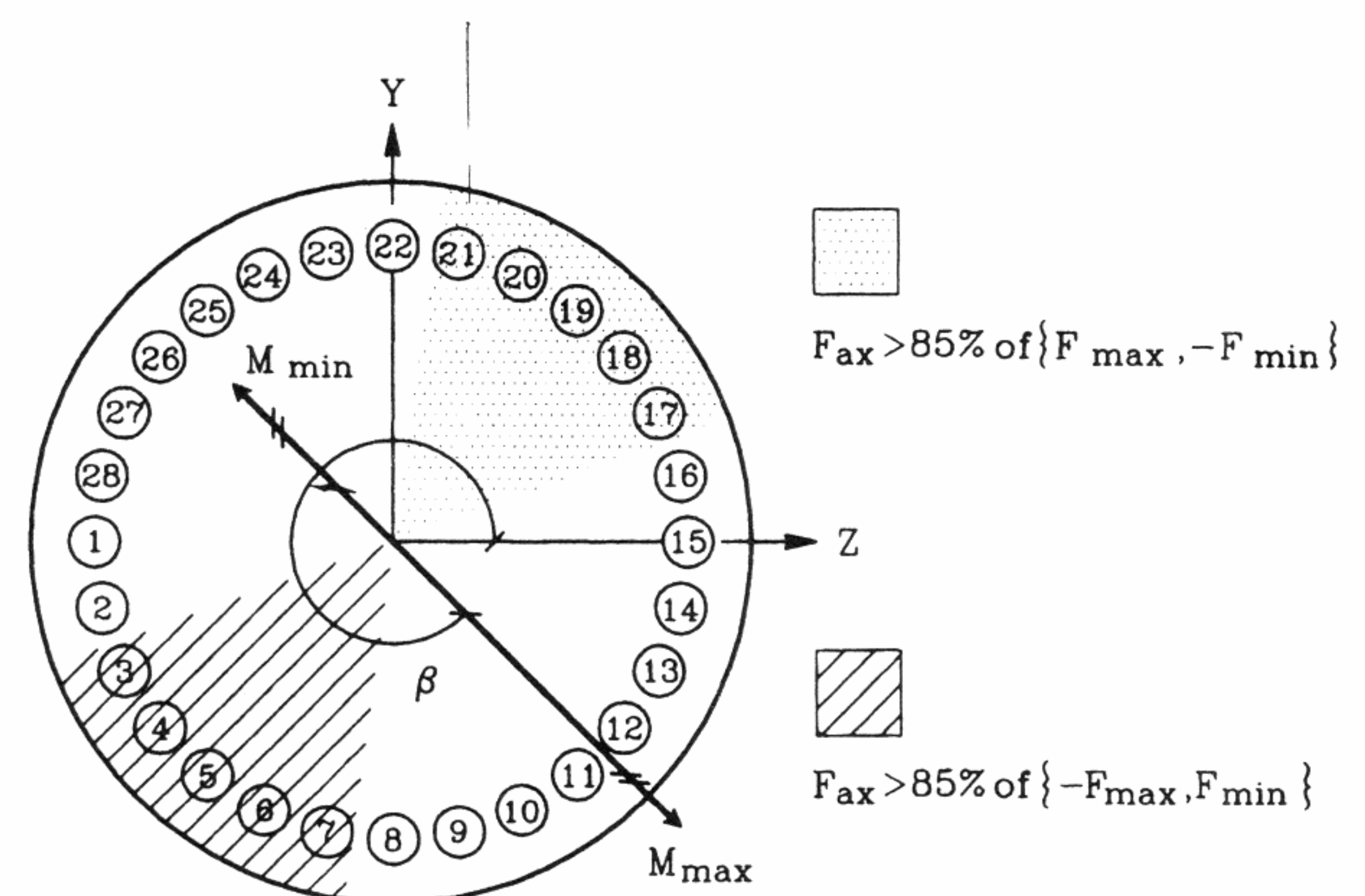
The rotor of the Nibe-B windmill was rigged with wooden blades for 9 years. During that time, the blades were in revolution for  $\sim 3$  years or  $25 \times 10^3$  h (Friis 1984; Rasmussen 1993), with a revolution frequency of 0.55 Hz. In total, the wooden rotor has been exposed to  $50 \times 10^6$  load cycles and an additional 6 years of dead load.

Fig. 5 shows the principle in establishing the load history. The maxima and minima,  $M_{max}$  and  $M_{min}$ , respectively, for the bending moment acting about the severest loaded axis in the connection have been determined as functions of the wind velocity (Øye 1982). The location of the severest loaded axis is given by the angle  $\beta$ . The bending moments were carried by

the bolts as either tension or compression axial forces, denoted as  $\pm F_{max}$  and  $\pm F_{min}$ , respectively. The most severely axially loaded bolts are found perpendicular to the direction of the bending moment. One-third of all bolts are exposed to more than 85% of the largest bolt force.

Limits for the axial forces are listed in Tables 3 and 4 for different wind velocity intervals and in some special situations. The numbers in Fig. 5 and Tables 3 and 4 identify the bolts that experience maximum compression or tension, respectively. The loads obtained during special operation situations are either not dramatically different from the normal loads or they occur in such low numbers that they can be ignored. The majority of load cycles obtained during normal operation is represented in the first six rows of Table 3. The windmill was in a nonoperating state for a total of 6 years. However, the most severe static force does not attain larger values than the forces encountered under dynamic loading, and the most severe forces from both dynamic and static loading act on almost the same bolts.

Fluctuations in MC in the wood are part of the load history of the bolts. Large fluctuation may introduce damage in the wood surrounding the bolt. However, observations of the moisture fluctuations showed that the solid root section had a huge moisture buffer capacity. This buffer capacity and the semidiffusion tight coating secured a relatively constant MC of the wood.

**FIG. 5. Location of Most Severe Load History****TABLE 3. Axial Forces during Normal Operation**

Wind (m/s) (1)	$\beta$ (degrees) (2)	Cycles ( $10^6$ ) (3)	$F_{max}$ (kN) (4)	$F_{min}$ (kN) (5)	Max tension (bolt number) (6)
5-7	355	12.9	19	-17	7-8
7-9	341	12.2	21	-15	6-7
9-11	331	9.8	26	-9	5-6
11-13	308	6.9	44	6	4
13-15	306	4.3	51	9	4
15-17	316	2.3	38	-4	4-5
17-19	322	1.2	33	-10	5
19-21	328	0.6	30	-14	5-6
21-23	331	0.2	31	-16	5-6
23-25	330	0.05	31	-21	5-6

**TABLE 4. Axial Forces during Special Situations**

Condition start/stop (1)	Cycles (2)	$F_{max}$ (kN) (3)	$F_{min}$ (kN) (4)	Max tension (bolt number) (5)
Light wind	18,000	25	-30	4-5
Strong wind	4,500	47	-65	4
Emergency	9	102	-95	3-4
Hurricane	1	106	-77	4-5

## DETERMINATION OF RESIDUAL STRENGTH

The root section of the blades had a solid circular cross section extending for  $\sim 1$  m. The test specimen was cut from the root section of the damaged blade. This produced a 0.8-m-high solid glulam cylinder with a diameter of 0.86 m containing the 28 glued-in bolts.

### Experimental Setup

The saw-cut surface of the test specimen was leveled, made parallel to the plane spanned by the bolts, covered with Teflon film, equipped with a center tap, and finally placed upright on a steel plate. These arrangements made it possible to rotate the test specimen about its center axis. Two steel straps were tightened around the cylinder to counteract tensile stresses perpendicular to the grain introduced during testing. Four steel columns were erected surrounding the test specimen on the strong-floor of the laboratory, and a set of U-profiles were mounted on the columns providing support for the hydraulic equipment as shown in Fig. 6.

The pullout force was delivered by a 500-kN servohydraulic double acting actuator. Due to the high strength of the steel used for the bolts the shaft of the bolts could withstand the necessary forces, and it was possible to pull out a bolt using only a threaded rod and a long socket as the connection between bolt and actuator (Fig. 7). The connection between bolt and actuator allowed for some rotation, and the bolt was accurately positioned under the actuator. Hence, the pullout force

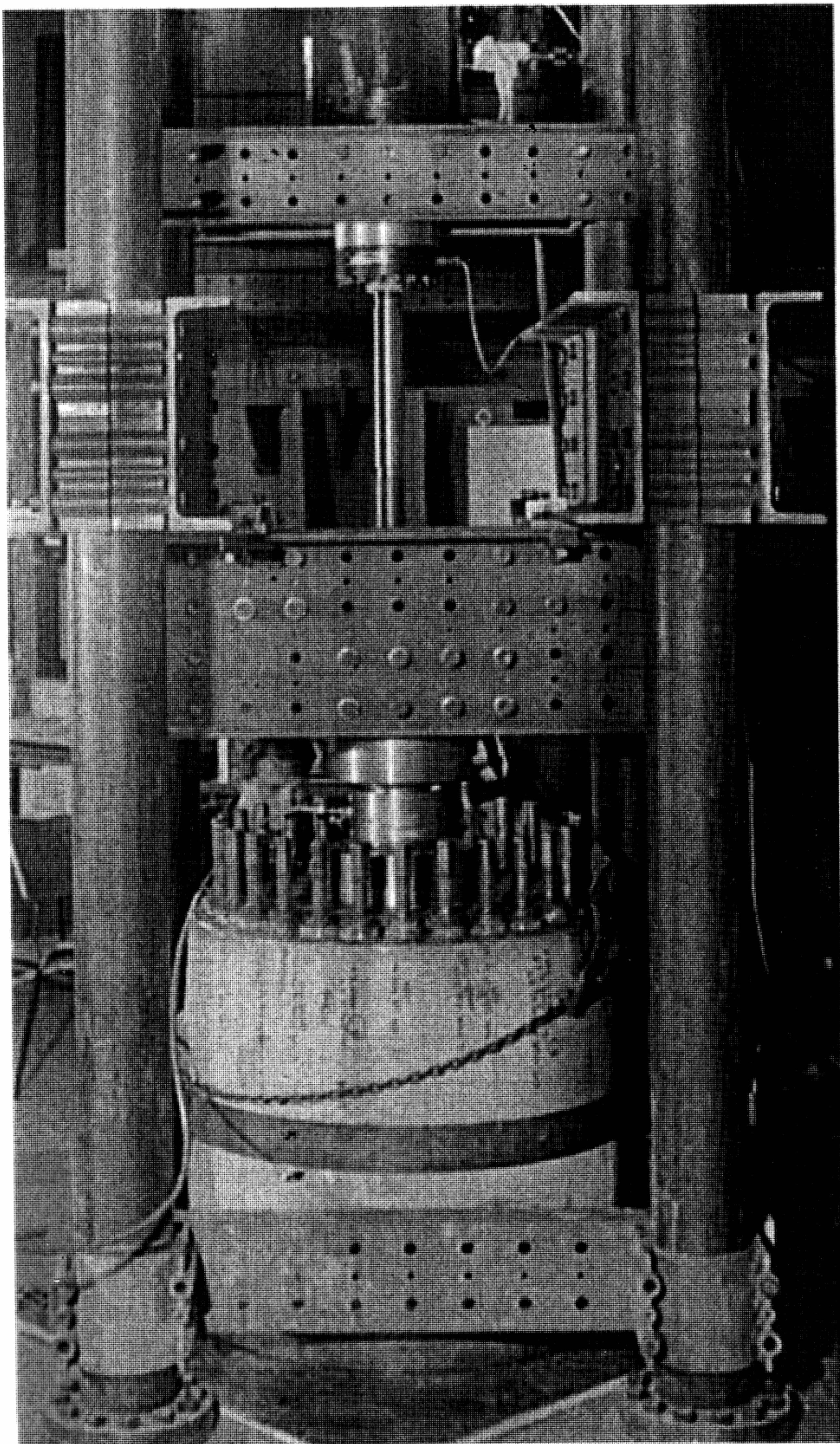


FIG. 6. Test Setup

was a pure axial force. To restrict the wood cylinder from moving during testing, the cylinder was prestressed between the strong-floor and the rigid test setup. The pressure was introduced using an 880-kN Hydrocam hydraulic press and a charnier between a steel beam and a 30-mm steel plate covering the upper surface of the wood cylinder.

### Displacement Monitoring

Displacement of the whole test specimen was measured using three displacement transducers—one acting on the loaded bolt and the other two acting on neighboring bolts (Figure 7). Signals from the displacement transducers and from the load cell of the actuator were recorded every 2 s.

The displacement transducers measured the absolute movements of the loaded bolt and two neighboring nonloaded bolts.

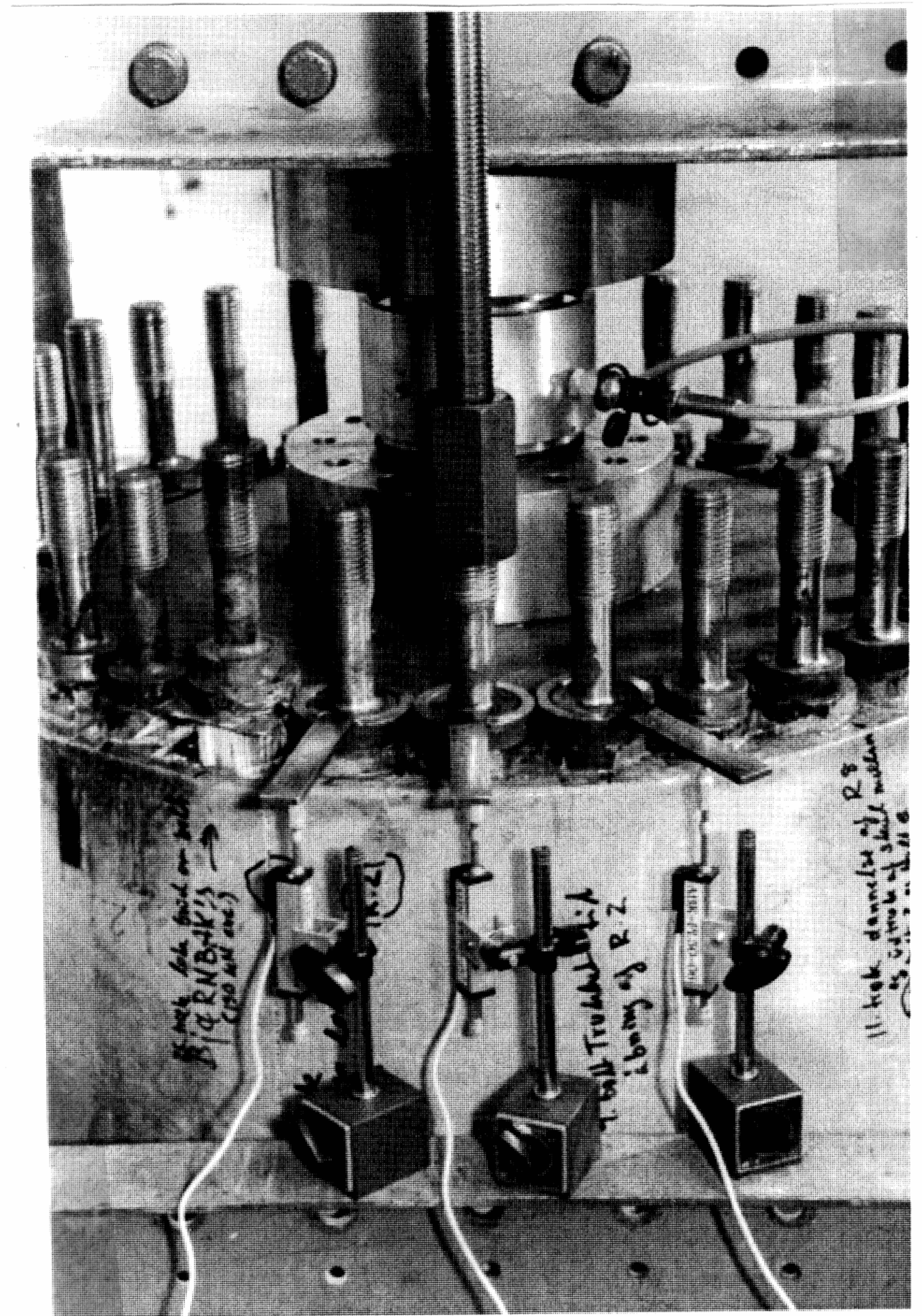


FIG. 7. Setup of Displacement Transducers

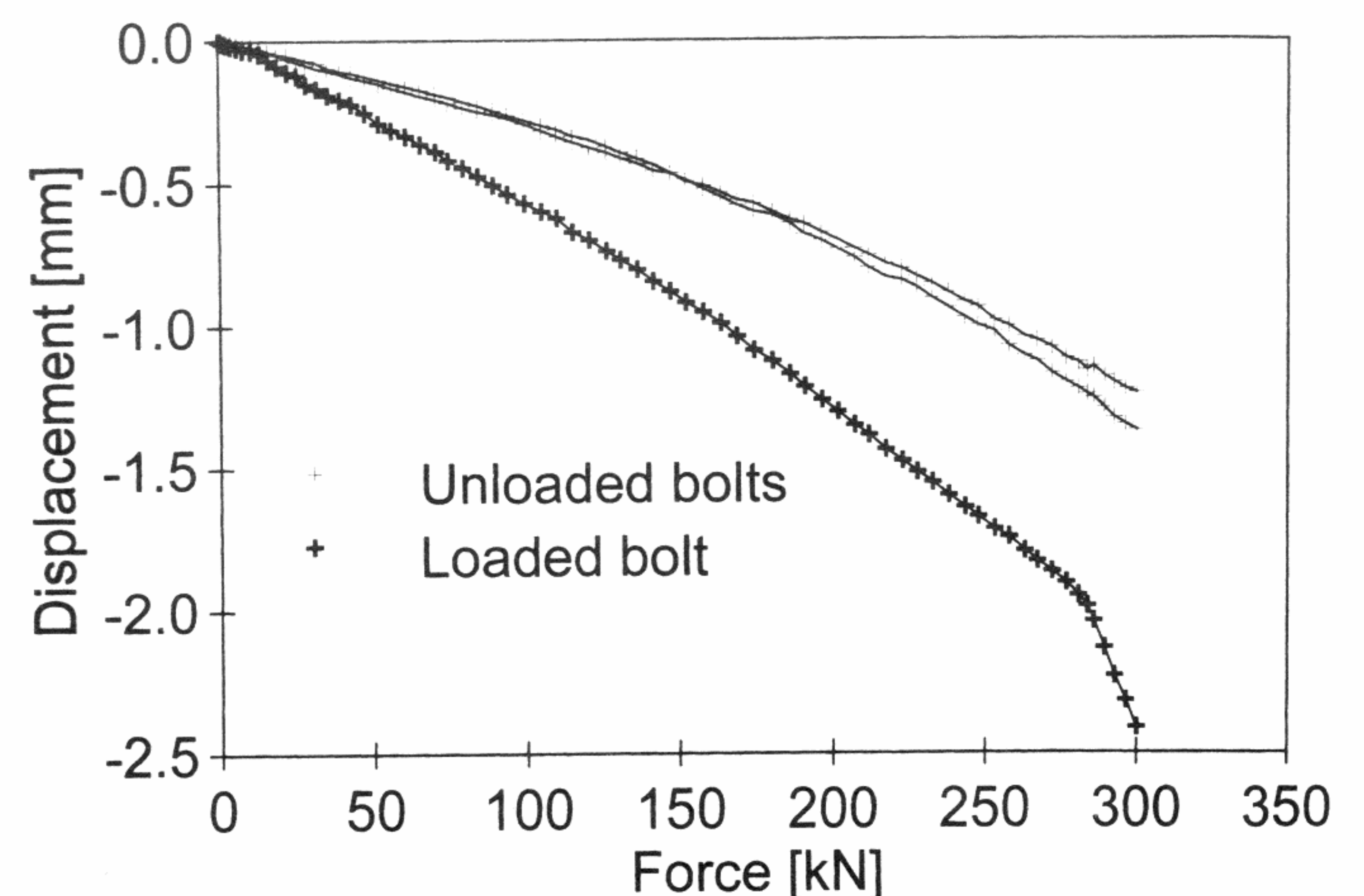


FIG. 8. Absolute Displacements of Three Neighboring Bolts

Fig. 8 shows an example of these displacement measurements. Subtraction of the displacements of the nonloaded bolts from the displacement of the loaded bolt is a measure of the displacement of the loaded bolt relative to the test specimen. This displacement measure is not restricted to the bolt and glue bond; it comprises the displacement of the wood in the proximity of the bolt as well.

Measurements with double instrumentation were made to estimate the uncertainty of the displacement measurements. The uncertainty was found to be one order of magnitude smaller than the displacement of the bolts measured relative to the test specimen.

### Conduction of Tests

The bolts were spaced apart by only 30 mm of glulam, and there was a potential danger of successive progression of fractures if neighboring bolts were tested one after another. Hence, the testing was conducted in the following two series:

- First series of pullout tests bringing every second bolt to failure
- Second series of pullout tests bringing the remaining bolts to failure

The first series of pullout tests form the main results for the entire investigation. The tests were displacement controlled with a 4-min duration of each test. A total of 11 bolts were pulled out in this series. The results obtained in the second test series are of a more informative character as they may be influenced by the first test series. A total of 10 bolts were pulled out in this series.

## RESULTS

### Fracture Modes

In the majority of failures the bolts were pulled out like a cork from a bottle (i.e., a local brittle failure in the proximity of the bolt). Fig. 9 shows typical examples of failed bolts. Seven bolts were never tested as they were pulled off in one piece (Fig. 10). This was because of a drying crack along the inner perimeter of the bolt circle. The failure of a bolt can be described by dividing the fracture location into three categories:

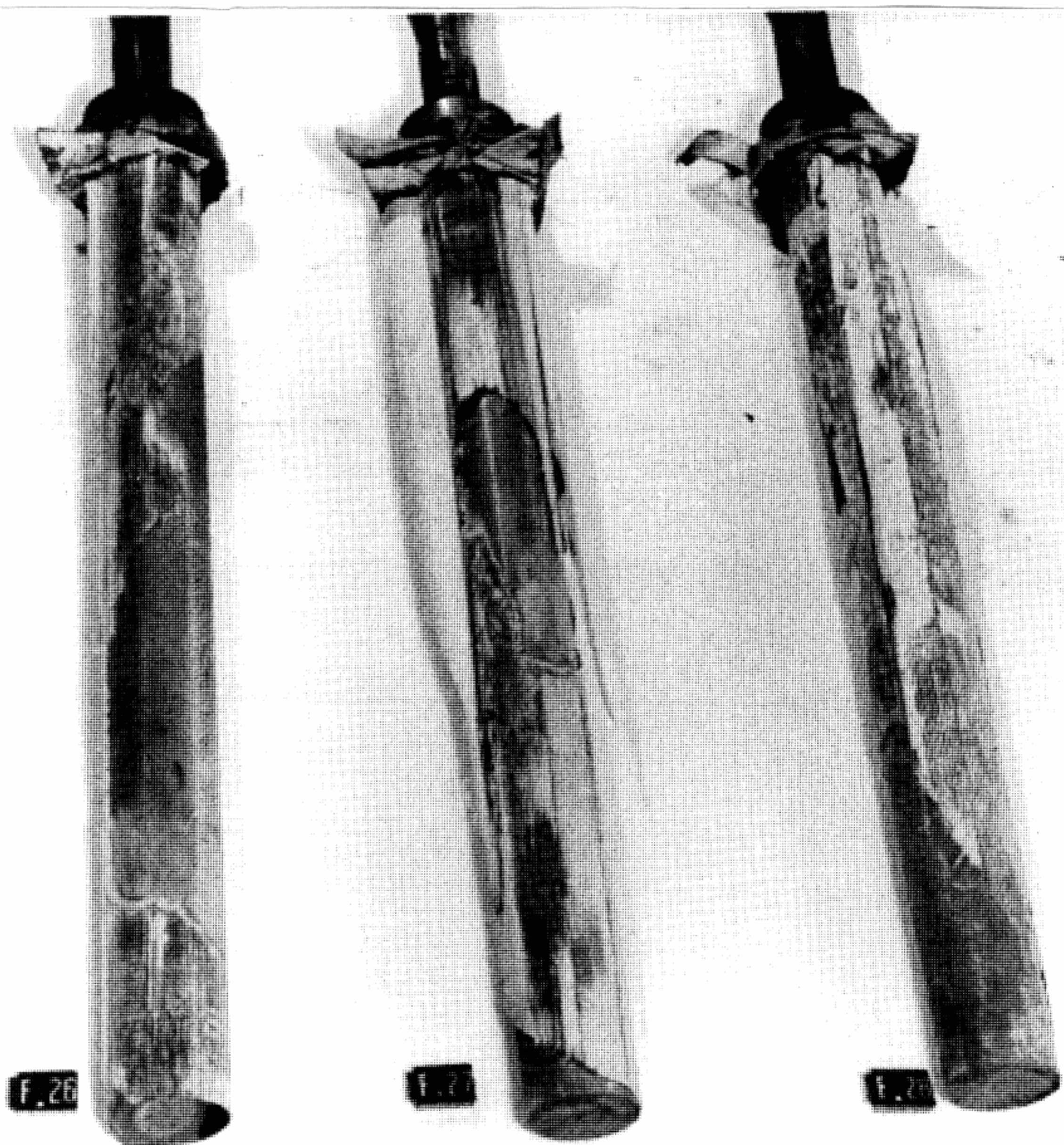


FIG. 9. Failed Bolts

- A—Fracture between bolt and glue
- B—Fracture between glue and glulam
- C—Fracture in wood in the proximity of the bolt

Fractures exposing the bolt surface occurred only in a few cases. The majority of fractures were between the glue and wood or in the wood only. The relative fracture locations are evaluated according to Categories A, B, and C in Table 5.

The bolts pulled out in the first series show the most characteristic “cork from a bottle” mode of failure. Testing and failure of one bolt influence the two neighboring bolts, which is verified by the data in Table 5. The fractures of bolts pulled in the second series tend to be in the wood surrounding the bolt rather than close to the bolt, suggesting that damage of the glulam was introduced during the first series of pullout tests. However, in each series there is no progressive shift from failure Categories A and B toward Category C.

No major flaws in the glue bond were observed on the exposed surface of the failed bolts. Few and small air voids were observed. A bolt, taken from the shell sections that failed in one part, was milled off exposing the sectional view shown in Fig. 3. This revealed slight inclination of the bolt in its hole and few air voids in the glue bond.

### Strength and Stiffness

The pronounced difference in fracture phenomenology for the two series of pullout was also present for the ultimate strength. The first series of tests show a mean strength 20% higher than that obtained for the remaining bolts pulled out between the failed bolts. The results from the second test series are therefore excluded with respect to the determination of the remaining strength of the bolts.

The results of the first series of pullout tests are shown in Table 6. The value of the ultimate strength  $F_{ult}$  is given along with the ultimate displacement  $\delta_{ult}$  of the loaded bolt relative to the test specimen. The mean of the obtained strength values is 362 kN with a standard deviation of 37 kN. The strength of the bolts was not negatively correlated to the progression of tests. This observation is crucial. It makes it reasonable to believe that the values of strength obtained in the first series

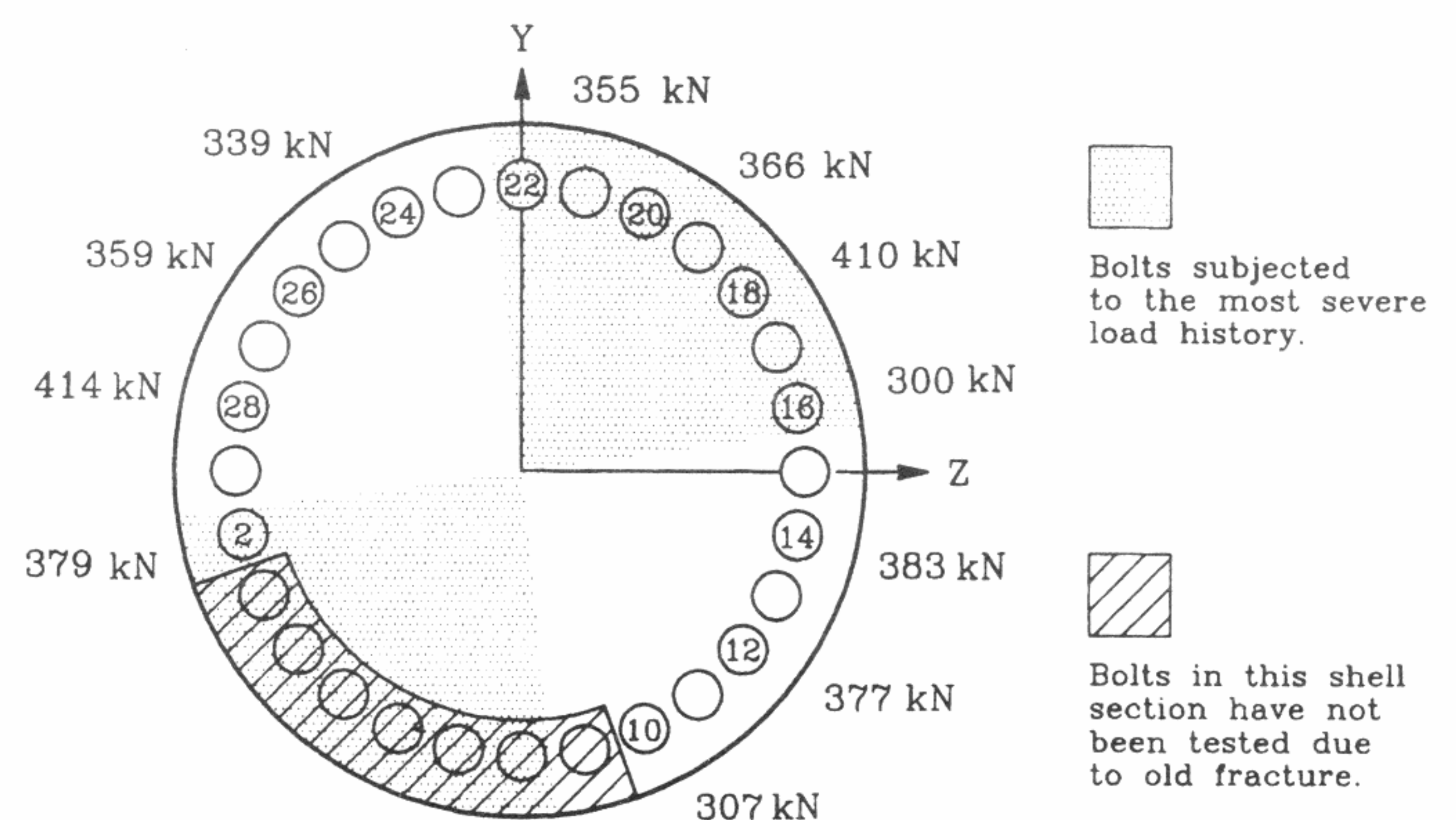


FIG. 10. Load History and Strength of Bolts Taken to Failure in First Test Series

TABLE 5. Fracture Location in Two Test Series

Series <sup>a</sup>	Category		
	A (%)	B (%)	C (%)
(1)	(2)	(3)	(4)
First	14	52	34
Second	2	48	50

<sup>a</sup>Series in which bolts were tested.

**TABLE 6. Results of First Series of Pullout Tests**

Bolt number (1)	$F_{ult}$ (kN) (2)	$\delta_{ult}$ (mm) (3)	$F/\delta$ (kN/mm) (4)	$R^2$ (5)
2	379	0.54	860	0.99
10	307	0.56	512	0.99
12	377	0.81	600	0.92
14	383	0.68	610	0.99
16	300	1.11	351	0.99
18	410	0.80	794	0.89
20	366	0.67	768	0.99
22	355	0.85	425	0.99
24	339	0.67	496	0.99
26	359	0.99	398	0.99
28	414	0.36	1,231	0.98

**TABLE 7. Fatigue Data from Laboratory Tests and Condensed Version of In Situ Load History**

Laboratory Tests—Low Level Fatigue on Three Bolts		In Situ Loading on Most Severely Loaded Bolt	
Load range $\{\alpha_1, \alpha_2\}$ (%) (1)	$N_{failure}$ ( $10^6$ ) (2)	Load range $\{\alpha_1, \alpha_2\}$ (%) (3)	$N_{in\ situ}$ ( $10^6$ ) (4)
{-20, 20}	12	{-5, 5}	13
{1, 30}	11	{-4, 6}	12
{-20, 20}	30	{-2, 7}	10
{1, 20}	12	{2, 12}	7
{1, 30}	44	{2, 14}	4

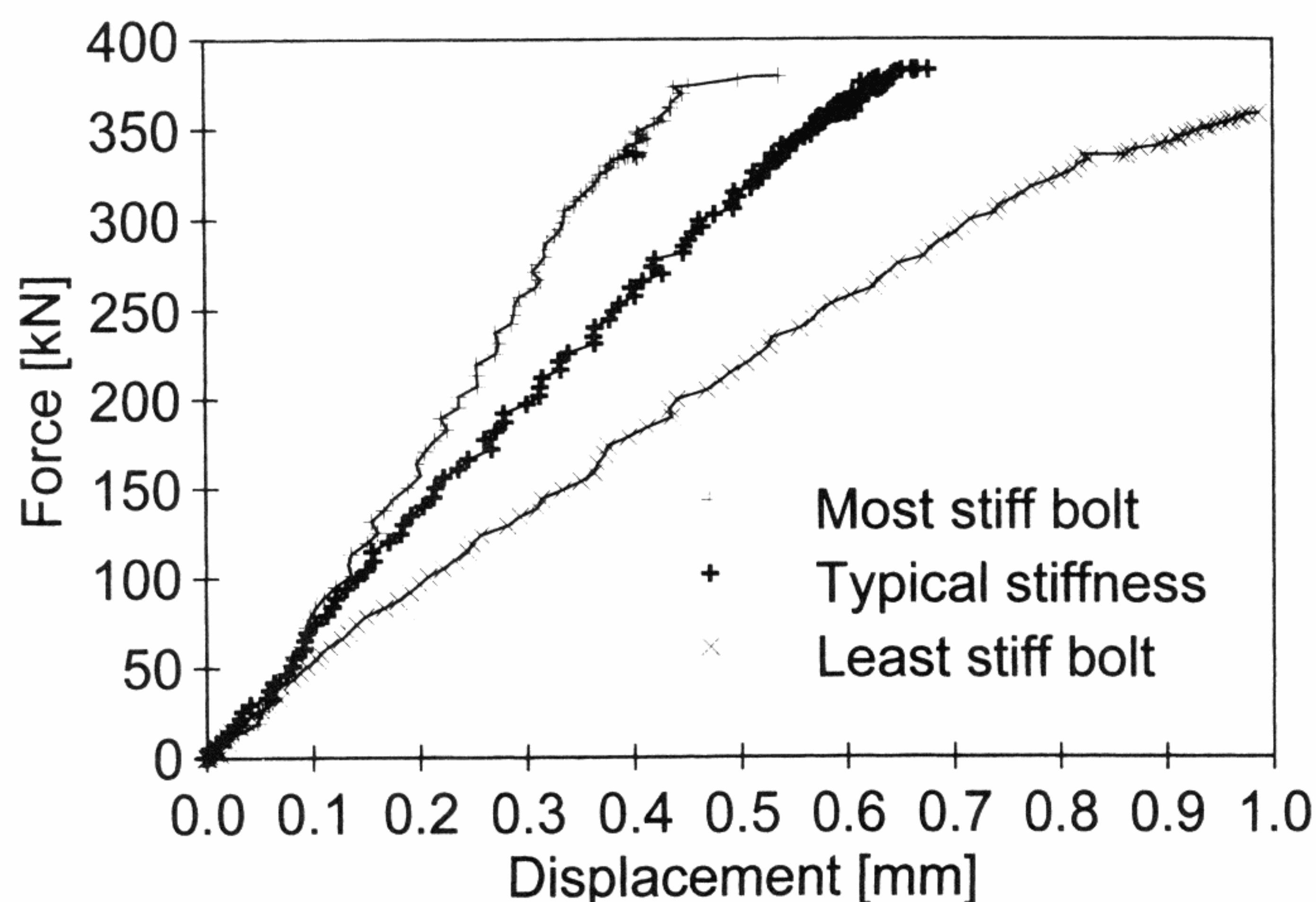


**FIG. 11. Load-Displacement Curves**

of pullout tests were unaffected by the test procedure. Thus, the strength values express the strength of the bolts after 9 years in situ loading. In the second test series the mean of the strength values is 304 kN with a standard deviation of 30 kN. The 20% loss of strength introduced by the testing procedure is distributed surprisingly homogeneously.

The stiffness  $F/\delta$  of the connections, shown in Table 6, has been calculated on basis of the linear part of the load-displacement curves. The coefficients of determination,  $R^2 > 0.98$  in most cases, verify the linearity. In Fig. 11 representative load displacement curves are shown. The curves follow the initial stiffness to failure and show no sign of plastic capacity of the connections.

## DISCUSSION

Based on results from Riberholt and Spøer (1983) the predicted mean value of the virgin static short-term strength is 382 kN with a standard deviation of 34 kN [(1)]. The mean value of the residual strength obtained in the first test series shows a 5% strength reduction compared with this predicted virgin strength of the bolts. The difference in mean strengths can be confirmed at a 73% level of confidence. Although this confirms a difference between the compared mean values, it is important to note that the difference is of the same magnitude as the uncertainty introduced by the adjustment of the static short-term strength [(1)]. Hence, the strength reduction observed is not decisive in a discussion of potential fatigue damage.

The load history of the connection revealed that in terms of axial forces and load span the bolts were not subjected to the same load history. A relatively well-defined group of bolts was exposed to the most severe load history. In Fig. 10 the most severely loaded bolts are accentuated, and the values of

strength obtained in the first series of pullout tests are presented along with the bolt position. The graphical representation reveals no correlation between position and strength (i.e., load history and strength). As the mean strength values of the bolts in the two groups are the same, fatigue damage is not observed by this comparison.

Table 7 quotes data for three low-level laboratory fatigue failures obtained in the design phase (Riberholt and Spøer 1983) along with a condensed version of the fatigue load history of the most severely loaded bolt tested in the present investigation. A linear extrapolation of the laboratory fatigue data into  $10^8$  load cycles—corresponding to 20 years of service life—predicts the safe load range to be below 15% of the static tensile strength. Although the number of load cycles leading to failure in the laboratory fatigue tests is of the same magnitude as for the in situ loaded bolts, the load span is smaller. In a careful comparison, however, the number of cycles must be viewed in the light of the frequency of the load cycles, as a pure number of cycles approach to wood fatigue may be inappropriate due to the time-dependent strength properties of wood.

The frequency used in the laboratory tests (Riberholt and Spøer 1983) was 8.3 Hz, whereas the frequency of the in situ load cycles of the investigated bolts was 0.55 Hz (i.e., 15 times lower). The influence of the frequency of loading on fatigue failure in wood is not well known, but Bach (1975) reported that the number of cycles to failure is a poor measure of fatigue resistance during low frequency pulsation of clear wood. The results presented in Clorius et al. (1996) suggest that a decade of cycles to failure is lost when the frequency is lowered 15 times. If this frequency dependency is also present for glued-in bolts, the number of in situ load cycles quoted in Table 7 corresponds to 10 times as many laboratory loads cycles.

## CONCLUSIONS

A total of 11 glued-in bolts have been pulled out from the root section of the wooden Nibe-B blade. The bolts experienced 9 years in situ load including a total of  $50 \times 10^6$  load cycles, subjecting the bolts to axial loads ranging within 15% of the static short-term strength. The mean value of the residual static strength is 362 kN with a mean displacement at failure of 0.73 mm. An approximate load history has been reconstructed and the virgin short-term strength predicted. The following two observations are made:

1. No difference in residual strength is observed as a function of the load history.
2. The mean strength of the bolts is in accordance with the predicted short-term static strength.

It can be concluded that the bolts investigated maintain full strength after 9 years in situ loading.

## ACKNOWLEDGMENTS

The research was founded by the Danish Ministry of Energy and the Danish electricity company ELKRAFT.

## APPENDIX. REFERENCES

- Bach, L. (1975). "Frequency-dependent fracture in wood under pulsating loading." *Proc., FPRS—Annu. Meeting.*
- Clorius, C. O., Pedersen, M. U., Hoffmeyer, P., and Damkilde, L. (1996). "Fatigue damage in wood." *Proc., 1996 Int. Conf. on Wood Mech.*, 227–248.
- Friis, P. (1984). "Nibe Møllerne, operation status March 1982–October 1983." *EEV. 84-03*, DEFU, Denmark (in Danish).
- Johansson, C.-J., Serrano, E., Gustafsson, P.-J., and Enquist, B. (1995). "Axial strength of glued-in bolts. Calculation model based on non-linear fracture mechanics—A preliminary study." *Proc., CIB/W18 Meeting*, 28-7-9.
- Øye, S. (1982). "Oscillating load calculation, Nibe-B wooden blade." *Notat VK-79-8202051*, DTH, AFM, Denmark (in Danish).
- Rasmussen, B. (1993). "The wooden blade technology, state of the art 1982–1992." *EEV. 93-03*, DEFU, Denmark (in Danish).
- Riberholt, H., and Spøer, P. (1983). "Glued-in bolts for the root to hub connection, Nibe-B windmill." *Tech. Rep. Ser. R No. 167*, Dept. of Struct. Engrg., DTU, Denmark (in Danish).

# A Simple Size Effect Model for Tension Perpendicular to the Grain

M. Uhre Pedersen, C. O. Clorius, L. Damkilde & P. Hoffmeyer

Department of Civil Engineering, Technical University of Denmark. DK-2800 Lyngby

The strength in tension perpendicular to the grain is known to decrease with an increase in the stressed volume. Usually this size effect is explained on a stochastic basis, that is an explanation relying on an increased probability of encountering a strength reducing flaw when the volume of the material under stress is increased. This paper presents an experimental investigation on specimens with well defined structural orientation of the material. The experiments exhibit a large size effect and the nature of the failures encountered suggests that the size effect can be explained on a deterministic basis. Arguments for such a simple deterministic explanation of size effect is found in finite element modelling using the orthotropic stiffness characteristics in the transverse plane of wood.

## 1 Background

Size effect in tension perpendicular to the grain may be approached in one of the following ways:

- Weakest link theory, i.e. a stochastic failure model assuming that failure is determined by Weibull distributed weak elements.
- Damage relevant Weibull stresses, i.e. a stochastic approach taking into account stress peaks introduced by the transverse elastic anisotropy.
- Fracture mechanical size effect, i.e. a model based on the ratio between the release of potential energy and the energy consumption in the fracture process.
- Simple stress criterion on stress peaks introduced by the transverse elastic anisotropy.

### 1.1 Weakest link theory

Size effect in wood is traditionally explained with stochastic arguments that can be summarized as follows:

- Assume that strength reducing flaws are distributed so that the probability of encountering strength higher than  $x$  in a unit volume is  $1 - F(x)$ .
- The number of flaws is proportional to the volume.
- The strength of a given volume of wood is determined by the strength of the weakest spot. This assumption is equal to a brittle failure theory and makes it possible to establish a relation between the strength of a given volume and a chain of  $n$  unit volumes.
- The probability of encountering strength higher than  $x$  in a chain of  $n$  unit volumes is  $[1 - F(x)]^n$ .

One of the solutions to the above extreme value problem is a Weibull distribution, which takes the following form:

$$F_V(x) = 1 - \exp[-\{(x - \epsilon)/\delta\}^k V], \quad (1)$$

where  $k$  is the shape parameter,  $V$  the volume,  $\delta$  is a scale factor and  $\epsilon$  is a lower limit of strength. When  $\epsilon = 0$ , the lower limit of strength is zero and (1) is a 2-parameter Weibull distribution.

The volume in (1) is assumed to be uniformly stressed. The volume dependent strength can be predicted from the strength distribution for a specific volume,  $V_0$ , as the probability of strength values lower than  $x$  at the volume  $V$  is set equal to the known probability  $F_{V_0}(x_0)$ :

$$1 - \exp[-\{x/\delta\}^k V] = 1 - \exp[-\{x_0/\delta\}^k V_0], \quad (2)$$

whereof

$$x = x_0 \left\{ \frac{V_0}{V} \right\}^{\frac{1}{k}} \quad (3)$$

The consequence of (3) is that the strength should decrease with increase in volume. In a double logarithmic diagram the relation is linear with slope  $-1/k$ .

In (Barrett 1974) different experimenters' results on tension perpendicular to grain are explained by use of the weakest link theory. The strength decreases with volume according to (3) and the shape parameter is found to be larger for clear than for commercial material. It is concluded that the strength distribution at constant volume may be due to a parent Weibull distribution. In (Larsen & Riberholt 1981) a size effect for Scandinavian wood is presented. The findings are similar to those in (Barrett 1974) and it is concluded that the strength variation with volume may be described by a parent two parameter Weibull strength distribution with shape parameter of about 5. In (Mistler 1998) a comprehensive investigation of numerous experimental results is presented. It is suggested that volume is replaced by height in the design equations as the strength is found to vary more with specimen height than with specimen volume.

## 1.2 Damage relevant Weibull stresses

In (Ranta-Maunus 1996) it is suggested to use an integration of the tension stress state perpendicular to the grain in order to incorporate the non-uniform stress state introduced by the transverse anisotropy and transient moisture induced stresses in a failure model. The effective stresses, or damage relevant Weibull stresses, are calculated according to:

$$\sigma_{t,90,Wei} = \left( \frac{1}{V} \int_V \sigma_{t,90}^k dV \right)^{\frac{1}{k}} \quad (4)$$

The Weibull stress,  $\sigma_{t,90,Wei}$ , is the value of constant stress that gives the same probability of failure as the actual stress distribution. In (4)  $k$  is the shape parameter of the Weibull distribution. The idea of damage relevant stresses is to weigh local stress peaks according to the Weibull theory.

The non-uniform stress state introduced by the anisotropy is reported in (Hanhijärvi & Ranta-Maunus 1996) and (Castéra & Lac 1997) and the approach using damage relevant Weibull stresses as given in (4) is used in e.g. (Aicher, Dill-Langer & Ranta-Maunus 1998) with the modification that the integral over the stressed volume is replaced with an integral along a line.

## 1.3 Fracture mechanical size effect

Decreasing nominal strength,  $\sigma_N$ , for increased structural size can be explained both within linear and non-linear fracture mechanics. An approximate non-linear size effect model (5) is offered by Bažant & Pfeiffer (1987) and used in (Aicher & Reinhardt 1993, Aicher, Reinhardt & Klöck 1993) to model experiments on single edge notched wood specimens.

$$\sigma_N = B f_t \sqrt{1 + \frac{d}{D_0}}, \quad (5)$$

where  $\sigma_N$  is the nominal strength,  $B$  is an empirical constant depending on the geometry of the test specimen,  $f_t$  is tension strength in a pure strength failure criterion,  $d$  is a typical specimen dimension and  $D_0$  is an empirical constant containing the length of the fracture process zone. The ratio  $d/D_0$  expresses the brittleness of the specimen, for low values of the ratio the specimen fails according to a strength failure criterion and for high values the nominal strength is proportional to  $d^{-\frac{1}{2}}$  as in linear elastic fracture mechanics. For intermediate values the softening properties governs the relation between nominal strength and size.

## 1.4 Simple maximum stress failure criterion

The model using damage relevant Weibull stresses incorporates stress peaks due to material anisotropy in a stochastic failure model. However, a simple maximum stress failure criterion uses the stress peaks

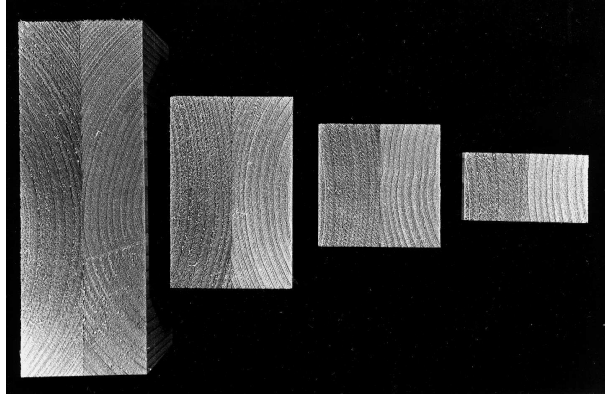


Figure 1: *Endview of specimens showing the intended double symmetry.*

directly in a stress failure model. The occurrence of stress peaks is due to cylindrical orthotropic material stiffness and in case of glulam also the regular pattern of lamination. This stiffness distribution gives rise to stress concentrations which may increase with increase in specimen size and hence give rise to a deterministic size effect. The simple maximum stress criterion states that the nominal strength is a function of stiffness orthotropy, geometry and an inherent material strength,  $f_{t,90}$ :

$$\sigma_N = f(\textit{stiffness orthotropy, geometry, } f_{t,90}) \quad (6)$$

The experimental observations and FEM-modelling presented in the present investigation lend themselves to a such simple stress failure criterion.

## 2 Experiments

### 2.1 Specimens

The clear wood material is taken from a large population of boards of Norwegian grown spruce, *Picea abies*. The boards were subdivided into three groups using an annual ring width criterion. In each group the boards were paired and glued sapwood to sapwood forming planks with symmetrical cross sections. Three planks, one from each annual ring width group, were chosen for the size effect investigation. After conditioning to 65% RH, 22° C, the planks were planed to 45 x 130 mm and cut to lengths of 70 mm avoiding knots and other visible flaws. Twelve clear specimens with a base of 70 x 45 mm and a height of 130 mm were taken from each plank. In random order these were shortened to heights of 25, 45, 70, 130 mm giving four groups of specimens with double symmetry, Figure 1. The base of the specimens was glued to a 20 mm thick aluminium plate using an epoxy glue. The plate had a groove for fixation in the test machine, Figure 2. In order to prevent failure in the wood-aluminium interface the specimens

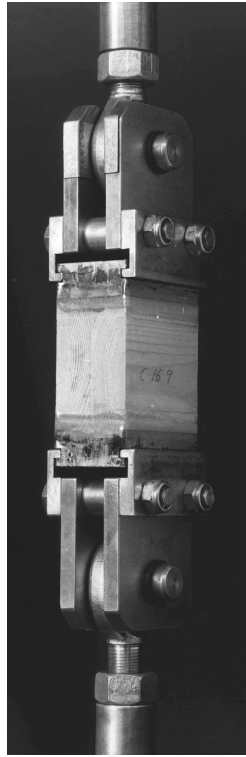


Figure 2: *A 70 mm high specimen mounted in the test machine.*

were locally reinforced with a thin strip of glass fibre in epoxy wrapped about the specimens along the interface.

The clear wood specimens are designed to be used in a fatigue test program providing information about the fatigue strength of wood in tension perpendicular to the grain. The specimen design secures failure at the free length of the specimen in a radial plane as shown in Figures 3 and 4. The design gives a lower bound estimate of the material strength as the tangential strength is smaller than the radial strength.

LVL specimens with a base of 70 x 45 mm were cut in random order from an LVL beam producing specimens with heights in the transverse direction of 25, 45, 112 and 230 mm. Six specimens at each height were tested in tension perpendicular to the grain in the same way as the clear wood specimens.

## 2.2 Tests

Both clear wood specimens and LVL specimens were taken to tension failure perpendicular to the grain in a 100 kN servo hydraulic Instron test machine. The load was applied in a double charnier set up, Figure 2. The tests were load controlled with a load application rate of 0.026 MPa/s giving mean times to failure of 100 seconds.

Height [mm]	Strength [MPa]									Mean	Stdev.
	Series A			Series B			Series C				
25	3.40	3.23	3.03	3.94	3.21	3.61	2.93	3.98	4.05	3.49	0.43
45	2.48	2.57	2.09	2.62	2.65	2.92	3.02	2.86	3.00	2.69	0.30
70	1.79	1.96	1.55	2.19	2.44	2.54	1.68	1.98	2.86	2.11	0.43
130	1.48	1.45	1.27	1.73	1.75	2.02	1.57	1.52	1.82	1.62	0.23
Mean	2.19			2.64			2.61				
$\rho$ [kg/m <sup>3</sup> ]	418			460			479				

Table 1: *Strength values and density for three series of clear wood specimens.*

To get an estimate of the strength in the radial direction each of the 45 mm high specimens were matched with a specimen rotated 90° and tested in tension in the radial direction.

The stiffness in the radial and tangential direction of the clear wood has been determined in a test series comprising 43 specimens with dimensions 20 x 20 x 20 mm. Material from both boards in all three planks was used. The stiffnesses were determined in compression.

### 3 Test Results

#### 3.1 Clear wood tests

The strength values for the four different specimen heights within each of the three series are presented in Table 1. The strength is seen to decrease more than 50% when specimen height is increased approximately 5 times. The material presented covers three test series A, B and C. Specimens within a series originate from the same plank forming a unity with respect to density and other inherent properties, hence each series constitutes a statistical block. The strength variation between series is reflected in the mean density,  $\rho$ , at 65% RH, Table 1.

##### 3.1.1 Failure location

Independent of specimen height all specimens fail in mid section planes as shown in Figure 3. Due to the specimen design the mid section of the specimens form a radial plane, Figure 4.

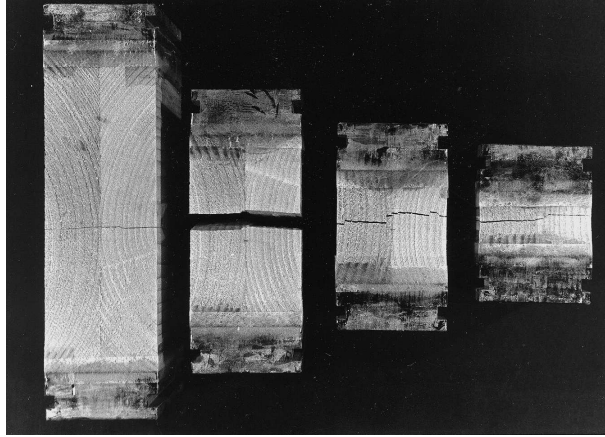


Figure 3: *All specimens fail in mid section radial planes.*

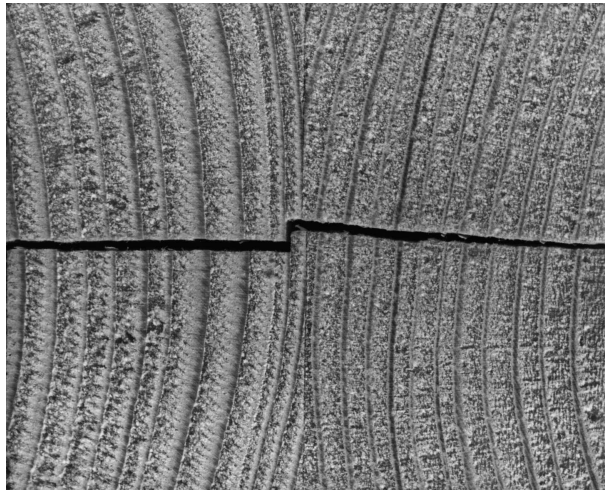


Figure 4: *Close-up of failure zone.*

Stress direction	Mean strength	Stdev.	Mean stiffness	Stdev.
Tangential	2.7	0.3	637	175
Radial	3.3	1.1	851	213

Table 2: *Strength and stiffness in tangential and radial directions, [MPa].*

Height [mm]	Strength [MPa]						Mean	Stdev.
25	1.82	1.86	1.85	1.61	1.42	1.89	1.74	0.19
45	1.47	1.50	1.43	1.61	1.52	1.48	1.50	0.06
112	1.39	1.57	1.50	1.55	1.18	1.60	1.46	0.16
230	1.30	1.46	1.75	1.48	1.44	1.32	1.46	0.16

Table 3: *Strength values for LVL specimens.*

### 3.1.2 Radial and tangential strength and stiffness

The consistent failure location is a result of the difference in strength in radial versus tangential direction. Table 2 lists the tension strength results from tests in radial and tangential direction. The stiffness determination from small oriented compressive tests is also given. As seen from Table 2 the strength in the radial direction is approximately 20% higher than the strength in the tangential direction. Most of the failures in the radial directions were in or initiated in the glue line. However, significantly higher strength were obtained for failure outside the glue line indicating that the radial strength is even higher than apparent from Table 2.

## 3.2 LVL tests

The material used for the LVL specimens have a mean density of  $504 \text{ kg/m}^3$  at 65% RH. Table 3 shows strength values for all tested specimens. No major change in strength as function of height is observed. No systematic failure location was observed.

## 4 Finite element modelling

A plane finite element modelling of the specimens is used to model the stress distribution as function of specimen height and the influence of differences in tangential and radial stiffnesses. The stiffnesses are given in polar coordinates according to Figure 5. The origo for the polar coordinates lies in the pith which has been determined to lie 85 mm from the centre of the specimens as a mean for all six boards involved. With reference to the experimental values in Table 2,  $E_r$  and  $E_t$  are chosen to 900 MPa and

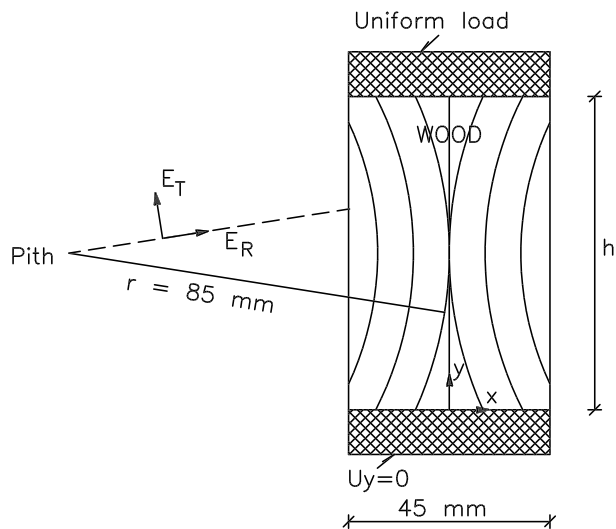


Figure 5: *Specifications for FE modelling.*

600 MPa respectively. Hearmon (1948) here quoted from (Kollmann & Côté 1984) reports a value of  $G_{rt}$  of 30 MPa for equivalent values of  $E_r$  and  $E_t$ . Poissons ratio,  $\nu_{rt}$ , is set to 0.3.

Eight node isoparametric elements in plane stress are used. The specimen is meshed with 22 elements in the x-direction and 100 elements in the y-direction. A uniform load is applied to an aluminium plate similar to the experimental setup. The boundary conditions are given in Figure 5.

#### 4.1 Results of FEM modelling

The differences in stiffness in tangential and radial direction leads to an inhomogeneous stress distribution. Figure 6 shows a contour plot of the tangential stress,  $\sigma_t$ , for a 130 mm high specimen. The stress peak at the corner of the specimen is due to the restriction of transverse deformation introduced by the stiff aluminium plate. In practice failure initiated by this peak was prevented by the described reinforcement of the glue line interface.

Failure is located in the mid section where the stress distribution depends on the test specimen height and the cylindrical orthotropy. For a very short specimen the influence from the cylindrical orthotropy is less pronounced and the stress distribution converges towards a homogeneous distribution. Conversely, the higher the specimen the more pronounced is the inhomogeneous stress distribution generated by the stiffness difference in radial and tangential directions. The distribution of tangential stresses plotted in Figure 7 is the outcome of a modelling with stiffness parameters as given in Section 4. The ratio between  $E_r$  and  $E_t$  is chosen as 1.5; in the literature the ratio is often set to 2. Generally an increase in this ratio will augment the difference between stress distribution for the four specimen heights. The ability

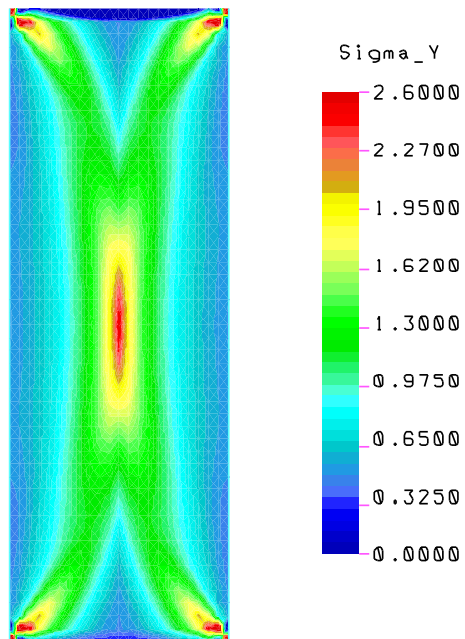


Figure 6: Contour plot of tangential stresses in 130 mm specimen for an applied uniform external stress of 1 MPa, stress in aluminium interface not shown.

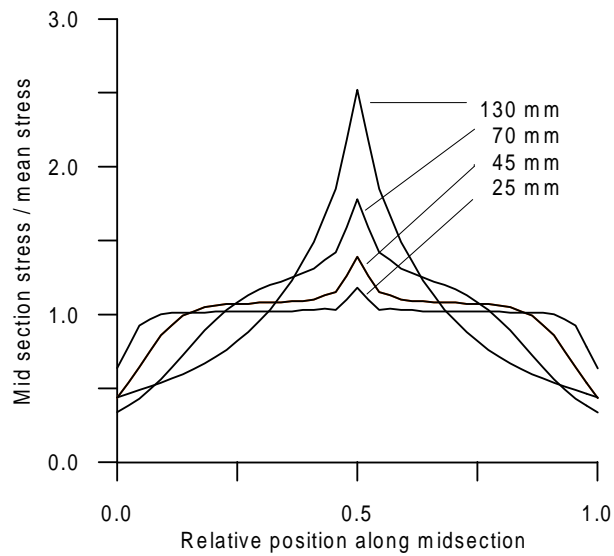


Figure 7: Plot of tangential stresses along the mid section for the different specimen heights.

to generate an inhomogeneous distribution is also dependent on the magnitude of the shear modulus; the general observation is that an increase of shear modulus will reduce the effect of the ratio between  $E_r$  and  $E_t$ .

## 5 Discussion

### 5.1 Statistical treatment of results

The strength of the clear wood specimens decreases with specimen height, whereas the influence of density difference between planks is reflected in the increase in mean strength from series A to C. Strength values and density are shown in Table 1. A linear two-factor statistical model is used to analyse the strength response,  $Y_{ijk}$ , as the sum of overall mean,  $\mu$ , effect of plank,  $p_i$ , effect of height,  $h_j$ , and random error of the individual specimen,  $E_{ijk}$ :

$$Y_{ijk} = \mu + p_i + h_j + E_{ijk} \quad (7)$$

Both  $p_i$  and  $h_j$  are significant with levels of confidence in excess of 99.9%. A Newman-Keuls test on the differences between the effects of height shows that  $h_1 \neq h_2 \neq h_3 \neq h_4$  at a level of confidence higher than 99%.

The analysis implies that the data is normally distributed. This assumption is confirmed by a normal probability test on the residuals,  $E_{ijk}$ , from the analysis. The data proves to fit slightly better to a log-normal distribution,  $X_{ijk} = \log Y_{ijk}$ . However, this transformation has little practical implication as the strength response  $Y_{ijk}$  covers a relatively narrow range. In Figure 8 (a) the strength values given in Table 1 are shown as function of specimen height in a double logarithmic diagram. The data has been cleaned for the scatter between series introduced by the effect of plank, i.e. the corrected values  $Y_{jk} = Y_{ijk} - p_i$  are plotted against height. The graphs show that a linear correlation in a double logarithmic plot provides a good empirical fit to the data.

The LVL specimens do not show a consistent strength variation with height. Though the higher strength of the 25 mm high specimens is statistically significant there is no significant trend in the data, Figure 8 (b).

### 5.2 Modelling

#### 5.2.1 Weibull weakest link

According to the Weibull weakest link theory the probability of encountering a weak spot is increased with increased volume. However, independent of specimen height, all clear wood specimens fail in the

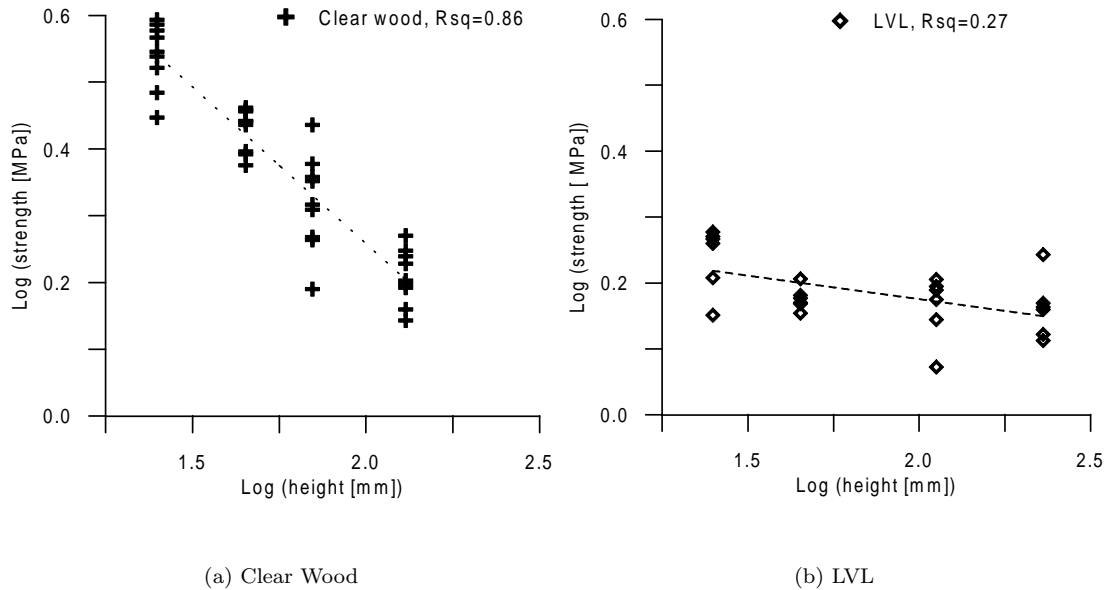


Figure 8:  $\text{Log}(\text{strength})$  versus  $\text{log}(\text{height})$ .

mid section radial plane as shown in Figure 3. The consequence of this deterministic failure location is that the strength cannot depend on the strength distribution in the material outside the failure zone. As the mid section radial plane is the weakest, the strength distribution outside this zone is of no importance to the strength of the specimen, and the strength decrease with increased volume cannot be explained by the Weibull theory. Furthermore, the LVL specimens show practically no strength variation with volume in the investigated range, even though LVL is a prime example of a Weibull material as it is full of strength reducing flaws. In Figure 9 the mean strength for both clear wood and LVL specimens are plotted together with results from (Larsen & Riberholt 1981). Larsen & Riberholt (1981) find a slope of approximately  $-0.2$  corresponding to a shape parameter  $k = 5$  in the Weibull distribution. This is the commonly recognized value of  $k$  also reported in (Barrett 1974) for commercial timber, and used in (EC5-1 1995). The clear wood specimens follow a different trend as the slope of the results is approximately  $-0.5$ . If the size effect observed for clear wood specimens was governed by a weakest link phenomenon this would correspond to the shape parameter  $k = 2$ . A Weibull distribution with shape parameter  $k = 2$  has a larger variance than a distribution with  $k = 5$  as the distribution contracts for higher values of the shape parameter. However, in this investigation the coefficient of variation is of the same order as in e.g. (Larsen & Riberholt 1981), namely 10% to 30%.

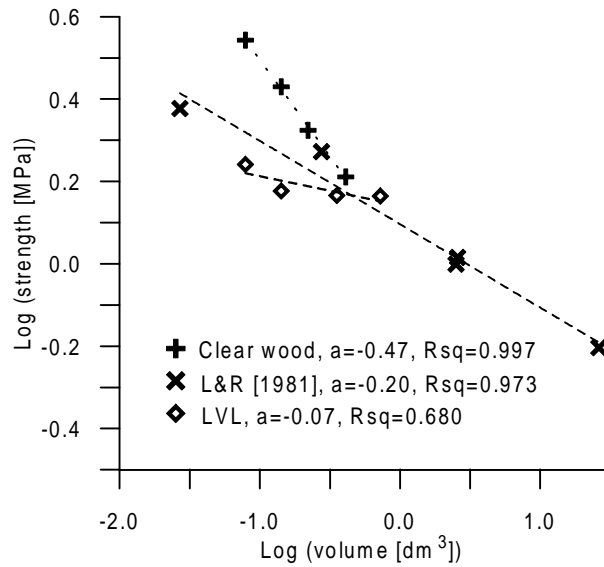


Figure 9: Mean values from this investigation and mean values from (Larsen & Riberholt 1981).

### 5.2.2 Damage relevant Weibull stresses

The concept of Weibull damage relevant stresses is appealing as it offers a means of taking into account non-uniform stress state in a volume where the strength at uniform stress is Weibull distributed.

When the non-uniform stress state is generated by external factors such as specimen geometry or loading configuration, correction to the effective volume is clearly necessary. Stress peaks in a necked tension specimen or in a simple bending specimen where the ultimate strength is governed by tension perpendicular to the grain are less harmful as they cover a limited volume. Corrections for such non-uniform stress distribution have been made in (Barrett 1974) by use of the same principle as given in (4).

Interaction between the Weibull strength distribution and non-uniform stress distribution is easily understood when the non-uniform stress is due to external factors. However, in (Ranta-Maunus 1996) the suggestion is to use (4) to include stress peaks generated by internal factors, i.e. the stiffness distribution. The authors see two problems connected to the concept of damage relevant Weibull stresses:

- The damage relevant Weibull stresses use a deterministic determination of stress distribution due to internal stiffness distribution. This stress distribution is then used in a stochastic model which originally tacitly included the same non-uniform stress distribution as a stochastic phenomenon.
- The shape parameter used in the damage relevant Weibull stress model cannot be determined directly in experiments, as it is correlated to an ideally uniformly stressed material and not the values for tests on the real material in itself influenced by local stress peaks.

Height [mm]	Damage relevant Weibull stresses [MPa]			
	$k = 2$	$k = 5$	$k = 10$	$k = 100$
25	3.49	3.53	3.57	3.98
45	2.73	2.84	2.96	3.61
70	2.22	2.50	2.79	3.60
130	1.79	2.35	2.89	3.88

Table 4: Value of the damage relevant Weibull stress for different values of the shape parameter.

The failure criterion in (4), as proposed in (Aicher et al. 1998), is implemented using the experimental mean strength for each height and the stress distribution along the mid section shown in Figure 7. The emerging damage relevant Weibull stresses are shown in Table 4. If the stress integration in (4) yields a reliable failure criterion a shape parameter must exist such that the damage relevant Weibull stresses take a constant value independent of specimen height. A value of  $\sigma_{t,90,Wei}$  that deviates in the order 10% takes a shape parameter in the order of 100. This value of the shape parameter fitted to correspond to the ideally uniformly stressed material practically excludes size effect in this material as the slope in a  $\log(\text{strength})-\log(\text{volume})$  depiction takes the slope  $-1/100$ .

### 5.2.3 Fracture mechanical size effect

The size effect observed for the wood specimens conforms with the size effect expected from linear elastic fracture mechanics, i.e.  $\sigma_N \propto d^{-\frac{1}{2}}$ . However, the LVL specimens show no such variation with size. The clear wood and the LVL specimens were geometrically similar. According to (Fonselius 1986) the fracture toughness in the relevant radial plane is approximately  $267 \text{ kNm}^{-3/2}$  for clear spruce and approximately  $300 \text{ kNm}^{-3/2}$  for LVL and Gustafsson, Hoffmeyer & Valentin (1998) finds the values  $272 \text{ J/m}^2$  and  $310 \text{ J/m}^2$  for the fracture energy perpendicular to grain,  $G_{fy}$ , for glulam and LVL respectively. For these reasons the brittleness expressed as  $d/D_0$  in Equation (5) is equal for the clear wood and LVL specimens of equal size. Hence, the size effect for the clear wood specimens cannot be of fracture mechanical origin as it is not seen for the – in relevant aspects – similar LVL specimens.

### 5.2.4 Simple maximum stress failure criterion

In the preceding sections three existing models have been questioned as explanatory basis for the observed size effect. The elaborate models are suggested replaced by a simple maximum stress failure criterion based on the following arguments:

- The stiffness orthotropy in the transverse plane introduces a regular, inhomogeneous pattern of stress.
- This regular pattern leads to an increasing stress inhomogeneity for increasing size, thus giving rise to the size effect.

In this explanation the regularity of the wood structure, rather than weak spots and flaws as supposed in the weakest link theory, is responsible for strength reduction with increasing size.

The experimental evidence is the decrease in nominal strength with increased specimen height for the cylindrical orthotropic clear wood specimens and the absence of size effect for LVL specimens. The stiffness distribution of the LVL specimens differs from that of the clear wood in that the cylindrical orthotropy has been straightened out to a cartesian in the manufacturing process. Further the FEM simulations show increase in the stress inhomogeneity with increased height, Figure 7, for the cylindrical orthotropic wood specimens. In order to compare experiments and simulations it is assumed that failure occurs when the stress at any point,  $\sigma$ , reaches an inherent failure strength:

$$\sigma = f_{t,90} \quad (8)$$

By use of (8) a nominal strength,  $\sigma_{N,FEM}$ , can be calculated from the stress intensification factor,  $\alpha$ . The stress intensification factor is determined as the ratio between the maximum stress,  $\sigma_{max,FEM}$ , and the applied external stress,  $\sigma_{applied,FEM}$ :

$$\sigma_{N,FEM} = \frac{\sigma_{applied,FEM}}{\sigma_{max,FEM}} f_{t,90} = \frac{1}{\alpha} f_{t,90} \quad (9)$$

As a means of comparison between experimentally determined nominal strength,  $\sigma_N$ , and modelled nominal strength,  $\sigma_{N,FEM}$ , the values of the nominal strength have been normalised with the value for the 130 mm high specimens in Table 5. In this way the unknown inherent failure strength  $f_{t,90}$  vanishes. The experimental values of normalized nominal strength,  $\frac{\sigma_N}{\sigma_{N,130}}$ , and the modelled normalized nominal strength values,  $\frac{\sigma_{N,FEM}}{\sigma_{N,130,FEM}}$  coincide within approx. 10%. The consequence is that the stress inhomogeneity which increases for increased specimen height can explain the size effect observed. The good agreement between experimental observations and numerical simulations shown in Table 5 is the outcome of a specific choice of elastic constants and a simple maximum stress failure criterion. It may be argued that a more realistic failure criterion is an integration of stresses in excess of a critical value. This, however, would not change the general picture. The finite element model is fairly stable to perturbations of the values of the elastic constants, and a more refined stress failure criterion could be applied without violating the main point, namely that a given mean stress generates higher stresses in higher specimens.

Height [mm]	Experiments		FEM simulations	
	$\sigma_N$ [MPa]	$\frac{\sigma_N}{\sigma_{N,130}}$	$\frac{1}{\alpha} = \frac{\sigma_{applied,FEM}}{\sigma_{max,FEM}}$	$\frac{\sigma_{N,FEM}}{\sigma_{N,130,FEM}}$
25	3.5	2.2	0.85	2.1
45	2.7	1.7	0.72	1.8
70	2.1	1.3	0.56	1.4
130	1.6	1	0.40	1

Table 5: *Normalized nominal strength from experiments and simulation (index FEM).*

### 5.3 Implications

The difference between a simple maximum stress failure criterion and the traditional Weibull approach is whether the strength perpendicular to the grain is a deterministic or stochastic parameter. In the weakest link theory the material is assumed to fail when the mean stress reaches a stochastic volume dependent strength:

$$\sigma_{mean} = f_{t,90}(\text{strength distribution, volume}) \quad (10)$$

The simple maximum stress failure criterion operates with a deterministic material strength,  $f_{t,90}$ , and a deterministic stress distribution depending upon stiffness orthotropy and geometry variables including dimension of the loaded wood member as well as annual ring pattern. Failure is reached when the maximum value of the stresses reaches the material strength:

$$\sigma_{max}(\sigma_{mean}, \text{stiffness orthotropy, geometry}) = f_{t,90} \quad (11)$$

Due to the character of the failure criterion (11) the observed relation between specimen height and strength, Figure 9, is just an accidental function of the chosen test specimens, their height and special symmetrical geometry, Figure 1. For other specimen geometries other relations between size and strength are expected. As an example, it is well documented in the literature that a standard glulam cross section yields  $\sigma_N \propto \text{volume}^{-0.2}$ .

The practical implication of the proposed failure criterion may be that the stress distribution e.g. in a standard glulam cross section can be manipulated to yield higher nominal strength. In a glulam cross section all lamellas except the outer have the same orientation. This high degree of global cross sectional regularity combined with the regularity of stiffness distribution within each lamella can make the cross section concentrate the carrying stresses in a wedge shape pattern. In (Hoffmeyer, Damkilde & Pedersen 2000) this is shown in compression for an idealized cross section of six lamellas with the same pith distance and location; a stress intensification of  $\alpha = 4$  is observed over 6 lamellas. Other references

e.g. (Aicher & Dill-Langer 1997) do not see this global interaction between lamella and cross sectional lay-out as different pith location for each lamella reduces the development of a regular wedge shaped pattern of carrying stresses. In (Castéra & Lac 1997) both an idealized and a more random cross section is modelled. A wedge shaped pattern of carrying stresses is a function of the lamellas concentrating stresses in the same direction, and can be avoided if every second lamella is reversed. This may of course be prohibitive in other respects but would diminish if not remove a deterministic stress peak induced size effect.

## 6 Conclusion

The paper reports tension perpendicular to the grain tests on small clear spruce and LVL specimens from which the following observations are made:

- There is a large size effect for small clear specimens.
- The failure location is predetermined independent of specimen size.
- Geometrical similar specimens of LVL show no size effect.
- A FEM analysis shows the stress inhomogeneity to increase with specimen height.

The observations are attempted explained within the Weibull weakest link model, a damage relevant Weibull stress model and a fracture mechanical size effect model but the most promising is a simple stress failure criterion:

- The Weibull weakest link model is rejected as the failure location is predetermined. Further, a size effect  $\propto \text{volume}^{-0.5}$  is found, indicating that the material strength does not follow the commonly recognized Weibull strength distribution with shape parameter  $k = 5$ . Lastly, though a prime example of a Weibull material full of strength reducing flaws, LVL specimens show no size effect.
- A failure model using damage relevant Weibull stresses is questioned for theoretical reasons. Based on the experiments it is rejected as the stress giving the same failure probability for uniform stress state becomes volume independent only for values of  $k$  so high that no size effect is allowed in the uniformly stressed material.
- The observed size effect  $\propto \text{volume}^{-0.5}$  is identical to the brittle fracture mechanical size effect. However, fracture mechanics cannot explain the observations as the LVL specimens which have similar fracture properties show no size effect.

- A maximum stress failure criterion is promising when stress distribution determined by the use of cylindrical orthotropy is used. FEM modelling shows the stress inhomogeneity to increase with increased height for a constant mean stress and the normalized nominal strength from FEM modelling and experiments coincide.

The simple stress failure criterion apply to the investigated specimens. In a broader context the result of the investigation questions the correctness of the traditional stochastic explanation of size effect in tension perpendicular to the grain.

## References

- Aicher, S. & Dill-Langer, G. (1997), ‘Climate induced stresses perpendicular to the grain in glulam’, *Otto-Graf-journal* **8**, 209–231. FMPA - Otto-Graf-Institute, Stuttgart.
- Aicher, S. & Reinhardt, H. W. (1993), ‘Einfluss der Bauteilgrösse in der linearen und nichtlinearen (Holz-)Bruchmechanik’, *Holz als Roh- und Werkstoff* **51**, 215–220.
- Aicher, S., Dill-Langer, G. & Ranta-Maunus, A. (1998), ‘Duration of load effect in tension perpendicular to the grain of glulam in different climates’, *Holz als Roh- und Werkstoff* **56**, 295–305.
- Aicher, S., Reinhardt, H. W. & Klöck, W. (1993), ‘Nichtlinearen Bruchmechanik-Maßstabgesetz für Fichte bei Zugbeanspruchung senkrecht zur Faserrichtung’, *Holz als Roh- und Werkstoff* **51**, 385–394.
- Barrett, J. D. (1974), ‘Effect of Size on Tension Perpendicular-to-Grain Strength of Douglas-Fir’, *Wood and Fiber* **6**(2), 126–143.
- Bazant, Z. P. & Pfeiffer, P. A. (1987), ‘Determination of fracture energy from size effect and brittleness number’, *ACI Materials Journal* pp. 463–480.
- Castéra, P. & Lac, P. (1997), ‘Effet d’échelle en traction perpendiculaire pour un multicouche composé de lamelles orthotropes: cas du bois lamellé collé’, *French Journal of Timber Engineering, Annales GC Bois* **2**, 15–24.
- EC5-1 (1995), Eurocode 5 – Design of timber structures – Part 1–1: General rules and rules for buildings, Preliminary building code prENV 1995-1-1, European Committee for Standardization.

- Fonselius, M. (1986), Brottmekanisk studie på gran och skiktträ, Report 80, Helsinki University of Technology, Department of Civil Engineering, Division of Structural Engineering, Espoo, Finland. (In Swedish).
- Gustafsson, P. J., Hoffmeyer, P. & Valentin, G. (1998), ‘Dol behaviour of end-notched beams’, *Holz als Roh- und Werkstoff* **56**, 307–317.
- Hanhijärvi, A. & Ranta-Maunus, A. (1996), Computational analysis of the effect of transverse anisotropy and annual ring pattern in cross-sections of curved glulam beams on the size effect of strengths., *in* ‘Proceedings of European Workshop on application of statistics and probabilities in Wood Mechanics, Bordeaux, France, February 22–23, 1996’.
- Hearmon, R. F. S. (1948), The elasticity of wood and plywood, Special Report 7, Forest Products Research, London.
- Hoffmeyer, P., Damkilde, L. & Pedersen, T. N. (2000), ‘Structural timber and glulam in compression perpendicular to grain’, *Holz als Roh- und Werkstoff*.
- Kollmann, F. F. P. & Côté, W. A. (1984), *Principles of Wood Science and Technology*, Vol. I: Solid Wood, reprint edn, Springer-Verlag.
- Larsen, H. J. & Riberholt, H. (1981), Strength of Glued Laminated Beams. Part 4, Technical Report 8110, Institute of Building Technology and Structural Engineering, Aalborg University Centre, Aalborg, Denmark.
- Mistler, H. (1998), ‘Querzug-Bemessung von BSH-Trägern nach EC 5. Ein Vergleich mit Forschungsergebnissen’, *Holz als Roh- und Werkstoff* **56**, 51–59.
- Ranta-Maunus, A. (1996), The influence of changing state of stress caused by mechano-sorptive creep on the duration of load effect, *in* S. Aicher, ed., ‘Proceedings of the 1996 International Conference on Wood Mechanics, Stuttgart, Germany, May 14–16, 1996’, pp. 187–201.

# Compressive fatigue in wood

C. O. Clorius, M. U. Pedersen, P. Hoffmeyer, L. Damkilde

**Summary** An investigation of fatigue failure in wood subjected to load cycles in compression parallel to grain is presented. Small clear specimens of spruce are taken to failure in square wave formed fatigue loading at a stress excitation level corresponding to 80% of the short term strength. Four frequencies ranging from 0.01 Hz to 10 Hz are used. The number of cycles to failure is found to be a poor measure of the fatigue performance of wood. Creep, maximum strain, stiffness and work are monitored throughout the fatigue tests. Accumulated creep is suggested identified with damage and a correlation is observed between stiffness reduction and accumulated creep. A failure model based on the total work during the fatigue life is rejected, and a modified work model based on elastic, viscous and non-recovered viscoelastic work is experimentally supported, and an explanation at a microstructural level is attempted. The outline of a model explaining the interaction of the effect of load duration and the effect of the loading sequences is presented.

## 1

### Introduction

Three fundamentally different types of models have been used to describe wood fatigue. Wöhler curves states fatigue resistance in number of cycles,  $N$ , and stress level, whereas duration of load models explain failure by the total accumulated time under load,  $T$ , and denies any effect of the oscillations of the load counted by  $N$ . Finally, energy criteria have been suggested in various forms, formalised as critical values of energy stored in one or more elements of rheological models.

### 1.1

#### Wöhler curves

Wöhler curves, or  $S$ - $N$  diagrams, describe fatigue resistance by a critical value of load cycles,  $N$ , leading to failure at a given stress level,  $S$ , e.g.:

$$\log(N) = A + B \cdot \log(S) \quad , \quad (1)$$

where the coefficients  $A$  and  $B$  depend on the factor  $R$ , which is determined as  $R = S_{\min}/S_{\max}$ , where  $S_{\min}$  and  $S_{\max}$  are the minimum and maximum stress level in a cycle, respectively. The number of cycles to failure is determined in constant

---

*Received 8 December 1997*

C. O. Clorius (✉), M. U. Pedersen, P. Hoffmeyer, L. Damkilde  
Department of Structural Engineering and Materials,  
Technical University of Denmark, DK-2800 Lyngby

amplitude tests at a number of different stress levels with varying R values as done by Bonfield (1991) in an extensive experimental work. This leads to empirical relations of the form given in (1). In order to verify the Palmgren–Miner summation rule Bonfield carried out tests where each specimen was subjected to different stress levels. The main results from (Bonfield, 1991) are presented in (Bonfield and Ansell, 1991). Based on these results a life prediction analysis is presented in (Bonfield et al., 1994).

The nature of Bonfield's life prediction analysis based on Wöhler curves is presented in (Ansell, 1995). An explanation of the fatigue phenomena is not established, but the underlying theory for the empirical fits is a Paris law relation, placing all emphasis on N according to the fracture mechanical approach presented in (Ansell, 1987).

## 1.2

### Duration of load

In an investigation by Bach (1975) wood fatigue is suggested reduced to a duration of load phenomenon. Bach investigated the influence of frequency,  $f$ , on fatigue failure. Compressive square wave shaped load cycles were imposed parallel to grain on small clear specimens at frequencies ranging from 0.1 Hz to  $10^{-6}$  Hz spaced by one decade. The number of cycles to failure was reduced from several hundred to one in the frequency range investigated. It was concluded that failure is best predicted by T determined as:

$$T = \frac{N}{2f} , \quad (2)$$

where  $1/2f$  is the time under load in each cycle.

## 1.3

### Energy criteria

Energy based failure criteria are expressed as a critical value of a specific energy quantity,  $w$ , which is calculated as an integral of a stress component times the corresponding strain increment:

$$w = \int \sigma d\varepsilon . \quad (3)$$

The stress component can be identified with the stress in an element of a rheological model. Due to the time dependent properties of wood, energy based failure criteria can be expressed in rates of stress,  $\dot{\sigma}$ , and strain,  $\dot{\varepsilon}$ , or generally stress work rate,  $\dot{w}$ :

$$w(t_f) = \int_0^{t_f} \dot{\sigma} \varepsilon + \sigma \dot{\varepsilon} dt = \int_0^{t_f} \dot{w} dt . \quad (4)$$

A simple theoretical basis can be a four element viscoelastic rheological material model, Fig. 1, representing the three strain components: elastic strain,  $\varepsilon_E$ , viscoelastic strain,  $\varepsilon_{VE}$  and viscous strain,  $\varepsilon_V$ . Integrating all stress and strain components of the model in Fig. 1 yields the total stress work (4).

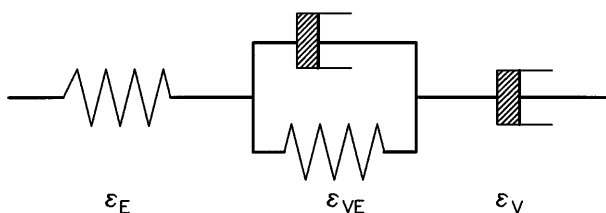


Fig. 1. Four element viscoelastic model, the Burger model

An elaborate energy failure criterion was put forward by Reiner and Weissenberg (1939). This criterion has recently been theoretically exploited by Liu and Ross (1995). According to the Reiner–Weissenberg theory failure will occur when the strain work,  $w_c$ , due to the recoverable part of the deformation attains a critical value. Hence, the dissipation rate of non-elastic energy,  $\dot{D}$ , is subtracted from the work integral:

$$w_c(t_f) = \int_0^{t_f} (\dot{w} - \dot{D}) dt . \quad (5)$$

The Reiner–Weissenberg theory as expressed by Eq. (5) states failure at a critical value of the energy stored due to  $\varepsilon_E$  and  $\varepsilon_{VE}$ . However, the Reiner–Weissenberg theory does not include stress relaxation failure as observed by Bach (1967). Stress relaxation failure occurs at constant strain condition due to redistribution of the strain components. To include stress relaxation failure Bach (1973) proposed a modification of (5). The modified criterion includes only the energy stored due to  $\varepsilon_{VE}$ , hence the instantaneously recoverable elastic energy at failure,  $w_c^E(t_f)$ , is excluded. The criterion takes the form:

$$w_c^{VE}(t_f) = -w_c^E(t_f) + \int_0^{t_f} (\dot{w} - \dot{D}) dt . \quad (6)$$

Bach (1975) attempted to verify the criterion (6) experimentally. However, Bach found that failure was best expressed by a time under load criterion.

Philpot et al. (1994) discuss energy based failure models. In a work density model failure is suggested identified with a critical value of the total work, Eq. (4), due to all strain components in Fig. 1. However, this model has the theoretical obstacle of rupture at almost any magnitude of load under repeated loading due to creep recovery, i.e. regain of  $\varepsilon_{VE}$  in periods without load. Hence, a modification is suggested which omits the work corresponding to creep recovery, i.e. the energy corresponding to the closed part of the hysteresis loop in a load cycle. The modification takes an empirical form and essentially the modified work density model Philpot et al. (1994) is a stress level dependent criterion on the maximum strain.

## 2

### Test outline and data acquisition

The aim of the present study is to explore the interaction of N and T in a series of wood fatigue experiments. The study assesses the validity of the three types of

failure criteria put forward in Sect. 1 and suggests a damage mechanical approach, i.e. an approach that takes into consideration the influence of 2nd order phenomena such as stiffness reduction on the accumulation of damage leading to failure. The following quantities have been measured throughout the tests:

- Number of cycles and time to failure
- E-moduli from loading and unloading sequences
- Maximum and minimum strain in each cycle
- Dissipated energy

## 2.1

### Test plan

Small clear prismatic ( $25 \times 25 \times 75$  mm) specimens of spruce (*Picea abies*) were taken to failure in compressive square wave shaped fatigue loading parallel to grain. The stress excitation level oscillated between 80% and 0.8% of the short term strength. Four frequencies ranging from 0.01 Hz to 10 Hz were used. The tests have been performed on two samples in equilibrium with 65% RH and 85% RH respectively. A fatigue specimen was the mid specimen of three in the fiber direction consecutive clear specimens. The reference short term strength of the fatigue specimen was determined on the basis of the two neighbouring specimens taken to failure in approximately 90 s. Specimens were used in fatigue testing only if the two reference short term strength values deviated less than 4% interpreted as an uncertainty of  $\pm 2\%$  on the short term strength. The density range was from  $377 \text{ kg/m}^3$  to  $437 \text{ kg/m}^3$ .

## 2.2

### Experimental set-up and machine performance

The specimens were placed centrally between stiff compression planes of the test machine and equipped with two extensometers with a gauge length of 50 mm. The specimens were taken directly from the conditioning chambers to the test machine where they were immediately sealed off from the environment by a polyethylene tubing. The specimens suffered a mean reduction in moisture content of 0.5% during testing. The machine used for the testing is an 250 kN 8502 INSTRON actuator. The actuator can apply load to the specimens with a rate of approximately 2900 kN/s with overshoots of no more than 2% of the load amplitude. In the tests the fatigue load ranged between approximately 0.1 kN and a maximum load between 15 and 24 kN leading to load rise and load fall times from 5 to 8 ms.

## 2.3

### Data acquisition

It is possible to collect a set of data every 0.4 ms, leading to 15–17 sets of data for each loading or unloading sequence when data for time, load, deformation, strain and cycle number are collected simultaneously. In the constant load sequences the acquisition is restricted to 25 sets of data. The number of cycles stored is restricted by a criterion set on amplitude of strain supplemented by a linear sampling criterion. Figure 2 shows the load time and load strain history for a cycle at 10 Hz.

Data points for the regression analysis of the E-moduli are restricted to those in the interval with maximum load application rate, that is, between two successive data points the difference in load must be greater than 0.4 kN and the

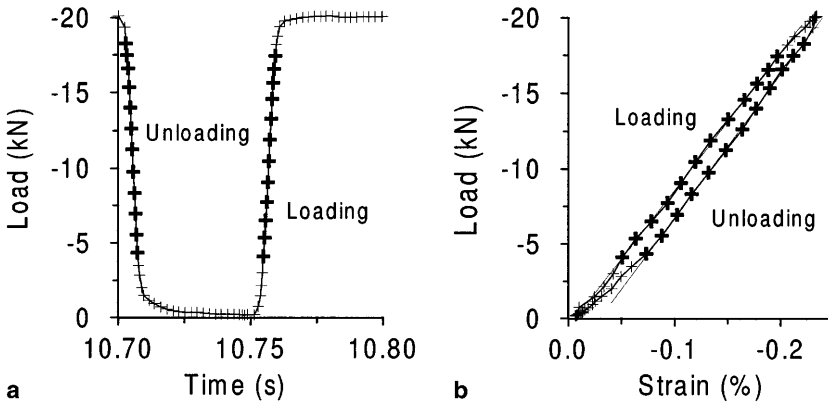


Fig. 2. Load-time and corresponding Load-strain diagram for a 10 Hz test

difference in time must be no more than 0.6 ms. The highlighted data at the linear flanges of the time load history in Fig. 2 are used for the determination of the E-modulus in loading,  $E_L$ , and unloading,  $E_U$ .

The energy represented by the area under the stress strain curve of each load cycle is determined. Fig. 3a shows area or work density for three separate load cycles. The total work density is calculated as the sum of work density for all load cycles. As the hysteresis loops overlap, the area below the envelope of all load cycles is covered several times. An interpolation is used to estimate the value of the work density of the cycles not recorded. The energy represented by the area below the envelope of all hysteresis loops, Fig. 3b, corresponds to the modified work density introduced by (Philpot et al., 1994).

As adiabatic heating may be present, especially in the high frequency tests, additional specimens were equipped with thermo-elements glued into the specimens to monitor any temperature development during testing.

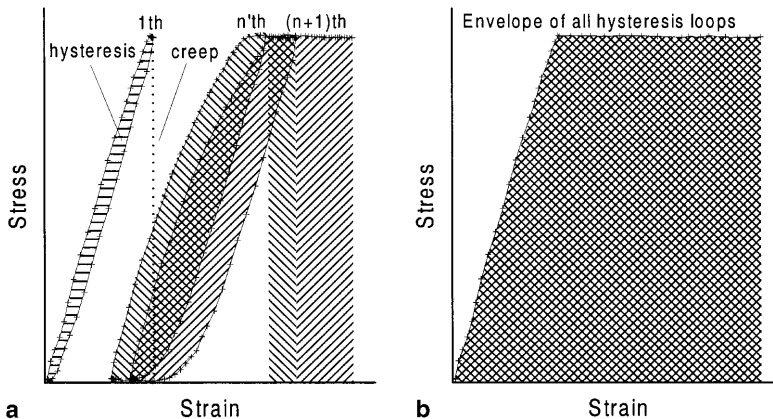


Fig. 3a, b. Calculation of work density. a Total work as sum of work in all cycles. b Modified work corresponding to envelope of all cycles

### 3

## Results

### 3.1

#### Number of cycles and time to failure

The mean number of load cycles to failure,  $\bar{N}$ , is given in Table 1 for all specimens tested. Obviously,  $\bar{N}$  increases with the frequency. Though the scatter is substantial, the four frequencies result in significantly different values of  $\bar{N}$ .

The substantial standard deviation  $s_N$  probably reflects a logarithmic relation between  $N$  and stress level. By using data from Bach (1975) the uncertainty of  $N$  due to the known uncertainty of  $\pm 2\%$  on the reference strength can be estimated to  $\pm 0.3$  decade. As  $s_{\log(N)}$  is less than 0.6 decade, Table 1, the bulk part of the scatter can be explained by the uncertainty of the reference strength.

The values of mean time under load to failure,  $\bar{T}$ , in Table 1 present no new information, as  $T = N/2f$  due to the square wave load cycles. However,  $\bar{T}$  accentuates that the survival time decreases with increasing frequency.

The shorter fatigue lives met in the high frequency tests may reflect a temperature related strength reduction. The result of the temperature monitoring of 8 specimens is shown in Fig. 4. The adiabatic heating is found to be insignificant for testing at frequencies up to 1 Hz. At 10 Hz the temperature rise from test start to failure is of the order of  $10^\circ\text{C}$ . According to Gerhards (1982) this is equivalent to a strength reduction of the order 5–10%. The temperature increase was not followed by a corresponding loss of moisture.

### 3.2

#### Failure modes

The visual failure was seen either as a fine-meshed pattern of compression zones scattered over a large section of the specimen or as localised failure restricted to one compression band. The visible failure developed during the last few load cycles. The two categories of failure modes are shown in Fig. 5. The proportion of fine-meshed failures increases with decreasing frequency and increasing moisture content as seen in Table 2. A similar dependency of failure mode and time under load is reported in (Madsen, 1992).

### 3.3

#### Stiffness development

The stiffness decreases during the fatigue life; this gives a fatigue life dependent E-modulus,  $E(t)$ . The stiffness,  $E_U(t)$ , recorded in the unloading sequences develops somewhat differently from the stiffness,  $E_L(t)$ , in the loading sequences. Generally, the stiffness reduction obtained in the unloading sequence is smaller than the reduction obtained in the loading sequence.

Figure 6 exemplifies the development of stiffness obtained from loading and unloading sequences. The reduction of the stiffness obtained in loading is determined as function of the fatigue life:

$$\text{Stiffness reduction} = \frac{E_L(t)}{E_L(0)}, \quad (7)$$

where the initial stiffness,  $E_L(0)$ , is defined as the stiffness recorded in the loading sequence of the 2nd load cycle. The specimens failing within the gauge length of the extensometers all exhibit reduction of stiffness during the fatigue life, whereas

**Table 1.** Number of cycles to failure and time under load to failure

Frequency [Hz]	No. of specimens		Mean no. of cycles to failure $\bar{N}$		Standard deviation $s_N$		Mean log(N)		Standard deviation $s_{\log(N)}$		Mean time under load $\bar{T}$ [sec]		Mean log(T)	
	65	85	65	85	65	85	65	85	65	85	65	85	65	85
RH [%]	65	85	65	85	65	85	65	85	65	85	65	85	65	85
0.01	12	12	48	26	35	41	1.60	1.10	0.29	0.56	2421	1308	3.29	2.80
0.1	14	12	284	98	262	81	2.32	1.82	0.34	0.42	1420	490	3.02	2.52
1	12	11	3048	367	3569	213	3.27	2.47	0.44	0.34	1524	183	2.97	2.17
10	11	11	21749	4431	29905	7529	4.09	3.38	0.46	0.43	1087	222	2.79	2.08

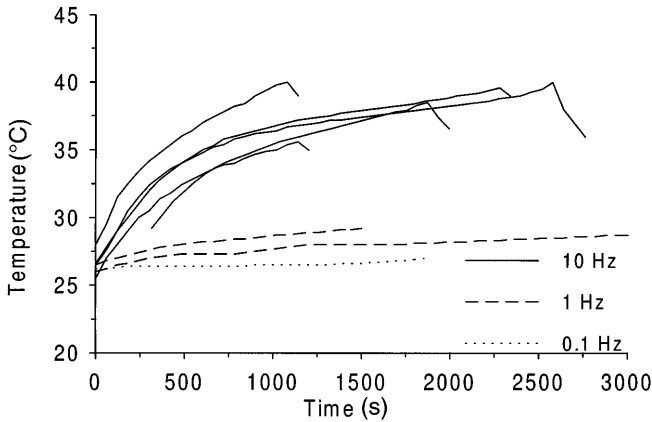


Fig. 4. Temperature development during testing

the stiffness reduction for the specimens failing outside the gauge length of the extensometers is less characteristic. Hence, values for specimens failed outside the extensometer gauges are excluded from Table 3. The table lists stiffness reductions at 0.1 and 0.9 fatigue life.

In order to quantify the different developments of  $E_U$  and  $E_L$ , the ratio between the stiffness recorded in unloading and loading sequences at any given time of the fatigue life is defined in Eq. (8). Table 3 gives the ratio determined at 0.1 and 0.9 of the fatigue life.

$$\text{Stiffness ratio} = \frac{E_U(t)}{E_L(t)} \quad (8)$$

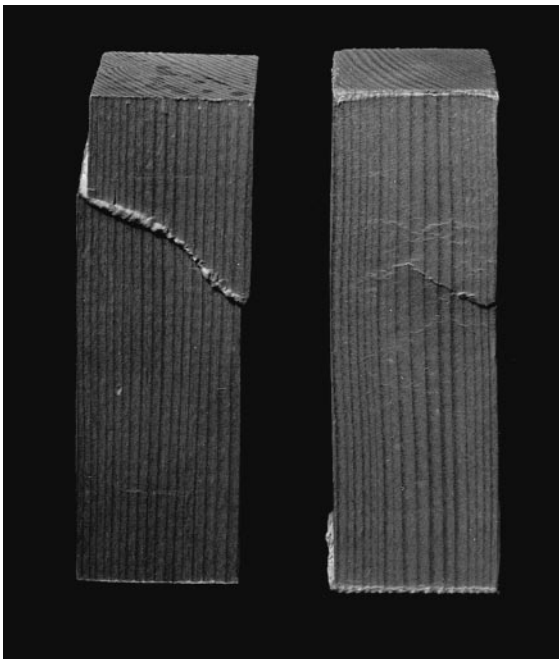
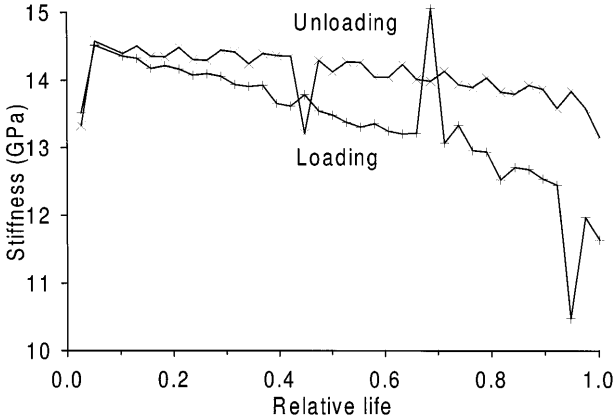


Fig. 5. A specimen failed in localised failure (left) and one failed in fine-meshed pattern (right)

**Table 2.** The ratio (in %) of specimens failed in a fine-meshed pattern to total number of specimens

Freq. [Hz]	0.01	0.1	1	10
65% RH	17	21	8	0
85% RH	33	25	18	9



**Fig. 6.** Development of  $E_U$  and  $E_L$ , 85% RH, 0.01 Hz

**3.4 Strain development**

Residual strain is defined as the strain measured at the end of an unloaded sequence at any given time of the fatigue life. Figure 7 exemplifies the development of residual strain for specimens at 85% RH. The development is seen to be highly frequency dependent; the higher the frequency the more rapid the development of final failure when a critical residual strain level is met. The magnitude of the residual strain is moisture dependent. The 85% RH specimens have twice the residual strain of the 65% RH specimens at 0.95 fatigue life as seen from Table 4. The maximum strain at 0.0 and 0.95 fatigue life is seen in Table 4. At 0.0 fatigue life the maximum strain of the moist specimens is less than the maximum strain of the dry specimens. This reflects that going from dry to moist condition yielded a 25% strength reduction not followed by a significant stiffness reduction.

**Table 3.** Mean stiffness reductions and ratios at 0.1 and 0.9 fatigue life

Freq [Hz]	Stiffness reduction				Stiffness ratio			
	0.1 fatigue life		0.9 fatigue life		0.1 fatigue life		0.9 fatigue life	
	65% RH	85% RH	65% RH	85% RH	65% RH	85% RH	65% RH	85% RH
0.01	1.01	0.99	0.96	0.89	1.00	1.03	1.01	1.09
0.1	1.01	0.99	0.97	0.86	1.00	1.03	1.02	1.10
1	1.01	1.01	0.97	0.89	1.00	1.01	1.01	1.08
10	1.01	1.02	0.97	0.94	1.00	1.01	1.01	1.06

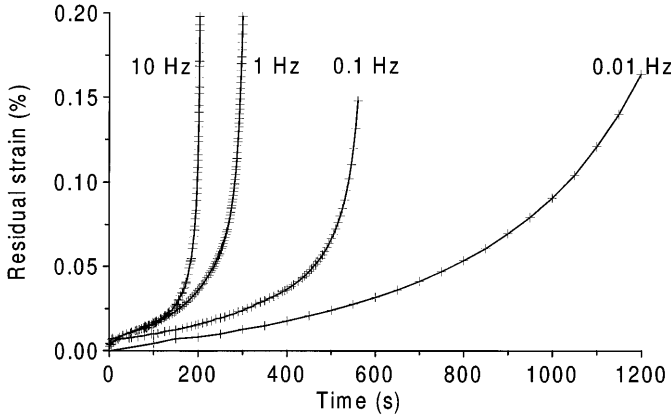


Fig. 7. Development of residual strain for four 85% RH specimens

Table 4. Maximum and residual strain at various stages of the fatigue life

RH [%]	Maximum strain				Residual strain	
	0.0 fatigue life		0.95 fatigue life		0.95 fatigue life	
	$\bar{\epsilon}_{\max}$ [%]	$s_{\epsilon_{\max}}$ [%]	$\bar{\epsilon}_{\max}$ [%]	$s_{\epsilon_{\max}}$ [%]	$\bar{\epsilon}_{\text{res}}$ [%]	$s_{\epsilon_{\text{res}}}$ [%]
65	0.27	0.02	0.35	0.07	0.06	0.04
85	0.22	0.02	0.41	0.06	0.11	0.03

However, at 0.95 fatigue life the maximum strain of the moist specimens exceeds the maximum strain of the dry specimens. This corresponds to the observation that more residual strain is accumulated in the moist specimens.

### 3.5

#### Energy development

The total work density of the specimens, Eq. (4), has been calculated at 0.5 and 0.9 fatigue life for all specimens, Table 5. The values of the total work density is highly dependent on frequency. Though more energy is dissipated per cycle in low frequency tests this is outweighed by the higher number of cycles met in high frequency tests. The modified work density does not show this frequency dependency. Mean values of the modified work density at 0.1 and 0.9 fatigue life are given in Table 5.

## 4

### Discussion

#### 4.1

##### Effect of frequency and moisture

In a statistical analysis the number of cycles to failure,  $N_{ijk}$ , is the random response of a process with two fixed effects: frequency,  $f_i$ , and moisture content,  $m_j$ ; and  $k$  replicants. A variance stabilizing transformation,  $Y_{ijk} = \log(N_{ijk})$ , is used in order to perform an analysis of variance. The transformation implies that the data

**Table 5.** Mean values of total and modified work density

Freq [Hz]	Total work density [kPa]				Modified work density [kPa]			
	0.5 fatigue life		0.9 fatigue life		0.1 fatigue life		0.9 fatigue life	
	65% RH	85% RH	65% RH	85% RH	65% RH	85% RH	65% RH	85% RH
0.01	360	320	680	740	62.9	38.0	92.7	100.7
0.1	1350	480	3250	1310	57.5	34.8	81.3	63.2
1	18950	1490	35800	3260	50.2	38.5	64.7	75.3
10	39300	25650	73200	49900	55.7	37.4	73.0	60.7

are logarithmically normal distributed. This assumption is confirmed by a normal probability test on the residuals from the final analysis. The statistical analysis is performed according to Montgomery (1997). The following linear two-factor statistical model including interaction is used:

$$Y_{ijk} = \mu + f_i + m_j + fm_{ij} + E_{ijk} \quad \begin{cases} i = 1, 2 & \text{two moisture levels} \\ j = 1, 2, 3, 4 & \text{four frequencies} \\ k = 1, 2, \dots, n & \text{number of replicates} \end{cases}, \quad (9)$$

where  $\mu$  is the mean,  $fm_{ij}$  is the interaction term between the effects of frequency,  $f_i$ , and moisture,  $m_j$ , and  $E_{ijk}$  is the random error. Both the effect of frequency  $f_i$  and the effect of moisture  $m_j$  are highly significant with levels of confidence in excess of 99.9%. The analysis show the interaction  $fm_{ij}$  to be non-significant which means that the reduction of  $\log N$  when going from low to high moisture content is independent of the frequency. The consequence on the non-transformed data is a moisture effect proportional to the frequency. A Newman-Keuls test on the differences between the effects of frequencies shows that:  $f_1 \neq f_2 \neq f_3 \neq f_4$  at a level of confidence higher than 99%.

As  $N$  is logarithmically normal distributed and as the frequencies range three decades, a double logarithmic diagram is used to present the data of Table 1. Figure 8 shows the  $\log(N)$ - $\log(f)$  relations with linear regression lines, both with and without tests performed at 10 Hz. When the whole frequency range is used

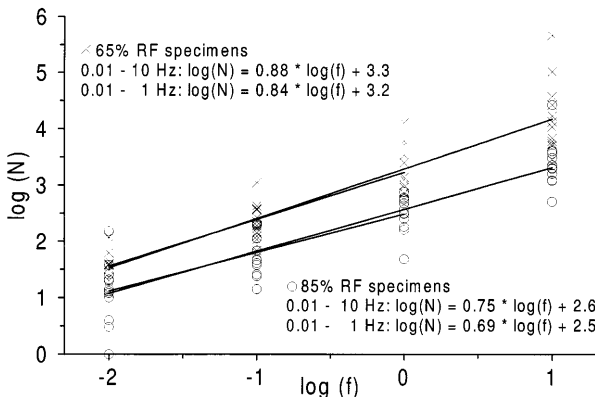


**Fig. 8.**  $\log(N)$  versus  $\log(f)$

the coefficients of determination are  $r^2 = 0.84$  and  $r^2 = 0.79$  for the dry and moist specimens respectively. These values are acceptable considering both the large scatter of  $N$  obtained for each frequency and the narrow  $\log(f)$  range. The values of the standard error of regression,  $s_{yx}$ , are within the bounds of the standard deviations,  $s_{\log(N)}$ , observed for all groups individually, Table 1.

The linear fits in Fig. 8 express the relation between  $N$  and  $f$  in the following form:

$$\log(N) = a \cdot \log(f) + b \Rightarrow N = cf^a \quad (10)$$

32

The sensitivity of the fatigue life to number of loading sequences, the “cycle effect”, is reflected in the exponent  $a$ ; the smaller the exponent, the greater the influence of the mere number of loading sequences. For  $a = 0$  a failure criterion can be expressed solely in terms of  $N$ , see Eq. (1), whereas  $a = 1$  leads to a duration of load criterion, see Eq. (2). As  $a$  is less than 1 for the regression lines in Fig. 8, time under load does not fully explain the relation between  $N$  and  $f$ . Due to the smaller exponent the moist specimens seem to be more susceptible to the number of loading sequences. However, differences in the exponent correspond to the interaction term,  $fm_{ij}$ , which is not statistically significant. The “cycle effect” observed cannot be explained by strength reduction due to adiabatic heating in the 10 Hz tests as the slope of the regression lines does not increase when the 10 Hz data are excluded from the regression. Though not global, the relations between  $\log(N)$  and  $\log(f)$  as presented in Fig. 8 are reliable in the frequency region investigated and the following conclusions can be drawn:

- The number of cycles to failure increases in a non-linear way with increasing frequency in the range from 0.01 Hz to 10 Hz, i.e. an increase of  $f$  results in increasing  $N$  but also reduced time to failure.
- The number of cycles to failure decreases with increasing moisture content even though the maximum stress is chosen as the same fraction of the moisture dependent short term strength.

## 4.2

### Failure criterion on $N$ or $T$

The number of cycles decreases from an order of  $10^3$  at 10 Hz to an order of 10 at 0.01 Hz. Consequently, Wöhler curves, (1), are useless in compressive fatigue description without a third dimension representing frequency. The results also show that time to failure decreases for increasing frequency. Hence, a failure criterion cannot be expressed as a duration of load criterion, (2).

## 4.3

### Strain and stiffness development

At the microstructural level non-recoverable viscous strain has been identified as slip planes by Hoffmeyer (1993) and Hoffmeyer and Davidson (1989). At a high intensity of this type of microstructural damage fatal compression bands form. Stiffness reduction is a natural consequence of slip planes due to the change in material properties. The monitoring of stiffness reduction may reveal the formation of compression bands before they become visible, and a correlation between residual strain and stiffness reduction is expected.

From Table 3 it is seen that the stiffness initially increases. The stiffness increase may be explained by permanent set during load application in the first load

cycles, i.e. a consolidation process. Apart from this the stiffness is reduced during the fatigue life for all frequencies at both moisture contents. The stiffness reductions observed for the moist specimens are systematically larger than for the dry specimens. The larger stiffness reductions for the moist specimens correspond to the larger levels of residual strain observed for these specimens, Table 4.

The development of stiffness reduction follow the overall shape of the accumulation of residual strain as shown in Fig. 7; i.e. the stiffness reduction is a function of accumulated damage independent of test frequency. In Fig. 9 the stiffness reduction is given as function of residual strain for four frequencies; the frequency invariance is obvious.

#### 4.4

##### Origin of residual strain

The residual strain is the strain measured at the end of the unloaded sequences. As the unloaded sequences have finite duration, full creep recovery is not possible and some of the residual strain is recoverable. However, from an early stage of the fatigue life the creep recovery is an order of magnitude smaller than the residual strain as both reported by Bach (1975) and indicated by pilot tests. Hence, the residual strain is believed to express non-recoverable strain or damage.

Development of viscous strain is known to be dependent upon stress level, time, moisture content and fluctuations as well as the creep level itself. In this context these parameters do not fully explain the frequency dependency of the residual strain developments seen in Fig. 7. Some of the accumulation of the residual strain must be reckoned as time dependent creep, identified as slip plane formation on a microstructural level. The viscous strain rate,  $\dot{\varepsilon}_V$ , is assumed to be dependent of the level of accumulated residual strain,  $\dot{\varepsilon}_V(\varepsilon_{res})$ . During cyclic square wave loading at a given stress level, the accumulation of time dependent viscous strain,  $\varepsilon_V$ , is expressed by the formula:

$$\varepsilon_V = \sum_{n=1}^N \int_0^{1/2f} \dot{\varepsilon}_V(\varepsilon_{res}) dt \quad (11)$$

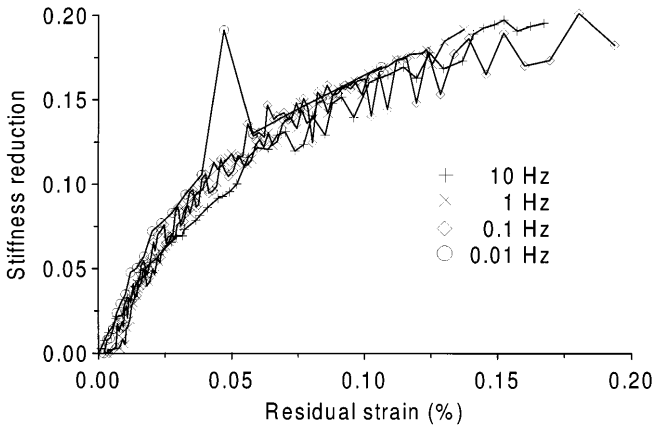


Fig. 9. Stiffness reduction as function of residual strain, 85% RH specimens

However, as the time under load to failure,  $T = N/2f$ , decreases for increasing frequency Eq. (11) does not consider the more rapid accumulation of residual strain in high frequency tests. To explain the frequency dependent accumulation of residual strain, time independent strain residuals,  $\Delta\epsilon_N$ , introduced in the loading sequences must be invoked. Letting this strain increment be dependent on the level of residual strain,  $\Delta\epsilon_N(\epsilon_{res})$ , a simple formula for the accumulation of  $\epsilon_N$  due to  $N$  square wave load cycles at a given stress level would be:

$$\epsilon_N = \sum_{n=1}^N \Delta\epsilon_N(\epsilon_{res}) \quad (12)$$

The experimental evidence for the existence of time independent strain residuals  $\Delta\epsilon_N(\epsilon_{res})$  is the different Young's moduli in loading and unloading, i.e. the stiffness ratio. From Table 3 it is seen that up to 10% of the apparent elastic strain gained in loading is not regained in unloading. In Fig. 6 it is seen how the stiffness ratio is an increasing function of the fatigue life, which verifies that  $\Delta\epsilon_N$  is dependent on the level of residual strain.

The consequence of  $\Delta\epsilon_N$  is that the mere loading sequences contribute to the accumulation of damage. Combining (11) and (12) gives an expression for the two sources of accumulation of residual strain:

$$\epsilon_{res} = \epsilon_V + \epsilon_N = \sum_{n=1}^N \int_0^{1/2f} \dot{\epsilon}_V(\epsilon_{res}) dt + \sum_{n=1}^N \Delta\epsilon_N(\epsilon_{res}) \quad (13)$$

Though heuristic in form, the algorithm (13) explains the experimental observations as the first term dominates the accumulation of residual strain in high frequency tests, leading to shorter fatigue lives, whereas the second term dominates in low frequency tests. The moisture induced reduction of time to failure is explained by higher creep rates in moist wood, i.e. by facilitated formation of slip planes (e.g. Hoffmeyer, 1990; Hoffmeyer and Davidson, 1989).

Figure 10 shows a schematic version of the developments of the residual strain curves given in Fig. 7. The sloping lines model  $\dot{\epsilon}_V$  under constant load, i.e. the

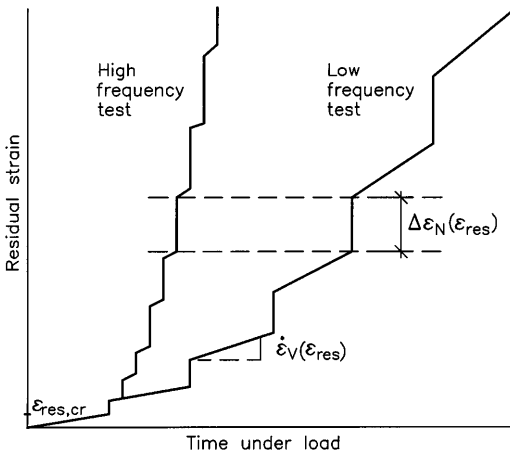


Fig. 10. Schematic development of residual strain for high and low frequency tested specimen

slope is a linearisation of  $\dot{\varepsilon}_V(\varepsilon_{\text{res}})$ . The vertical lines model  $\varepsilon_N$  introduced in the loading sequences.

The critical residual strain level,  $\varepsilon_{\text{res,cr}}$ , in Fig. 10 corresponds to the occurrence of the first premature failure zone, i.e. the first cluster of slip planes. From this stage on the development towards failure is frequency dependent:

- In low frequency testing the accumulation of residual strain is dominated by creep (11), i.e. formation of slip planes in periods with constant load.
- In high frequency testing the accumulation of residual strain is dominated by damage induced in the loading sequences (12), i.e. time independent residual strain increments.

It is unlikely that the damage introduced in the loading sequences,  $\varepsilon_N$ , is for-  
 mation of additional slip planes, as slip plane formation is generally recognised as  
 a time dependent process identified with viscous creep,  $\varepsilon_V$ , (Hoffmeyer, 1993) or  
 (Hoffmeyer and Davidson, 1989). Hence, the additional damage in the loading  
 sequences may be seen as the effect of the loading process working on existing  
 slip planes. This interpretation of the damage introduced in the loading sequences  
 is confirmed by the visible failure morphology. In low frequency tests the failure  
 zones form randomly in the specimen as function of time and load leading to the  
 higher number of fine-meshed failures, Table 2. Conversely, the failure of the high  
 frequency tested specimens are confined to one compression band due to loading  
 sequence induced enlargement of the first premature failure zone.

## 4.5

### Energy based failure criterion

A failure criterion expressed in terms of the total work is rejected as the work on  
 the specimens at 0.9 fatigue life, Table 5, in high frequency testing is found to be  
 70–100 times the work on the specimens in low frequency testing. Contrary to the  
 work density the modified work density is of the same order of magnitude for  
 tests at different frequencies. The moist specimens that are exposed to lower  
 absolute stresses than the dry specimens exhibit larger values of the maximum  
 strain near failure, Table 4. This is of course a necessary consequence of the  
 modified work density criterion, as this essentially is a stress level dependent  
 criterion on the maximum strain as illustrated in Fig. 11. The idealisation in  
 Fig. 11 is verified by the values from Table 5. Initially, at 0.1 fatigue life, the  
 modified work density is significantly lower for the moist specimens, however  
 near failure, at 0.9 fatigue life, the moisture dependency is no longer significant.

## 4.6

### Strain-stability failure criterion

The consequence of the modified work density failure criterion is that failure at  
 low stress levels will occur at higher strain levels than failure at high stress levels,  
 as idealised in Fig. 11. The observation of accumulated residual strain confirms  
 this conjecture. Observations of overall compression failures support the view  
 that failure is initiated at a higher level of microstructural damage at lower stress  
 levels. The description of compression failure such as presented in (Hoffmeyer,  
 1990) reveals that the overall compression failure is initiated by cell wall buckling  
 in earlywood preceded by slip plane formation in latewood, Fig. 12.

The moist and dry specimens were loaded equally severely relative to the short  
 term strength values. However, relative to the stiffness the moist specimens were  
 loaded less severely than the dry specimens. Hence, it is not unlikely that more

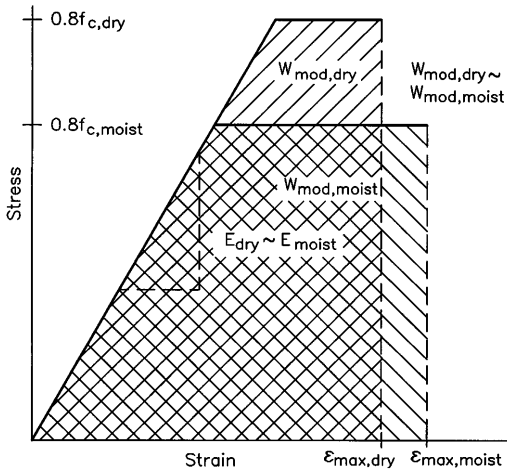


Fig. 11. Consequence of the modified work density failure criterion idealised in a stress strain diagram

damage is needed to introduce overall failure of the wood in the moist case if the final formation of compression bands is a cell wall buckling phenomenon governed by the overall stiffness of the material. This damage–stability interaction offers a micromechanical explanation to the modified work density criterion.

## 5

### Conclusion

From the present compressive fatigue test the following is concluded with respect to modelling of fatigue failure:

- Number of cycles is an inadequate measure of wood fatigue life as it is highly dependent on test frequency.
- Total time under load to failure decreases with increasing test frequency.

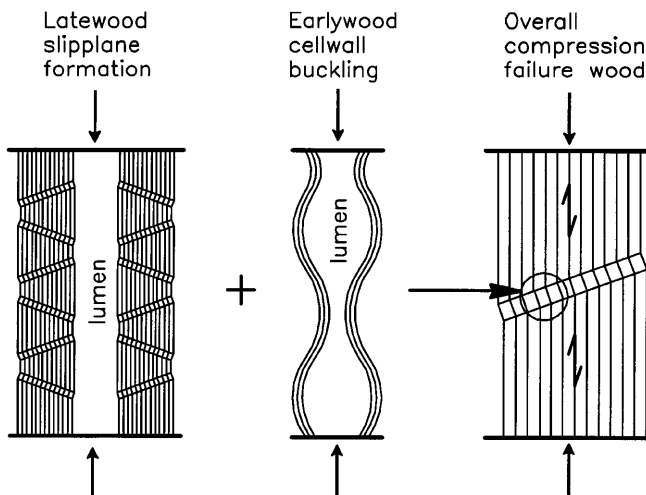


Fig. 12. Slip plane formation in latewood precedes cell wall buckling in earlywood resulting in overall compression failure

- Total work density can not explain fatigue failure as it is highly dependent on test frequency.
- A modified work density criterion, in effect a stress level dependent criterion on the maximum strain, is more promising.
- A conjecture to explain a stress level dependent strain criterion is made based on damage level and stability considerations.

A damage mechanical approach is suggested resting on damage accumulated as:

- Time dependent creep, i.e. slip planes developed during constant load periods.
- Permanent set introduced in the loading sequences, probably introduced as further damage of already formed slip planes.

The approach has the merit of being able qualitatively to explain why the time to failure is reduced with increasing test frequency. Further, there is phenomenological evidence from the visible failure morphology that two modes of damage accumulation are present in compressive wood fatigue, and that permanent set from the loading sequences dominates high frequency fatigue tests.

## References

- Ansell MP** (1987) Laymans guide to fatigue. In: Galt JM (Ed.) Wind Energy Conversion 1987, pp. 39–54, Mechanical Engineering Publications Ltd
- Ansell MP** (1995) Fatigue design for timber and wood-based materials, step lecture E22. In: Blass HJ et al. (Eds.) Timber Engineering STEP 2, pp. E22/1–E22/8, Centrum Hout
- Bach L** (1967) Static fatigue of wood under constant strain, Information Report VP-X-24, Canadian Forest Prod. Lab., Vancouver B.C., Canada
- Bach L** (1973) Reiner-Weisenberg's theory applied to time-dependent fracture of wood subjected to various modes of mechanical loading. Wood Sci. 5(3): 161–171
- Bach L** (1975) Frequency-Dependent Fracture in Wood under Pulsating Loading, In FPRS-Annual meeting Proceedings, June 15, 1975, Portland, Oregon, USA
- Bonfield PW** (1991) Fatigue evaluation of wood laminates for the design of wind turbine blades, PhD thesis, University of Bath
- Bonfield PW, Ansell MP** (1991) The fatigue properties of wood in tension, compression and shear. J. Materials Sci. 26: 4765–4773
- Bonfield PW, Ansell MP, Dinwoodie JM** (1994) Fatigue testing of wood, A detailed guide for the development of life prediction formulae from fatigue data. In Proceedings of IUFRO S5.02, International Timber Engineering Conference. pp. 163–174, Sidney, Australia
- Gerhards CC** (1982) Effect of moisture content and temperature on the mechanical properties of wood: an analysis of immediate effects. Wood and Fiber 14(1): 4–36
- Hoffmeyer P** (1990) Failure of wood as influenced by moisture and duration of load, PhD thesis, State University of New York, Syracuse, New York
- Hoffmeyer P** (1993) Non-linear creep caused by slip plane formation. Wood Sci. Technol. 27: 321–335
- Hoffmeyer P, Davidson RW** (1989) Mechano-sorptive creep mechanism of wood in compression and bending. Wood Sci. Technol. 23: 215–227
- Liu JY, Ross RJ** (1995) Energy criterion for fatigue strength of wood structural members. In Proceedings of the 1995 ASME meeting, Mechanics of Cellulosic Materials. Vol. AMD 209/MD 60, pp. 125–133. Los Angeles
- Madsen B** (1992) Structural Behaviour of Timber, 1st edn., Vancouver, Canada: Timber Engineering ltd
- Montgomery DC** (1997) Design and analysis of experiments, 4th edn., New York: John Wiley & Sons
- Philpot TA, Fridley KJ, Rosowsky DV** (1994) Energy-based failure criterion for wood. J. Materials in Civil Engineering, ASCE. 6(4): 578–594
- Reiner M, Weisenberg K** (1939) A thermodynamic theory of the strength of materials. Rheological leaflet 10(12)